

Distributed optical fiber sensing based on frequency-scanned phase-sensitive optical time-domain reflectometry

Présentée le 21 décembre 2020

à la Faculté des sciences et techniques de l'ingénieur
Groupe SCI STI LT
Programme doctoral en photonique

pour l'obtention du grade de Docteur ès Sciences

par

Li ZHANG

Acceptée sur proposition du jury

Prof. C. S. Brès, présidente du jury
Prof. L. Thévenaz, directeur de thèse
Prof. Z. HE, rapporteur
Prof. M. GONZALEZ HERRAEZ, rapporteur
Prof. N. QUACK, rapporteur

In Your light we see light.
— Psalms 36:9

To my late grandparents.

Acknowledgements

First and foremost, special thanks go to my supervisor Prof. Luc Thévenaz, for warmly welcoming me into his laboratory, the guidance throughout my studies, and the efforts he has made to maintain a collaborative and pleasant atmosphere in the lab.

I also would like to thank the jury members: Prof. Miguel González-Herráez, Prof. Zuyuan He, Prof. Camille-Sophie Brés, and Prof. Niels Quack for kindly accepting to review my thesis.

My thesis is built up with many collaborative works, and I would like to acknowledge all the collaborators: the supervisors and colleagues in my exchange studies, Prof. Miguel González Herráez, Prof. Francis Berghmans, Prof. Thomas Geernaert, Prof. Nicholas Walter, Dr. Kenny Hey Tow, Prof. Moshe Tur, Luis Costa, and Sergei Mikhailov, for their the kind hosting and sharing of their expertise; Dr. Maximilian Fisser from Victoria University of Wellington and Łukasz Szostkiewicz from InPhoTech, Poland, for providing the fiber samples.

I am very thankful to the colleagues from Group for Fiber Optics at EPFL. I would like to give my special thanks to the postdocs Dr. Zhisheng Yang and Dr. Fan Yang for the advice and guidance on my study. My thanks also go to the current and previous group members as well as the guest students: Simon Zaslowski, Malak Galal, Dr. Suneetha Sebastian, Tiago Neves, Leonardo Rossi, Prof. Marcelo Soto, Dr. Flavien Gyger, Dr. Desmond Chow, Dr. Zonglei Li, Dr. Sheng Wang, Yun Fu, Prof. Pingyu Zhu. Dr. Can Yao and group administrative assistant Svetlana Machkina. Without their kind support and accompany, my Ph.D. life could be much more difficult and much less fun. My thanks also go to colleagues from PHOSL for kindly sharing the equipment for the experiments.

Besides, I would like to thank my dear flatmates Shuang Liang and Jiangtao Zhou, for being a witness to each other of the suffering and success in the past 4 years. I also appreciate very much the fellowship and spiritual care offered by the members of ECCL and my prayer partner Jing Zhao. My great thanks go to my dear families, partners in crime Ji Hu and Tianyang Song (and many other friends to whom I must apologize for not mentioning) for their unconditional love and support.

Thanks to God, for being my faithful Father, my dearest lover, my closest friend, my refugee and strength in the most difficult time, and the most precious gift in my life. Words can never express my gratitude to you, Jesus Christ, my Lord and my Savior.

Lausanne, 13. Oct. 2020

Li Zhang

Abstract

Unlike traditional sensing schemes which rely on discrete point sensors that perform measurements at predetermined positions, distributed optical fiber sensing is a general technique that enables to continuously gather information (typically temperature and/or strain) along the entire length of an optical fiber. This remarkable feature fulfills today's high demand for multi-points monitoring and detection in complex industrial facilities, e.g. gas/oil delivery systems and civil infrastructures. As one of the most recently investigated distributed optical fiber sensors, frequency-scanned phase-sensitive optical time-domain reflectometry (ϕ -OTDR) can provide quantitative measurements with high sensitivity by frequency shift estimation using the local Rayleigh backscattering spectra, showing the potential of long-distance and high-spatial resolution sensing. In this thesis, particular attention has been paid to this technique to achieve more reliable measurements and explore diverse applications rather than conventional temperature and strain sensing.

After a general introduction on distributed optical fiber sensing, including the main scattering phenomena occurring in optical fibers and the most common interrogation methods, the working principle and numerical model, as well as the phase demodulation schemes of ϕ -OTDR, are reviewed. An emphasis is placed on frequency-scanned ϕ -OTDR, especially in terms of temperature, strain and pressure sensitivity when using standard single mode fibers and some other sensing performance criteria.

A thorough study on the issue of large-errors when using cross correlation for the frequency shift estimation is given analytically and experimentally. The results yielding an explanation to the problem and providing with an estimation of the large error probability. In a disruptive approach, a least mean square algorithm is proposed to reduce these errors, enabling to experimentally demonstrate temperature sensing with long distance and high spatial resolution. Distributed pressure sensing, distributed and dynamic strain sensing, as well as distributed hydrogen sensing, are finally presented and demonstrated using different fibers, based on frequency-scanned ϕ -OTDR with high spatial resolution (5 cm/20 cm). The sensing principles, experimental setups, and results are presented in full detail. The study demonstrates the capability of frequency-scanned ϕ -OTDR for different applications going beyond temperature and static strain sensing, in particular, when combined with fibers based on dedicated designs.

Key words: fiber optics, Rayleigh scattering, distributed optical fiber sensor

Résumé

Contrairement aux systèmes de mesures traditionnels qui reposent sur l'utilisation de capteurs discrets mesurant divers paramètres physiques à des positions bien déterminées, la détection répartie par fibre optique permet de recueillir des informations (généralement liées à la température et/ou la déformation) sur l'intégralité de la fibre. Cette particularité rend les capteurs à fibre optique aptes à répondre à la forte demande actuelle en termes de surveillance et de détection sur de multiples points dans certaines installations industrielles complexes, tels que les systèmes de distribution de gaz/pétrole et les infrastructures de génie civil. Étant l'un des capteurs répartis à fibre optique les plus étudiés actuellement, la réflectométrie optique à balayage de fréquence et à sensibilité de phase dans le domaine temporel est capable de fournir des mesures quantitatives de grande sensibilité par estimation du décalage de fréquence entre les spectres locaux de rétrodiffusion Rayleigh, et démontre ainsi un fort potentiel de mesure à longue distance et à haute résolution spatiale. Dans cette thèse, une attention particulière a été accordée à cette technique, afin de réaliser des mesures plus fiables et d'explorer des applications non conventionnelles, plutôt que de se focaliser sur des mesures plus traditionnelles, telles que la température et la déformation.

Après une introduction générale sur les capteurs répartis à fibre optique, les principaux phénomènes de diffusion observés dans les fibres optiques, les méthodes de mesures les plus communes, leur principe de fonctionnement et le modèle numérique associé sont passés en revue, ainsi que les procédés de démodulation de la phase appliqués à la réflectométrie optique sensible à la phase dans le domaine temporel (ϕ -OTDR). Différents aspects des ϕ -OTDR à balayage de fréquence sont abordés, notamment en termes de sensibilité à la température, à la déformation et à la pression, lors de l'utilisation de fibres unimodales standards, ainsi que de certains critères de performances.

Une étude sur le problème des larges erreurs lors de l'utilisation de la corrélation croisée pour l'estimation du décalage de fréquence est conduite analytiquement et expérimentalement, fournissant une explication au problème des larges erreurs, ainsi qu'une estimation de leur probabilité d'apparition. En rupture avec les approches traditionnelles, un algorithme se reposant sur la méthode des moindres carrés est mis en œuvre, afin de réduire sensiblement la présence de larges erreurs, permettant ainsi une mesure expérimentale de la température à longue distance et à haute résolution spatiale. La détection distribuée de la pression, de la déformation dynamique, ainsi que de l'hydrogène, sont démontrées à l'aide de différent

types de fibre, sur la base d'un système ϕ -OTDR à haute résolution spatiale (5 cm/20 cm). Les principes de détection, les dispositifs et les résultats expérimentaux sont présentés de façon extensive. L'étude illustre les performances du ϕ -OTDR à balayage de fréquence pour différentes applications, allant au-delà des mesures classiques telles que la température et la déformation statique, en particulier lorsque cette technologie est combinée avec des fibres spécifiquement conçues pour ces applications.

Mots clefs : fibre optique, diffusion Rayleigh, détection répartie à fibre optique

Contents

Acknowledgements	i
Abstract (English/Français)	iii
List of figures	xi
List of tables	xv
1 Introduction	1
2 Distributed optical fiber sensing	3
2.1 Scattering mechanisms	4
2.1.1 Spontaneous Raman scattering	4
2.1.2 Spontaneous Brillouin scattering	6
2.1.3 Stimulated Brillouin scattering	8
2.1.4 Rayleigh scattering	10
2.2 Three interrogation schemes on: time, frequency and coherence domains	14
2.2.1 Optical time-domain reflectometry	15
2.2.2 Optical frequency-domain reflectometry	17
2.2.3 Optical coherence-domain reflectometry	19
2.3 Conclusions	20
3 Phase-sensitive optical time domain reflectometry	21
3.1 ϕ -OTDR: an overview	21
3.1.1 ϕ -OTDR with intensity detection	22
3.1.2 1-D model of ϕ -OTDR	22
3.1.3 Experimental setup	25
3.1.4 Statistical properties of ϕ -OTDR traces	26
3.2 ϕ -OTDR with phase demodulation	29
3.2.1 Interferometric phase demodulation	29
3.2.2 Coherent detection	31
3.2.3 Pulse-engineered ϕ -OTDR	32
3.3 Frequency-scanned ϕ -OTDR	33
3.3.1 Working principle	34
3.3.2 Experimental setup	35

3.3.3	Temperature, strain and pressure sensitivities	36
3.3.4	Key criteria of the interrogator	42
3.3.5	Two main sources of noise	45
3.4	Conclusions	47
4	Large errors on frequency estimation	49
4.1	Frequency shift estimation using cross correlation	49
4.2	Large errors analysis	51
4.2.1	An example of large errors	52
4.2.2	Analytical model for Large errors analysis	53
4.2.3	Comparison of the theoretical and experimental <i>PLE</i>	55
4.3	Least mean square for reducing the large errors	59
4.3.1	<i>PLE</i> of least mean square algorithm	59
4.3.2	Temperature sensing with high spatial resolution	61
4.4	Conclusions	63
5	Distributed pressure sensing	65
5.1	Principle	66
5.2	Experimental setup	67
5.3	Distributed pressure sensing using "butterfly" PCFs	68
5.3.1	"Butterfly" photonic crystal fibers	69
5.3.2	Experimental results	70
5.4	Distributed pressure sensing using side air-hole fiber	71
5.4.1	Side air-hole fiber	71
5.4.2	Experimental results	72
5.4.3	Discussions	75
5.5	Conclusions	78
6	Dynamic strain sensing	79
6.1	Experimental setup	80
6.1.1	Setup	80
6.1.2	RF pulsing scheme	81
6.1.3	Backscattering-enhanced fiber	82
6.2	Experimental results	84
6.2.1	Frequency shift estimation using cross correlation	84
6.2.2	Using least mean square	85
6.3	Conclusions	86
7	Distributed hydrogen sensing	89
7.1	Sensing fiber design	90
7.2	Experimental setup	90
7.3	Experimental results	91
7.4	Conclusions	94

8 Conclusions and Perspectives	95
8.1 Main contributions	95
8.2 Future work	98
Bibliography	101
List of acronyms	113
List of symbols	115
List of publications	117
Curriculum Vitae	119

List of Figures

2.1	Principle of distributed fiber sensing	3
2.2	Three types of scattering mechanisms in the fiber [4]	4
2.3	Energy diagram of Raman scattering	5
2.4	Momentum conservation of spontaneous Brillouin scattering in Stokes case	6
2.5	Stimulated Brillouin scattering: the pump wave (incident light) interferes with the signal wave (scattering wave)	9
2.6	Coordinate system for calculation of the Rayleigh scattered light field	11
2.7	Schematic diagram of OTDR (FUT; fiber under test)	15
2.8	Typical trace of OTDR (FUT: fiber under test)	16
2.9	Schematic diagram of OFDR (FUT: fiber under test, FRM: Faraday rotator mirror)	17
2.10	Schematic diagram of OCDR (DUE: device under evaluation)	19
3.1	Intrusion sensing based on ϕ -OTDR (traces at t_1 and t_2 are the intensity traces of Rayleigh scattered light obtained before and after the intrusion, respectively)	22
3.2	1 D model of Rayleigh scattering in in the fiber	23
3.3	Diagram of a typical ϕ -OTDR setup. (EOM: electro-optic modulator, Cir.: circulator, TF: tunable filter, PD: photodetector, OSC: oscilloscope, PC: personal computer)	25
3.4	Optical intensity of Rayleigh backscattering light along the fiber distance	25
3.5	Random walk process of the phase of the Rayleigh scattered light from different scatters: (a) constructive summation; (b) destructive summation	26
3.6	Probability of density function of ϕ -OTDR trace	28
3.7	Schematic diagrams of phase demodulation using interferometric receiving schemes: (a) Mach-Zehnder interferometer; (b) Michelson interferometer with phase-generated carrier (PGC). FRM: Faraday rotator mirror; PZT: piezoelectric transducer.	30
3.8	Schematic diagrams of phase demodulation with coherent detection: (a) heterodyne detection; (b) homodyne detection.	31
3.9	Principle of frequency-scanned ϕ -OTDR: (a) conceptual view of interrogation in frequency-scanned ϕ -OTDR; (b) Intensity of Rayleigh backscattered traces for the different scanning optical frequencies; (c) Rayleigh spectra of reference and measurement showing the strain/temperature-induced frequency shift at position L_0	34

3.10	Diagram of a typical ϕ -OTDR setup. (EOM: electro-optic modulator, Cir.: circulator, TF: tunable filter, PD: photodetector, OSC: oscilloscope, PC: personal computer, FBG: fiber Bragg grating)	35
3.11	Experimental traces of frequency-scanned ϕ -OTDR: (a) time-domain trace (distribution along distance); (b) frequency-domain trace. The data are obtained with a 10 ns pulse width, which corresponds to a spatial resolution of 1 m.	36
3.12	Probability of density function of an spectra obtained from the frequency-scanned ϕ -OTDR at a certain position	36
3.13	Thermal expansion coefficient of fused silica SRM 739	37
3.14	Thermo-optic coefficient at wavelength 1550 nm	39
3.15	Illustration of the spatial resolution of OTDRs	43
3.16	Effect of the extinction ratio on the pulse modulation	45
4.1	Frequency estimation using cross correlation for frequency-scanned ϕ -OTDR: (a) 2-D intensity map of the reference and (b) spectrum at the i_{th} position point in the reference measurement; (c) 2-D intensity map of the j_{th} measurement; (d) spectrum at the i_{th} position point of the j_{th} measurement; (e) local correlation spectrum at the i_{th} position point; (f) close-up view of the correlation peak.	50
4.2	An example of the occurrence of large errors: (a) the reference spectrum and (b) the measurement spectra at the position of the 2047 _{th} sampling point (c) correlation spectra at the 2047 _{th} sampling point (with error) and the 2000 _{th} sampling point (without large error). (d) Estimated FS profile obtained by cross correlation showing the occurrence of a large error.	53
4.3	Experimental setup of frequency-scanned ϕ -OTDR (EOM: electro-optical modulator, EDFA: erbium-doped fiber amplifier, Cir: circulator, FUT: fiber under test, TF: tunable filter, PD: photodetector, OSC: oscilloscope, PC: personal computer, PG: pulse generator, Sync, synchronization).	55
4.4	Comparisons between experimental and theoretical results. The probability of large error v.s. scan range F_t with a pulse width of (a) 1 ns and (b) 500 ps, F_0 is the frequency offset between measurement and reference spectra; (c) comparative <i>PLE</i> using different pulse widths ($F_0=3$ GHz) (d) <i>PLE</i> dependence on FS ($F_t=30$ GHz) (PW: pulse width)	57
4.5	Diagram to show the different scan ranges of reference and measurement.	58
4.6	<i>PLE</i> vs. spectral scanning range of measurement F_s with a pulse width of (a) 1 ns and (b) 500 ps when the scanning ranges of the reference and measurement are different. F_0 is the frequency range difference between the measurement and reference spectra i.e. $F_0 = 2F_d$	59

4.7	Principle of the frequency shift estimation using the proposed least mean squares (LMS) method. (a) The measurement spectrum at a given point (orange) is swept over the broad reference spectrum (blue) and LMS are calculated for each relative spectral position δf . (b) Mean square errors as a function of the frequency shift δf showing a clear minimum value which is the estimation of the best similarity.	59
4.8	Comparison of <i>PLE</i> between LMS and correlation with increasing scan range of measurement F_s (PW=1 ns), (a) with noise; (b) without noise.	60
4.9	Experimental results of temperature sensing using the proposed LMS-based ϕ -OTDR: (a) Spectra of the reference (blue line, obtained by tuning the temperature of the laser) and 6 measurements at different temperatures (at a fiber position of ~852 m, obtained by tuning the current of the laser); (b) Retrieved frequency shift profiles.	61
4.10	frequency shift distributions around the edge of the hotspot which confirms a spatial resolution of less than 5 cm.	62
5.1	Scanning procedure of the interrogating pulses for the reference and measurement.	66
5.2	Pressure sensing principle: (a) obtained Rayleigh scattering (RS) spectra; (b) correlation spectra between Y references and measurements on each polarization axis, respectively.	67
5.3	Experimental setup. OS: optical source, PSw: polarization Switch, PolC: polarization controller, FUT: fiber under test, OR: optical receiver, OSC: oscilloscope.	68
5.4	Scanning electron microscope (SEM) images of the cross sections of the two PCFs under test: (a) fiber A; (b) fiber B	69
5.5	Differential frequency shift distributions along (a) fiber A and (b) fiber B under various applied pressures, respectively	70
5.6	Mean frequency shift in (a) fiber A and (b) fiber B as a function of pressure change	71
5.7	SEM image of the cross section of side-hole fiber	71
5.8	(a) pressure and (b) temperature response along the two polarization axes of the fiber, respectively.	72
5.9	Correlations of RS spectra when 12 bar pressure is applied. (a) slow axis; (b) fast axis. (5 cm spatial resolution)	73
5.10	(a) Pressure change distribution along the fiber; (b) Zoom-in at the pressure transition	74
5.11	Responses of (a) fast and (b) slow axis when 3 bar,6 bar and 9 bar pressure changes are applied to the fiber; (c) pressure distributions and (d) temperature/strain distributions demodulated from the discrimination algorithm	75
5.12	The pressure sensitivity depends quadratically on the angle γ [138]	76

5.13 (a) Temperature and (b) pressure sensitivities with different core diameters. Parameters used for simulation: 72 GPa, 0.17, 1.14×10^{-6} [1/K], and 5.5×10^{-7} [1/K] for Young's modulus, Poisson's ratio and thermal expansion coefficient for core and cladding, respectively	76
6.1 Schematic of the experimental setup. AWG: arbitrary waveform generator; EOM: electro-optic modulator; FUT: fiber under test; PD: photodetector. The AWG helps the generation of short, high extinction ratio pulses, over a precise wide frequency range with close to zero switching latency	81
6.2 Schematic diagrams of (a) the RF signal applied to the EOM and (b) the envelope of the generated pulse train after Filter 1.	82
6.3 Measured spectra of light before and after Filter 1 ($T=0.6 \mu\text{s}$ and $\tau=2 \text{ ns}$).	82
6.4 The enhanced backscattering from the special fiber [104] used in the experiment. The two fibers were illuminated with the ASE from an EDFA and measured with an optical spectrum analyzer using a circulator. The reflectivity here is defined as the reflected spectrum normalized by the input spectrum.	83
6.5 Strain distribution along the fiber: (a) Time domain; (b) Frequency domain based on FFT of a 20 ms long acquisition.	84
6.6 Demodulated strain inside and outside of the vibrating fiber segment: (a) Time domain; (b) Power spectral density.	84
6.7 Instantaneous strain distribution around the vibrating fiber segment, demonstrating the actual 20 cm spatial resolution.	85
6.8 Demodulated strain for a triangular driving voltage inside and outside of the vibrating segment: (a) Time domain; (b) Power spectral density.	86
7.1 SEM image of the cross-sectional view of the sensor. To increase the visibility of the adhesive, the SEM potting epoxy was filled with silica nanoparticles.	90
7.2 Experimental setup for distributed hydrogen sensing	91
7.3 Frequency shift responses of the sensing fiber every 5 minutes in half an hour: after exposing the sensor to the gas with hydrogen concentrations of (a) 0.3% and (b) 0.6%, respectively	92
7.4 Frequency shift responses of the 4 sensing segments over 6 hours. The hydrogen concentration-changing events are indicated in the time chart.	93
7.5 Frequency shift response when the hydrogen concentration changes from (a) 0% to 0.3%; (b) 0.3% to 0.38%	93



List of Tables

3.1	Parameters in the Sellmeier model for Corning 7980 fused silica[96]	38
8.1	Summary of demonstrated sensing performance	97

1 Introduction

Fiber-optic communication, as the hardware basis for the Internet technology, lays the foundations for the information age and has sharpened the modern life style significantly. As one of the key inventions in fiber-optic communication, optical fibers demonstrate extremely low transmission loss (0.2 dB/km) and other important advantages such as low cost, light weight, immunity to electromagnetic interference among others. The main stream of research and application on optical fiber is based on its role as *transmission* medium in optical communication; however, it also serves as information writing and reading medium such as imaging tools, medium for lasers, sensors and so forth.

Apart from fiber-optic communication, distributed optical fiber sensor (DOFS), in which the optical fiber plays a role of both transmission and sensing medium, is another great example of taking the best advantages of the exceptionally low loss and also the other intrinsic advantages of the optical fiber as mentioned above. It is a technique which cost-effectively provides information from thousands of or even millions of locations with just one interrogator and a single fiber, instead of a complex sensor array deployed. Today's high demand of multi-points monitoring for long distance in harsh environment is being fulfilled by DOFS in many domain such as structural health monitoring (long bridges, electrical cables, oil and gas pipelines, etc), security surveillance, and other energy industry [1, 2, 3].

The working principle of DOFS is based on a scattering process of light in the fiber: Rayleigh scattering, Brillouin scattering and Raman scattering; and there are three main interrogation schemes to spatially resolve the information which is carried by the scattered light: in time domain, frequency domain and correlation domain. As one of the most promising DOFS techniques based on Rayleigh scattering, phase-sensitive optical time-domain reflectometry (ϕ -OTDR) is drawing increasing attentions both in academic research and industrial application areas, owing to its ultra high sensitivity and potential for long-distance sensing.

In this dissertation, we are focusing on the study and development of distributed optical fiber sensing based on ϕ -OTDR. To demodulate the phase change of the fiber, the frequency of the interrogating light is scanned and the frequency shift of the Rayleigh backscattered

spectra is linearly proportional to the amplitude of the environmental perturbations. The measurement errors are investigated theoretically and experimentally. A great effort has been made to demonstrate distributed pressure sensing using the frequency-scanned ϕ -OTDR and the potential of sensing other measurands has been explored.

The thesis is structured as following:

In Chapter 2, it gives a general review of distributed optical fiber sensor (DOFS) based on different scattering mechanisms and interrogation schemes.

Chapter 3 addresses the fundamentals of a particular DOFS system: ϕ -OTDR, including the numerical description of Rayleigh scattering in the fiber, and the working principle of intensity of intensity-based ϕ -OTDR. It also reviews the phase demodulation schemes of ϕ -OTDR and an alternative method to retrieve the phase information of the Rayleigh scattering by scanning the frequency of the interrogating light. The phase sensitivities on temperature, strain and pressure of fiber are discussed, as well as some key measurement parameters of frequency-scanned ϕ -OTDR, such as the sensing distance, the spatial resolution, the dynamic range and response time. In addition, two different sources of noise in the system are specifically addressed.

Chapter 4 explores the measurement large errors on the frequency shift estimation of frequency-scanned ϕ -OTDR. It has been found that the large error results from the limited spectral span and the errors exist even with infinite high signal-to-noise ratio. The problem is studied analytically and experimentally. Solution based on least mean square algorithm is proposed to reduce the large errors and demonstrated for temperature sensing.

Thanks to the ultra-high sensitivity of ϕ -OTDR and the proper designs of the fiber, frequency-scanned ϕ -OTDR have the potential to sensing different quantities with high spatial resolution distributedly and even dynamically. In Chapter 5-7, three experimental demonstrations on exploring the capability to sensing different physical quantities with different designs of optical fiber are presented, based on frequency-scanned ϕ -OTDR. Chapter 5 focuses on distributed pressure sensing, using two different types of fiber: photonic crystal fibers (PCFs) and air side hole fiber. In chapter 6 and chapter 7, distributed hydrogen sensing and distributed dynamic strain sensing are presented, separately, as examples to explore the capability of the system for different applications.

The final chapter summarizes the main results of this thesis and a few perspectives on frequency-scanned ϕ -OTDR are proposed.

2 Distributed optical fiber sensing

The principle of distributed optical fiber sensing (DOFS) is schematically shown in Fig. 2.1. Intensity and/or frequency modulated light is sent into the fiber as an optical probe that picks up vibrations or temperature changes along its way through different scattering mechanisms. The information is carried on by the scattered light up to detection, where it is then processed to be spatially resolved. In this chapter, the main scattering mechanisms used in DOFS as well as the most common interrogating schemes are introduced briefly.

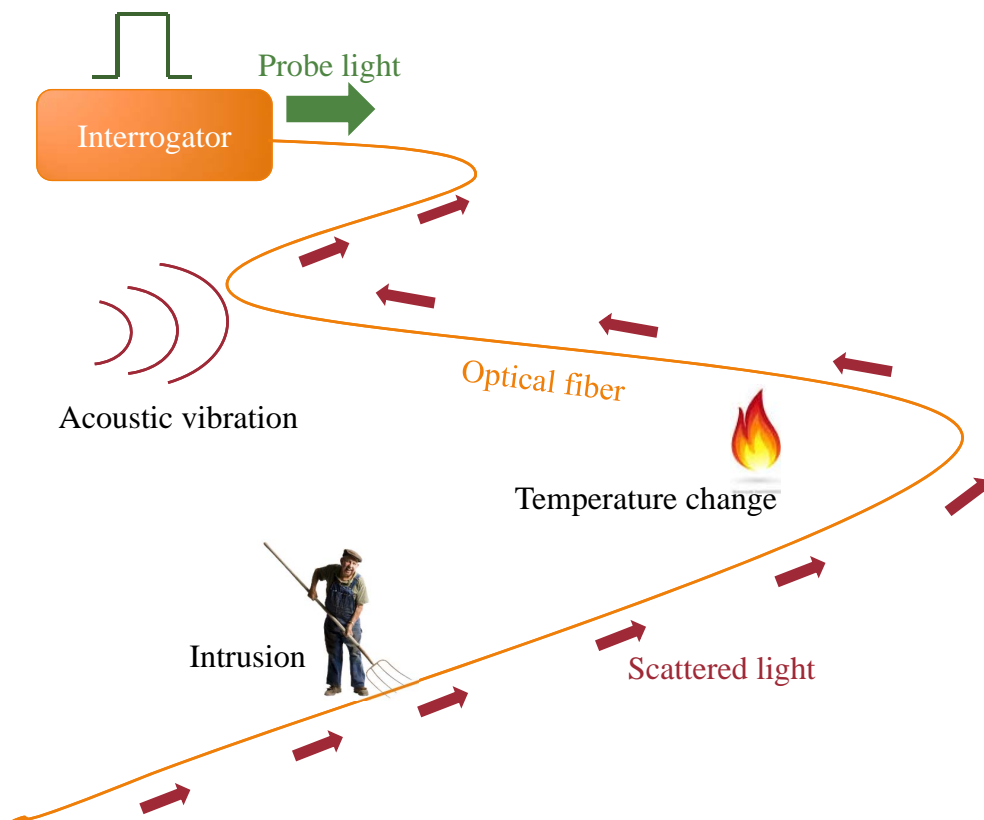


Figure 2.1 – Principle of distributed fiber sensing

2.1 Scattering mechanisms

Scattering phenomena result from light-matter interactions: when an optical wave propagates in a given medium, it interacts with its constituents at a molecular level and a part of the incident light is deflected. Since these physical processes depend on the mechanical and optical properties of the medium, distributed optical fiber sensors (DOFS) rely on the different scattering processes occurring in an optical fiber to remotely access local environmental changes, typically temperature and/or strain. The great majority of existing DOFS are based on three scattering mechanisms: Rayleigh scattering, Brillouin scattering and Raman scattering, whose spectra are shown in Fig. 2.2.

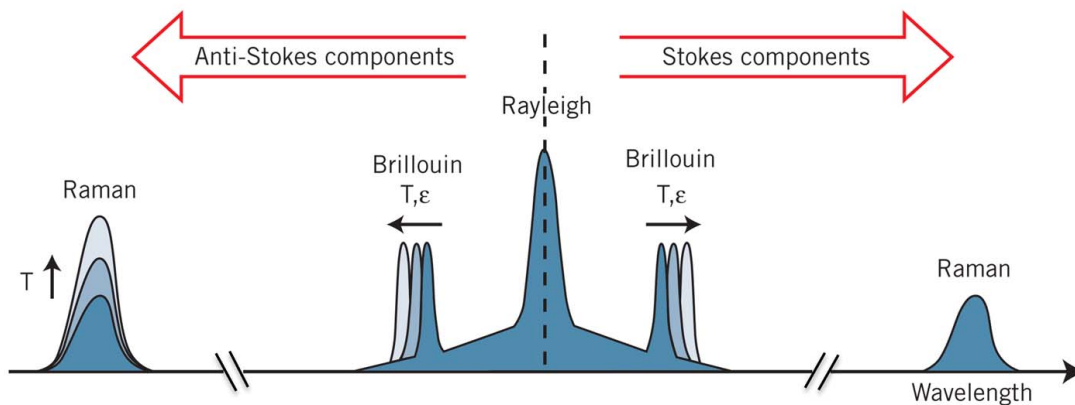


Figure 2.2 – Three types of scattering mechanisms in the fiber [4]

In this section, four scattering processes^I are introduced briefly; they are spontaneous Raman scattering, spontaneous Brillouin scattering, stimulated Brillouin scattering and Rayleigh scattering^{II}. As of now, these four scattering mechanisms make up the core of the technique for distributed optical fiber sensing.

2.1.1 Spontaneous Raman scattering

Raman scattering was firstly observed by C.V. Raman in 1928 [5]. When light shines on a material, spontaneous Raman scattering (SpRS) transfers a small fraction (typically $1/10^{-6}$) of the incident power to another optical field, i.e. the scattered light spectrum contains new frequencies, different from those of the excitation source. As is shown in Fig. 2.2, the new components that are shifted to higher wavelength are called Stokes components, while those that are shifted to lower wavelength are called anti-Stokes components^{III}.

SpRS is a the light-matter interaction involving vibrational (or rotational) transitions at a

^IAll three phenomena can be categorized in two regimes: spontaneous and stimulated, which are linear and nonlinear processes, respectively. Stimulated Raman scattering and Stimulated Rayleigh scattering are not discussed here since there are very few DOFS based on those two scattering mechanisms.

^{II}The so called Rayleigh scattering often refers to the spontaneous elastic regime.

^{III}The same naming rule also applies to Brillouin scattering as shown in Fig. 2.2

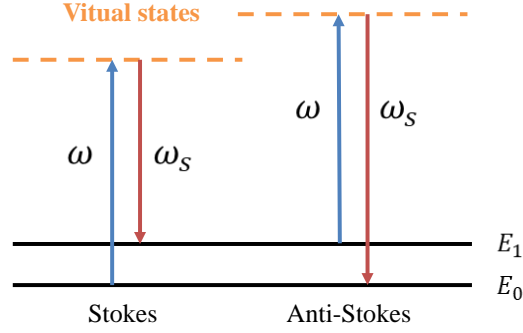


Figure 2.3 – Energy diagram of Raman scattering

molecular level. It can be explained schematically from the energy diagram shown in Fig. 2.3: An incident photon excites a molecule from ground state E_0 to a higher state E_1 through a virtual state, generating a photon with reduced energy (Stokes process); As for the anti-Stokes case, a molecule at an energy level E_1 absorbs an incident photon through a virtual state and decays to its ground state; at the same time, a photon with higher energy is emitted. Assume that the frequency of the incident photon is ω , and the frequency of the scattered photon is $\omega \pm \Omega_A$, where Ω_A is related to the angular frequency of the thermal vibration of the molecule. The quantity $\nu_R = \Omega_A/2\pi$ describes the Raman frequency shift experienced by the scattered light.

The strength of the anti-Stokes scattering is determined by the average number of thermally activated phonons N_{ave} in the material, since a phonon and an incident photon are annihilated to create a new photon during the process. However, the scattering strength for the Stokes process is proportional to $N_{ave} + 1$, given that the incident photon is annihilated to generate a new phonon and photon pair. The average number of thermally activated phonons in a material is governed by the Bose-Einstein distribution [6]:

$$N_{ave} = \frac{1}{\exp\left(\frac{h\nu_R}{k_B T}\right) - 1} \quad (2.1)$$

where k_B and T are the Boltzmann constant and the absolute temperature in Kelvin, respectively. For instance, at ambient temperature ($T=293$ K), the typical Raman frequency shift is ~ 13.2 THz in fused silica [7], the thermally activated phonons N_{ave} is therefore ~ 0.13 , which is much smaller than 1. As a consequence, the strength of the Stokes process is much less sensitive to temperature since $N_{ave} + 1 \approx 1$, and the ratio between the strength of the anti-Stokes and Stokes process is :

$$S_R = \frac{N_{ave}}{N_{ave} + 1} = \exp\left(-\frac{h\nu_R}{k_B T}\right). \quad (2.2)$$

By measuring the power of the scattered anti-Stokes and Stokes light, we can retrieve

the temperature information, which is the main working principle of Raman distributed temperature sensors (DTS).

DTS was first investigated in 1985 [8] and has been commercialized for distributed temperature sensing in various areas, such as oil well, and pipelines. [9, 10]. One of the most remarkable advantages of Raman-based temperature sensing compared with DOFS systems based on Brillouin and Rayleigh scattering, is that it is insensitive to strain, [11]. As mentioned before, the Raman frequency shift is $\nu_R \approx 13.2$ THz in fused silica. For an incident light working at a wavelength of 1310 nm, the spectral separation between the Stokes and anti-Stokes is 120 nm. In this case, the different attenuation experienced by the Stokes and the anti-Stokes components due to their spectral separation can introduce errors into the temperature measurements. To compensate this attenuation difference, double ends configuration [12] and double light sources methods [13] were introduced to increase the sensing accuracy. Due to the low efficiency of SpRS, multimode fibers were utilized in early works to obtain higher scattered power since the multi modes fibers have larger backscattering capture factor [8, 14]. However, inter-modal dispersion has limited the sensing range as well as the spatial resolution. Today's commercially available Raman-based DTS can typically measure up to 14 km of fiber with a spatial resolution of 1 m [15, 16].

2.1.2 Spontaneous Brillouin scattering

Unlike Raman scattering, where the light interacts with the vibration of individual molecules (optical phonons: high energy and low momentum), Brillouin scattering is the phenomenon in which energy couples between optical modes and vibrational modes of the entire molecular chain (acoustic phonons: low energy and high momentum) [6].

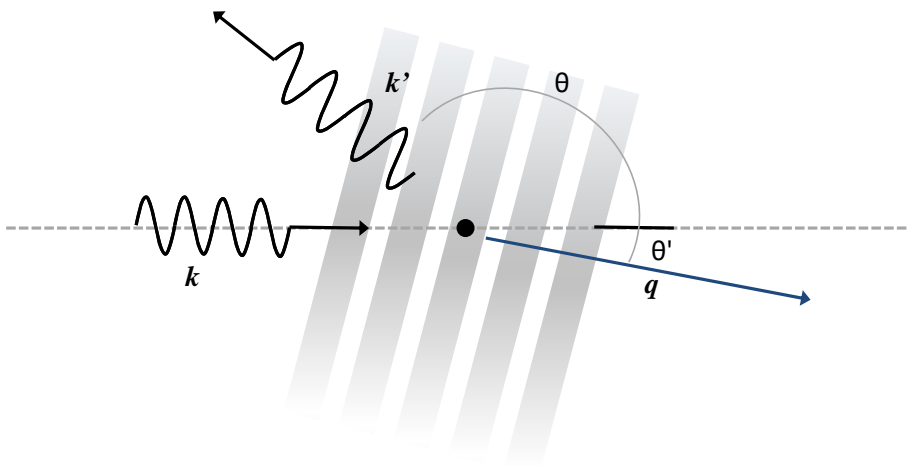


Figure 2.4 – Momentum conservation of spontaneous Brillouin scattering in Stokes case

Fig. 2.4 depicts the wavevector diagram of spontaneous Brillouin scattering (SpBS): the incident optical wave, with frequency ν and wavevector \mathbf{k} , is partially diffracted when interacting with the thermally activated acoustic wave (bulk acoustic wave, gray shape in Fig. 2.4), which frequency and wavevector are ν_a and \mathbf{q} , respectively. The acoustic wave induce refractive index variation via photo-elasticity thus diffracting the incident light. Assuming for the frequency and wavevector of the scattered light to be ν' and \mathbf{k}' , respectively, and applying energy and momentum conservation to the three waves:

$$\nu' = \nu - \nu_a \quad (2.3a)$$

$$\mathbf{k}' = \mathbf{k} - \mathbf{q} \quad (2.3b)$$

By projecting the wavevectors shown in Fig. 2.4 along the orthogonal axes, we have:

$$\begin{cases} k' \sin\theta = q \sin\theta' \\ k = k' \cos\theta + q \cos\theta' \end{cases} \quad (2.4)$$

θ is the angle between \mathbf{k} and \mathbf{k}' , and θ' is the angle between \mathbf{q} and \mathbf{k} . Considering Eq. 2.3, Eq. 2.4 and the relationship between wavenumbers and frequencies $\nu = kc/2\pi$, $\nu' = k'c/2\pi$, $\nu_a = qV_a/2\pi$, where c and V_a represent the light and acoustic velocities in the medium, respectively, the general relation linking the frequencies and velocities of the incident light wave and the acoustic wave is obtained as follows:

$$4V_a^2 \nu(\nu - \nu_a) \sin^2\left(\frac{\theta}{2}\right) = (c^2 - V_a^2) \nu_a. \quad (2.5)$$

Thus the frequency of the acoustic wave ν_a can be derived as:

$$\begin{aligned} \nu_a &= 2 \frac{V_a}{c} \nu \sin\left(\frac{\theta}{2}\right) \sqrt{1 - \left(\frac{V_a}{c}\right)^2 \cos^2\left(\frac{\theta}{2}\right)} - 2 \left(\frac{V_a}{c}\right)^2 \nu \\ &\approx 2 \frac{V_a}{c} \nu \sin\left(\frac{\theta}{2}\right) = 2n \frac{V_a}{\lambda_o} \sin\left(\frac{\theta}{2}\right) \end{aligned} \quad (2.6)$$

where λ_o is the wavelength of the incident light in vacuum. The approximation in Eq. 2.6 comes from the fact that the velocity of light is much larger than that of the acoustic wave in the medium (e.g. in silica, the velocities of light and acoustic waves are $\sim 2 \times 10^8$ m/s and $\sim 6 \times 10^3$ m/s, respectively).

From Eq. 2.6 we can see that the frequency shift of the scattered light with respect to the incident light ν_a is highly dependent on the scattering angle θ . The shift is maximized when $\theta=180^\circ$ (in the backward direction) and it is zero when $\theta=0^\circ$ so the scattered light can not be distinguished from the incident light in the forward direction. The backward frequency shift of the scattered light in the counter-propagating direction is called the Brillouin shift:

$$\nu_B \equiv \nu_a(\theta = \pi) = 2n \frac{V_a}{\lambda_o} \quad (2.7)$$

From Eq. 2.7 we can see that v_B is related with the acoustic velocity and optical refractive index of the material. In single standard single mode fiber (SMF) at 1550 nm, v_B is normally about 11 GHz.

In solid materials, the acoustic velocity is given by:

$$V_a = \sqrt{\frac{B}{\rho}} \quad (2.8)$$

where B is the bulk modulus and ρ is the material density. Both ρ in Eq. 2.8 and n in Eq. 2.7 are temperature-dependent. Besides, mechanical deformations such as strain will also change the material density as well as the refractive index through photoelasticity [17]. Consequently, SpBS can be used for temperature and strain sensing by measuring v_B . In silica fibers, the temperature and strain sensitivities are approximately:

$$\frac{\Delta v_B}{\Delta T} \approx 1.26 \text{ MHz/K} \quad (2.9a)$$

$$\frac{\Delta v_B}{\Delta \varepsilon \times 10^{-6}} \approx 0.056 \text{ MHz}/\mu\varepsilon \quad (2.9b)$$

where T and ε are the temperature and strain applied to the fiber. Typical SpBS-based DFS systems include Brillouin optical time-domain reflectometry (BOTDR) [18] and Brillouin optical frequency-domain reflectometry (BOFDR) [19, 20]. They are often implemented for distributed strain sensing in structural health monitoring [21]. As frequency-based techniques, the advantage of Brillouin-based DOFSs is that they are less sensitive to the fiber loss, compared with the intensity-based sensors such as Raman-based DTSs.

2.1.3 Stimulated Brillouin scattering

When the incident light is strong enough, the optical properties will be changed by the incident light and the scattering strength is no longer dependent on thermally-activated phonons. In this case, the scattering process is much more efficient than the spontaneous processes and it is called *stimulated* [17].

Stimulated Brillouin scattering (SBS) is one of the most often used stimulated processes in DOFS. In SBS, an optical pump wave (with frequency ν_p) interferes with a counter-propagating optical signal wave (with frequency ν_s). The resulting beat wave (with frequency $\nu_p - \nu_s$) produces, through electrostriction (or radiation pressure), an acoustic wave (with frequency $\nu_p - \nu_s$) traveling at the acoustic velocity. As the acoustic wave propagates along the fiber, a moving grating is created through photoelasticity, that scatters back the pump. When the frequency difference between pump and signal matches the Brillouin shift, i.e. $\nu_p - \nu_s = \nu_B$, the energy is transferred from pump to signal with the maximum efficiency. The increased signal will in turn enhance the intensity of the beat wave, and consequently the amplitude of the acoustic wave. Overall, both the scattered light as well as the moving grating strength are

enhanced through this positive feedback as illustrated in Fig 2.5 [6]. The same mechanism takes place when only the pump wave is initially present: when the intensity of the pump is high enough, i.e. past the so-called *critical point*, the incident light scattered through SpBS is powerful enough to play the role of the signal wave described here above. In this case, the whole process builds up from thermally activated acoustic waves.

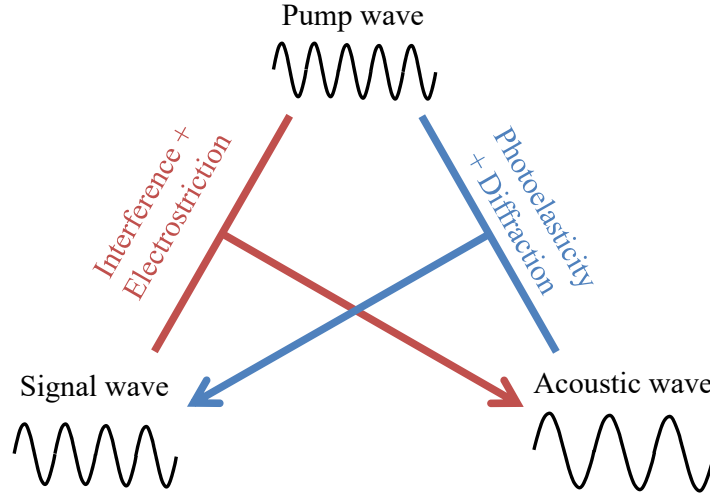


Figure 2.5 – Stimulated Brillouin scattering: the pump wave (incident light) interferes with the signal wave (scattering wave)

The amplitude of the three waves in an optical fiber can be described by [22]:

$$\left\{ \begin{array}{l} \frac{\partial E_P}{\partial z} - \frac{n_1}{c} \frac{\partial E_P}{\partial t} = E_A E_S \\ \frac{\partial E_S}{\partial z} + \frac{n_1}{c} \frac{\partial E_S}{\partial t} = E_A^* E_P \\ \frac{\partial E_A}{\partial z} + \Gamma_d E_A = \frac{1}{2} g_B E_P E_A^* \end{array} \right. \quad (2.10)$$

where E_P , E_S and E_A are the amplitude of the pump wave, signal wave and the acoustic wave, respectively. $\Gamma_d = \Gamma_B + i2\pi\delta\nu_B$ is the damping factor, which is related to the phonon life time $1/\Gamma_B$ and the detuning factor $\delta\nu_B$. The gain factor is given by [23]:

$$g_B = \frac{2\pi n^7 p_{12}^2 K_P}{c\lambda^2 \rho V_A \nu_B} \frac{P_P}{A_{\text{eff}}}, \quad (2.11)$$

where P_P is the pump power, λ is the pump wavelength, A_{eff} is the effective core area, p_{12} is one element in the strain-optical tensor of the material (longitudinal elasto-optic coefficient) and K_P varied from 0 to 1, which is a factor which describes the alignment between the polarization states of pump and signal. On average K_P equals 0.5.

SBS has the highest efficiency among the nonlinear optics effects taking place in an optical fiber and has been widely used in DOFS such as Brillouin optical time-domain analyzer (BOTDA), Brillouin optical frequency-domain analyzer (BOFDA) and so on. Since the probe power can be much stronger than the spontaneous scattered light, the SBS based DOFS systems are suitable for long distance sensing [24]. However, the pump and probe need to be launched into the sensing fiber from opposite ends, since the scattering coefficient is zero when the probe and pump light are co-propagating. The equivalent one-end sensing range has to be shortened to half of the total fiber loop. With specially-designed erbium doped fiber amplifier (EDFA) repeaters, the sensing distance of BOTDA was extended to 325 km in 2014, corresponding to a 650 km fiber loop [25]. Assisted with coding and Raman amplification, a repeaterless BOTDA with record long distance of 175 km has been achieved [26]. Normally, the phonon acoustic lifetime (in the order of 10 ns) limits the spatial resolution to 1 meter, unless sophisticated coding schemes are utilized [27, 28]. Very recently, through signal processing, the submeter spatial resolution has also been demonstrated [29].

2.1.4 Rayleigh scattering

Rayleigh scattering originates from non-propagating density fluctuations in the medium [17]. This scattering process takes place when the scale of the fluctuations (the size of the scatterer) is much smaller than the wavelength of the incident light. In a dense medium (e.g. silica), this process can be described using a microscopic approach.

The local perturbations of the medium lead to variations of the material optical properties, thus the process can be described by the dielectric tensor ϵ :

$$\mathbf{D} = \epsilon \mathbf{E} = \epsilon_0 \mathbf{E} + \mathbf{P} \quad (2.12)$$

Here \mathbf{D} , \mathbf{E} and \mathbf{P} are the electric displacement vector, electric field and polarization vector, respectively while ϵ_0 is the permittivity in vacuum. The response of the medium can be described by the polarization vector as:

$$\mathbf{P} = \epsilon_0 \chi \mathbf{E} \quad (2.13)$$

where χ is the susceptibility tensor. The tensor χ is a fundamental parameter to describe how the medium responds to an incident electromagnetic field and $\epsilon = \epsilon_0 (\mathbf{I} + \chi)$ where \mathbf{I} is the identity matrix. We can rewrite the dielectric tensor to address the perturbations by an averaged value (scalar term) plus small perturbations (tensor):

$$\epsilon = \bar{\epsilon} \mathbf{I} + \Delta \epsilon \quad (2.14)$$

where $\bar{\epsilon}$ is the average dielectric constant of the medium, which we assume as isotropic. The first term represents the homogeneous contribution to the dielectric tensor whereas the second term $\Delta \epsilon$ is the temporally and/or spatially varying fluctuations in the dielectric tensor,

leading to light scattering. We can further decompose the fluctuation term into a scalar and a tensor contribution:

$$\Delta\epsilon = \Delta\epsilon I + \Delta\epsilon^t \quad (2.15)$$

The first term comes from fluctuations in thermodynamic quantities, e.g. the pressure, density, temperature and entropy. Scattering due to $\Delta\epsilon$ is categorized as scalar light scattering, including Brillouin scattering and Rayleigh scattering. Scattering arising from the second term in Eq. 2.15 is called tensor light scattering, including Raman scattering and Rayleigh-wing scattering.

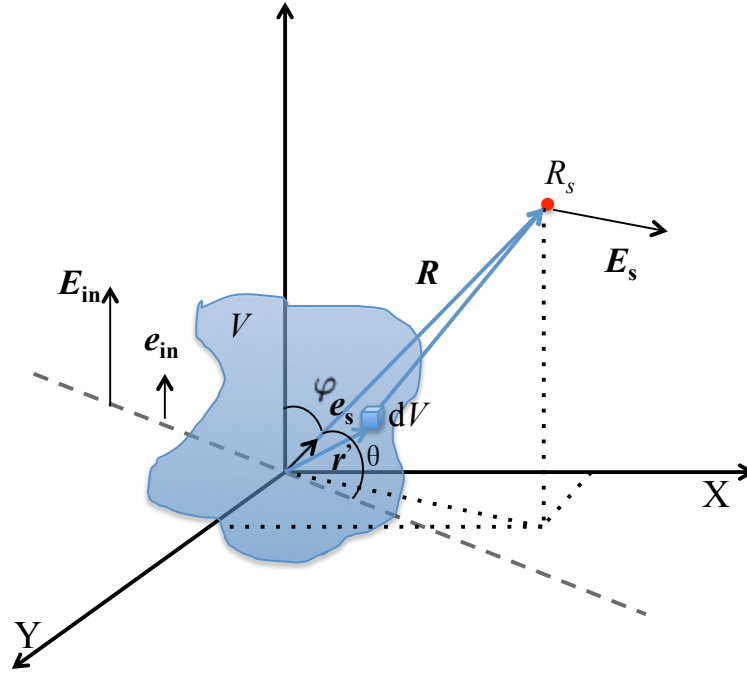


Figure 2.6 – Coordinate system for calculation of the Rayleigh scattered light field

To calculate the intensity of the Rayleigh scattered light, we consider a plane optical wave as the incident wave:

$$\mathbf{E}(\mathbf{R}, t) = E_{\text{in}} \mathbf{e}_{\text{in}} e^{j(\boldsymbol{\beta}_{\text{in}} \mathbf{R} - \omega t)} \quad (2.16)$$

E_{in} is the amplitude of the incident field, \mathbf{e}_{in} is the unit vector aligned with the light polarization state (a linear polarization of the incident light is assumed here), $\boldsymbol{\beta}_{\text{in}}$ is the propagation wave vector, \mathbf{R} is the position of interest in the xyz coordinated system, and ω is the optical frequency. The scattered field generated by a volume V of the medium at a position R_s far from the scattering volume (illustrated in Fig. 2.6) is given by [6]:

$$\mathbf{E}_s(\mathbf{R}, t) = E_{\text{in}} \frac{\omega^2}{c^2} [\mathbf{e}_s \times (\mathbf{e}_s \times \mathbf{e}_{\text{in}})] \frac{e^{j(\beta_s R - \omega t)}}{4\pi R} \frac{1}{\epsilon_0} \int_V \Delta\epsilon(\mathbf{r}', t) e^{j(\boldsymbol{\beta}_{\text{in}} - \boldsymbol{\beta}_s) \mathbf{r}'} d\mathbf{r}' \quad (2.17)$$

Here $R = |\mathbf{R}|$ and $\beta_s = |\boldsymbol{\beta}_s|$, where $\boldsymbol{\beta}_s$ is the propagation vector in the direction of the scattered wave and \mathbf{e}_s is the unit vector which aligns with the direction of $\boldsymbol{\beta}_s$. The intensity is then the time-averaged value of $\mathbf{E}_s \mathbf{E}_s^*$,

$$I_s = \langle \mathbf{E}_s \mathbf{E}_s^* \rangle \quad (2.18)$$

Inserting Eq. 2.16 into Eq. 2.18 yields:

$$I_s = I_{\text{in}} \frac{\omega^4}{c^4} \frac{\sin^2 \varphi}{\epsilon_0^2 (4\pi R)^2} \int_V \int_V \langle \Delta\epsilon(\mathbf{r}_1', t) \Delta\epsilon(\mathbf{r}_2', t) \rangle e^{j[\boldsymbol{\beta}_{\text{in}} - \boldsymbol{\beta}_s](\mathbf{r}_1' - \mathbf{r}_2')} d\mathbf{r}_1' d\mathbf{r}_2' \quad (2.19)$$

where φ is the angle between the incident light field direction \mathbf{e}_{in} and the propagation vector in the direction of the scattered wave $\boldsymbol{\beta}_s$.

Eq. 2.19 leads to the following observations:

- 1 The intensity of Rayleigh scattering light is proportional to ω^4 , thus inversely proportional to λ^4 ;
- 2 when φ is zero, the scattering intensity is also zero, which means that there is no scattering in the direction orthogonal to the propagation axis of the incident wave.

Since the scatterers are much smaller than the wavelength, the phase component of the integral can be approximated to 1 and $\Delta\epsilon$ can be assumed to be constant within the volume V . The scattering intensity emitted by V is:

$$I_s = I_{\text{in}} \frac{\omega^4 V^2 \sin^2 \varphi}{16\pi^2 R^2 c^4} \frac{\langle \Delta\epsilon^2 \rangle}{\epsilon_0^2} \quad (2.20)$$

Then we can calculate the mean-square fluctuation in the dielectric constant $\langle \Delta\epsilon^2 \rangle$ using the thermodynamic approach, which can be applied to describe the fluctuations in the material properties. The dielectric variation caused by changes of temperature T and density ρ reads:

$$\Delta\epsilon = \left(\frac{\partial\epsilon}{\partial\rho} \right)_T \Delta\rho + \left(\frac{\partial\epsilon}{\partial T} \right)_\rho \Delta T \quad (2.21)$$

In silica fibers, the main contribution to $\Delta\epsilon$ is from the first term, as temperature fluctuations contribute only to less than 2% of its value [30]. Therefore we neglect the temperature contribution and we find:

$$\langle \Delta\epsilon^2 \rangle = \left(\frac{\partial\epsilon}{\partial\rho} \right)^2 \langle \Delta\rho^2 \rangle. \quad (2.22)$$

The subscript T is not retained, and $\langle \Delta\epsilon^2 \rangle$ can be expressed as

$$\langle \Delta\epsilon^2 \rangle = \gamma_e \frac{\langle \Delta\rho^2 \rangle}{\rho_0^2} \quad (2.23)$$

where ρ_0 is the mean density of the material and γ_e is the electrostrictive constant which is defined as:

$$\gamma_e = \left(\rho \frac{\partial \epsilon}{\partial \rho} \right)_{\rho=\rho_0}. \quad (2.24)$$

And $\langle \Delta \rho^2 \rangle / \rho_0^2$ in Eq. 2.23 can be calculated using the law of statistical mechanics and can be described as:

$$\frac{\langle \Delta \rho^2 \rangle}{\rho_0^2} = \frac{K_B T C_T}{V} \quad (2.25)$$

where

$$C_T = -\frac{1}{V} \left(\frac{\partial V}{\partial p} \right) \quad (2.26)$$

is the isothermal compressibility. Insert Eq. 2.23 and Eq. 2.25 into Eq. 2.27, the total intensity of the scattering can be expressed as:

$$I_s = I_{in} \frac{\omega^4 V \gamma_e^2 C_T K_B T \sin^2 \varphi}{16 \pi^2 R^2 c^4 \epsilon_0^2}. \quad (2.27)$$

It should be noted that similar results can be derived from radiation properties of the dipole oscillations [31].

As for the spectrum of Rayleigh scattering, we can consider again Eq. 2.21 and address only the first term the density fluctuation on the right hand, which is the main contribution for $\Delta \epsilon$. The density variations $\Delta \rho$ can be described by entropy s and pressure p fluctuations, which are considered to be two independent variables:

$$\Delta \rho = \left(\frac{\partial \rho}{\partial p} \right)_s \Delta p + \left(\frac{\partial \rho}{\partial s} \right)_p \Delta s \quad (2.28)$$

The first term on the right hand represents adiabatic density fluctuations, which account for Brillouin scattering, while the second term describes isobaric density fluctuations induced by entropy variations which leads to Rayleigh scattering. Here, we only address Rayleigh scattering, hence the entropy fluctuations can be described as [17]:

$$\rho c_p \frac{\partial \Delta s}{\partial t} - \kappa \nabla^2 \Delta s = 0 \quad (2.29)$$

where c_p denotes the specific heat at constant pressure and κ is the thermal conductivity. It should be noted that Eq. 2.29 is a diffusion equation rather than a wave equation, thus it admits a solution in the form:

$$\Delta s = \Delta s_0 E^{-\delta t} e^{-j \mathbf{q} \cdot \mathbf{r}}, \quad (2.30)$$

where δ is the damping rate, which is given by

$$\delta = \frac{\kappa}{\rho c_p} q^2, \quad (2.31)$$

where $q = |\mathbf{q}|$ and \mathbf{q} is the density wave vector. Since the density wave does not propagate, the scattered light has no frequency shift with respect to the incident light. Similar to that of SpBS, $|\mathbf{q}| = 2|\mathbf{k}|\sin(\theta/2)$ ($|\mathbf{k}| \approx |\mathbf{k}'|$) so the width of the scattered light is:

$$\delta\omega_c = \frac{4\kappa}{\rho c_p} |\mathbf{k}|^2 \sin^2(\theta/2). \quad (2.32)$$

In optical fibers, Rayleigh scattering determines the minimum loss limit, in particular for wavelengths shorter than 1600 nm. In standard single mode fiber (SMF), the Rayleigh scattering coefficient is about 0.15 dB/km at a wavelength of 1550 nm, whereas the total loss amounts to 0.2 dB/km.

Rayleigh scattering is regarded as a detrimental phenomenon in optical communication since it is a source of optical loss and induces noise in the signal. However, it gives access to local information of the optical fiber in sensing systems since the backscattered light which carries the local information can be detected from the beginning of the fiber. Rayleigh scattering based optical time-domain reflectometry (OTDR) was first proposed in 1976 [32] and since then the term OTDR often refers to OTDR based on Rayleigh scattering. It has been commercialized and widely used in almost every optical fiber group for the characterization of fibers and fiber links. In recent years, phase-sensitive Rayleigh scattering based sensing systems, not only OTDR but also optical-frequency domain reflectometry (OFDR), have drawn increasing attention since their sensitivity is much higher than that of Brillouin-based and Raman-based DOFS systems[33], demonstrating sensing capabilities for temperature, longitudinal strain and pressure [34, 35, 36].

A more detailed review and introduction on phase-sensitive Rayleigh scattering DOFSs will be given later on.

2.2 Three interrogation schemes on: time, frequency and coherence domains

The most remarkable advantage of distributed optical fiber sensors (DOFSs), which distinguishes it from other optical fiber sensing techniques, is the fact that it provides spatially resolved information from all positions along the fiber. Depending on the method used to acquire local knowledge about a given measurand, DOFS systems can be divided into three categories: optical time-domain reflectometry (OTDR), optical frequency-domain reflectometry (OFDR) and optical coherence-domain reflectometry (OCDR). It should be noted that, most DOFS systems are reflectometers, where the scattered light signals are detected at the

same end of the fiber where the incident light is injected, thus only single fiber end access is required. However, for stimulated Brillouin scattering, there are also DOFS systems that require probe and pump injected to the sensing fiber from different fiber ends. These system are often named *analyzer*, such as BOTDA and BOFDA as mentioned before.

A brief introduction to the operating principles of the aforementioned interrogation schemes is exemplified here below, focusing on Rayleigh-based DOFS.

2.2.1 Optical time-domain reflectometry

First demonstrated in 1976 [32], OTDRs have been developed for fiber link diagnose, intrusion monitoring, acoustic sensing and more applications, but the core of this technique has never been changed. The schematic diagram of a conventional OTDR is illustrated in Fig. 2.7. The probe is an optical pulse, obtained by internal or external modulation of a given light source, which is injected into the fiber under test (FUT) through an optical coupler or a circulator. The backscattered light intensity is converted into electrical voltage by a photodetector and digitized by a data acquisition instrument.

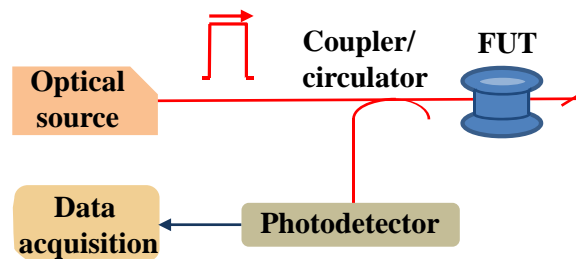


Figure 2.7 – Schematic diagram of OTDR (FUT; fiber under test)

The working principle resembles that of the radar, where radio waves are emitted into the medium (air) and reflected (or scattered) by obstacles. The distance of the detected event from the emitter is calculated through time of flight measurement, i.e. the time delay required for the emitted wave to reach the target and for the scattered wave to reach back the detector. Similarly, OTDR operates by sending intensity-modulated optical waves into the waveguide (fiber). Due to the inhomogeneity of the fiber density or due to various mechanisms (e.g. Fresnel reflections), a portion of the optical pulse gets reflected and/or scattered back and detected. Through time-of-flight evaluation t of the received optical light, the distance d of the event can be precisely estimated $d = v_g t/2$, based on the propagation group velocity of the optical waves in the fiber v_g . Because the distance information is resolved in time domain, the technique is named optical *time-domain* reflectometry.

The power received from Rayleigh backscattered light at the photodetector from a fiber

position z is [37]:

$$P_s = \frac{1}{2} F \alpha_r \nu_g W P_{in} \exp(-2\alpha z), \quad (2.33)$$

where F and α_r are the capture coefficient and Rayleigh scattering coefficient, respectively, P_{in} is the peak power of the input pulse, W is the pulse width and α is the fiber attenuation coefficient which is assumed to be a constant.

From Eq. 2.33 we can see that, as the interrogating pulse travels along the fiber, the pulse power experiences attenuation, thus leading to a decrease of the detected Rayleigh backscattering intensity. A typical schematic OTDR trace in logarithm scale is shown in Fig. 2.8. The slope of the trace divided by 2 is the fiber loss, where the factor 2 comes from the fact that the light travels a round trip in the fiber, hence it experiences twice the fiber attenuation (see the factor $-2\alpha z$ in Eq. 2.33). Any additional reflection or attenuation will be reflected on the trace as a sudden intensity increase or decrease.

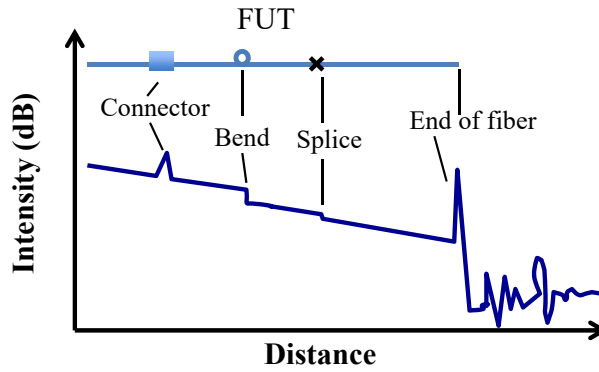


Figure 2.8 – Typical trace of OTDR (FUT: fiber under test)

The spatial resolution of an OTDR system can be expressed as:

$$\Delta z = \frac{cW}{2n_g} \quad (2.34)$$

where n_g is the group refractive index of the fiber.

Thanks to the simple structure of OTDR, this technique has been commercialized as a handy device for the past decades for applications in telecommunication area such as fiber characterization, fiber link diagnosis and so on. Polarization OTDR (POTDR) was proposed in 1981 [38], by measuring the state of polarization (SOP) instead of the intensity of the Rayleigh scattered light. Alternatively, the polarization change is converted into intensity modulation of the light by inserting a polarizer before the photodetector of the conventional OTDR as a simpler case of POTDR. Since the SOP of the probe pulse is very sensitive to the environmental

vibrations along the fiber link, POTDR was applied for distributed fiber sensing to monitor the environmental perturbations (eg intrusions) suffered by the fiber [39]. Phase-sensitive OTDR (ϕ -OTDR), also demonstrating intrusion monitoring, was later proposed using a laser source with a narrow linewidth [40]. Increasing research has been invested in ϕ -OTDR due to its ultra-high sensitivity.

From Eq. 2.34 we can see that the spatial resolution of OTDRs is determined by the pulse width. The shorter the pulse width is, the higher the spatial resolution. However, it can be seen from the Eq. 2.33, that a decrease of the pulse width reduces at the same time the received optical power. This is a classic trade-off existing in OTDRs (and other time-domain based techniques) which limits the dynamic range when high spatial resolution is required.

2.2.2 Optical frequency-domain reflectometry

Optical frequency-domain reflectometry (OFDR) is a technique which retrieves spatial information in frequency domain. It is usually based on a frequency-scanned homodyne interferometer [41]. Fig. 2.9 shows a typical schematic diagram of an OFDR (the polarization effects are ignored for the purpose of simplicity). The interrogating light is frequency scanned and sent to a coupler. The Rayleigh scattered light from the fiber under test (FUT) will then beat with a reference light reflected from a Faraday rotator mirror (FRM) and converted into an electrical signal by a photodetector.

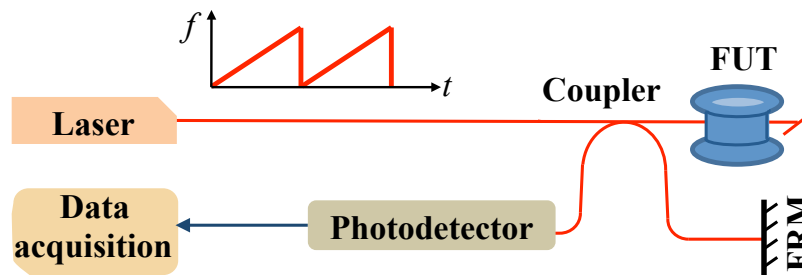


Figure 2.9 – Schematic diagram of OFDR (FUT: fiber under test, FRM: Faraday rotator mirror)

Assume a linearly chirped interrogating light wave at the input of the fiber whose frequency is varying with time:

$$\omega(t) = \omega_0 + \gamma t \quad (2.35)$$

where ω_0 is the carrier frequency and γ the frequency scan rate. The optical field at the photodetector will be the summation of the Rayleigh scattered light from the FUT and the reference. For simplicity, we ignore the fiber loss and the length of the reference arm, so the alternating part of the photo-current from the photodetector resulting from the beating signal

is derived as:

$$\begin{aligned} I_s(t, \tau) &\propto r_e R_r A_0^2 \cos(2\pi\gamma\tau t) \\ &= r_e R_r A_0^2 \cos(2\pi f_b t) \end{aligned} \quad (2.36)$$

where $r_e^2 = F\alpha_r$ is the Rayleigh reflectivity, R_r^2 the reflectivity of the FRM and

$$f_b = \gamma\tau = \gamma \frac{2nz}{c} \quad (2.37)$$

is the beat frequency corresponding to the Rayleigh scattering or reflection and $\tau = \frac{2nz}{c}$ is the round-trip time of the interrogating light scattered from position z ($z \in [0, L]$, L is the length of the sensing arm).

From Eq. 2.37 we can see that the beat frequency of the signal is proportional to the position where scattering takes place, so that position mapping can be obtained from a Fourier transform of the acquired electrical signal:

$$z = \frac{\pi f_b c}{\gamma n} \quad (2.38)$$

The spatial resolution is determined by [42]:

$$\Delta z = \frac{c}{2n\Delta F}. \quad (2.39)$$

Here, $\Delta F = \gamma T_p$ is the frequency scanning range, where T_p is the period of the frequency scan. ΔF can be typically a few tens of GHz, such systems thus enables to reach spatial resolution in the *cm* scale or even lower, which is the most remarkable advantage of OFDR compared with OTDR. However, the sensing fiber length is usually limited to several tens of meters because OFDR requires coherent detection, hence the coherence length of the laser source sets a hard limit to the fiber length. In addition, a broad linearly chirp scan is also required to reach high spatial resolution. Nevertheless, similar to that in OTDR, the period of the light modulation need to be larger than the time of flight of the interrogating light to avoid light overlapping from different operations, thus the modulation period sets a limit to the maximum sensing range, whereas a large linear scan with fast scan rate is difficult to be obtained. OFDR is often used in characterization of optical components or photonic integrated circuits [43, 44]. In recent years, with time-gated interrogating light wave, the measurable range could be extended to more than 100 km, with a moderate spatial resolution in meters range [45].

As for sensing applications, strain sensing based on OFDR was proposed in 1998 [46] by measuring the frequency shift of the Rayleigh scattering spectra. Similarly, distributed temperature sensing can be achieved [47]. Nowadays, many works has been done to extend the sensing length of OFDR, in particular for vibration/acoustic sensing [48, 49].

It should be noted that, thanks to the coherent detection scheme, the sensitivity of the reflectometry is significantly improved compared with any direct detection technique, however,

the state of polarization (SOP) of the back-reflected light has strong effect on the results. In fact, the electric signal amplitude will be zero when the SOPs of the reference and scattered light are orthogonal. Therefore, polarization diversity receivers will be needed, which are based on the splitting of SOP of the reference light to amplify light from both the orthogonal SOPs, respectively [47, 48].

2.2.3 Optical coherence-domain reflectometry

Another instrument capable of determining the positions of the individual reflections is called an optical coherence (or correlation)-domain reflectometer (OCDR), which can achieve spatial resolution in the micrometer range. A typical schematic diagram of OCDR is shown in Fig. 2.10 [50]: a broadband light source is launched into a Michelson interferometer, where the two interferometer arms consist of a device under evaluation (DUE) and a mirror fixed on a movable piezoelectric transducer (PZT). In general, OCDR is a multipath interferometer, and when the time delay from the reflection at a particular location in the DUE equals to the time delay from the reflection of the reference mirror, the interferometer fringes will appear; otherwise, the reflections which are incoherent with the mirror reflection will be converted to phase noise.

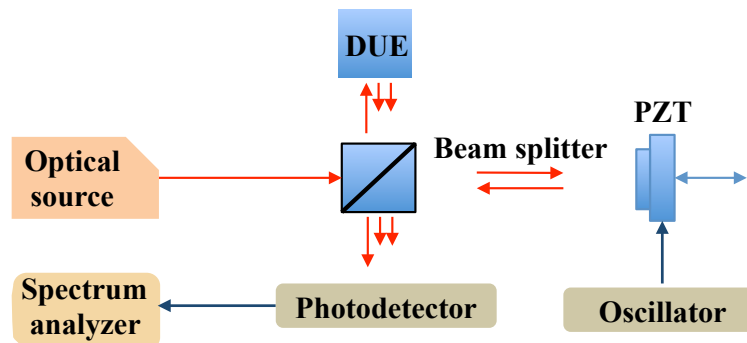


Figure 2.10 – Schematic diagram of OCDR (DUE: device under evaluation)

The spatial resolution of this technique is determined by the width of the coherence envelope, which typically scales inversely with the bandwidth of the optical source, thus it can be so high such that the use is often targeted to optical coherence tomography [51] for noninvasive cross-sectional imaging in biological systems, instead of distributed optical fiber sensing (DOFS).

Instead of mechanically moving the reference mirror to change the optical path, K. Hotate *et al.* proposed an interferometric reflectometry with coherence modulation of the light source through direct frequency modulation [52]. Phase modulation was introduced in the reference arm to synthesise the coherence function [53]. Distributed stress sensors were then demonstrated using polarization maintaining (PM) fiber by measuring the polarization

coupling induced by the lateral stress in the coherence domain^{IV} [54], or using fiber Bragg gratings [55].

Actually, distributed fiber sensing in optical coherence domain is more often used for Brillouin scattering. The spatial information resolving principle is applied in Brillouin-based DOFS, such as Brillouin optical correlation-domain analyzer (BOCDA) [56], where stimulated Brillouin scattering only occurs at a location where the optical probe and pump fulfill the phase matching condition all the time when they meet, the frequency/phase difference between the two otherwise is varying, breaking the phase matching condition. Brillouin optical correlation-domain reflectometry (BOCDR) was also proposed where the SpBs was detected in the coherence domain [57].

2.3 Conclusions

A brief introduction has been given about the scattering process which the distributed optical fiber sensors (DOFS) are often based on, and also the working principles of the DOFS in terms of the spatially resolving methods of the interrogation.

The main focus of this dissertation is on the optical time-domain reflectometry based Rayleigh scattering using a coherent laser with tuneable wavelength. More fundamentals and applications will be introduced in the following chapters.

^{IV}The scheme is actually measuring the interference at the other end of the fiber rather than consisting in a reflectometer

3 Phase-sensitive optical time domain reflectometry

A major part of this thesis is devoted to Rayleigh based optical time-domain reflectometry (OTDR), and in particular to phase-sensitive OTDR, i.e. ϕ -OTDR, due to the following reasons:

- The Rayleigh scattering coefficient is the strongest among all scattering phenomena occurring in optical fibers;
- An OTDR system is simple and only requires access to a single end of an optical fiber;
- The sensitivity of ϕ -OTDR is extremely high.

In this section, a brief review on ϕ -OTDR is provided. Its working principle is explained by developing a 1-D model describing the Rayleigh-induced scattering of a light pulse propagating in an optical fiber. That model is later used to infer the statistical properties of the traces acquired by a ϕ -OTDR. Finally, various implementations of phase demodulation are presented, and particular attention is paid to frequency-scanned ϕ -OTDR, with an emphasis on the sensitivities and other key functional parameters of the system.

3.1 ϕ -OTDR: an overview

The first ϕ -OTDR instrument was proposed by H. F. Taylor *et al.* in 1993 [40]. The system shares certain similarities with interferometry, as it operates by detecting the coherent intensity of the scattered light, enabling to monitor the evolution of the phase of an optical pulse along the fiber. One of the most remarkable advantages of ϕ -OTDR is thus its high sensitivity, which can be intuitively expected since a 2π phase change corresponds to an optical path change of the order of the wavelength, i.e. 1550 nm. Theoretically, the sensitivity of ϕ -OTDR is 1000 times higher than for distributed optical fiber sensors (DOFS) based on Brillouin scattering, such as Brillouin optical time-domain analysis (BOTDA), a technique that has been intensively studied and commercialized for fiber distributed sensing over the past twenty years.

3.1.1 ϕ -OTDR with intensity detection

The first practical application making use of ϕ -OTDR was a distributed intrusion sensor, demonstrated by H.F. Taylor and Chung E. Lee in 1993. Since then, different methods have been proposed to enhance its key specifications: measurement range [58, 59, 60, 61], spatial resolution [62], signal to noise ratio [63, 64, 65], fast dynamic response [66, 67], etc. Based on hybrid distributed amplification, the sensing range of ϕ -OTDR was extended to 175 km [68]. Using pulse stretching and recompression, a spatial resolution of 3 mm was achieved [69]. Frequency division multiplexing was introduced in order to enhance the response bandwidth of the system [70].

A conventional ϕ -OTDR interrogation scheme is shown in Fig. 3.1, which is similar to the OTDR introduced in the previous chapter, except that the low coherence light source is replaced by a high coherence laser with narrow linewidth. The light is intensity-modulated into a pulse before being sent into the fiber. The intensity of the coherent Rayleigh scattered light of the interrogating pulse is measured as it travels along the fiber. Intrusions can be recognized from differential measurement based on successive traces that indicate the vibration-induced strain on the buried fiber.

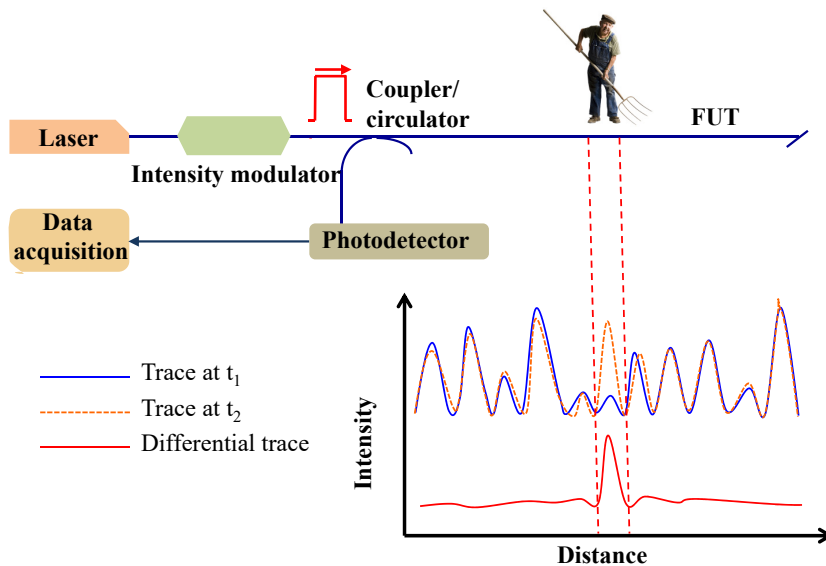


Figure 3.1 – Intrusion sensing based on ϕ -OTDR (traces at t_1 and t_2 are the intensity traces of Rayleigh scattered light obtained before and after the intrusion, respectively)

3.1.2 1-D model of ϕ -OTDR

When a light wave travels along an optical fiber, it continuously experiences scattering throughout its entire propagation. A small fraction of this scattered light is captured back by the fiber and is guided backwards into the direction of the source. The mathematical expression of the

power backscattered by an optical pulse launched into a fiber due to Rayleigh scattering is derived below.

Without loss of generality, we assume a linearly polarized interrogating rectangular light pulse of width W . Furthermore, only the light scattered back along the fiber axis is taken into consideration. Inhomogeneities in the fiber material density scatter the incident light, the partial reflection inducing notably an additional phase change on the scattered field. Assuming that the initial optical field at the beginning of the fiber $z_0 = 0$ is E_0 , we can express the complex amplitude vector of the light reflected from a single scattering point located at a position z as:

$$E_s(z) = E_0 r_e(z) e^{-\alpha z + j\phi(z)} \quad (3.1)$$

where α , $r_e(z)$, and $\phi(z)$ are the fiber loss coefficient, the Rayleigh scattering reflection coefficient and the additional phase change experienced by the incident light, respectively. The phase change is:

$$\phi(z) = \int_0^z \beta(x) dx = 2\pi \frac{\nu}{c} \int_0^z n(x) dx \quad (3.2)$$

where β is the local propagating constant of the fiber and c is the light velocity in vacuum. From Eq. 3.2 we can see that the scattered light $E_s(z)$ at position z is dependent on the optical frequency ν and the refractive index distribution $n(z)$ in the range $[0, z]$.

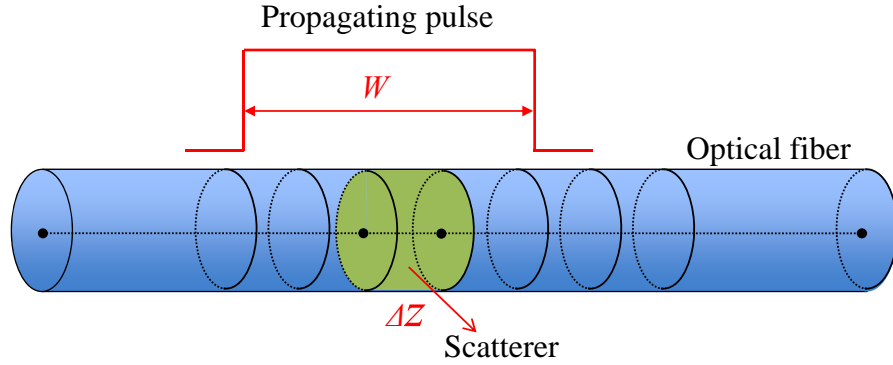


Figure 3.2 – 1 D model of Rayleigh scattering in in the fiber

As shown in Fig. 3.2, the optical fiber is modeled as a unidimensional medium consisting of uniformly distributed scatterers of fixed size Δz for simplicity, but with random density changes and thus refractive index fluctuations. We assume that the refractive index of each scatterer is $n(m) = n_{ave} + \Delta n(m)$, where $n_{ave} (\approx 1.46)$ is the averaged refractive index of the fiber and $\Delta n(m)$ represents the index fluctuation, which is in the order of 10^{-7} . Therefore we can rewrite Eq. 3.1 as a discrete summation rather than a continuous integral, such that the

electric field of the light reflected from the m_{th} scatterer is:

$$E_s(m) = E_0 r_e(z_m) e^{-\alpha m \Delta z + j 2\pi \frac{\nu}{c} \sum_{i=1}^m n(i) \Delta z} \quad (3.3)$$

For a pulse width of W , the backscattered signal received at the fiber beginning at time t is the summation of the individual contribution from every discrete location:

$$E_s(t) = \sum_{m=1}^N E_0 r_e(z_m) e^{-2\alpha m \Delta z + j 2\pi \nu (t - \tau_m)} \text{rect}\left(\frac{t - \tau_m}{W}\right) \quad (3.4a)$$

$$\text{rect}\left(\frac{t - \tau_m}{W}\right) = \begin{cases} 1, & 0 \leq \frac{t - \tau_m}{W} \leq 1; \\ 0, & \text{otherwise.} \end{cases} \quad (3.4b)$$

where $N = L_{tot} / \Delta z$ represents the number of scatterers over the fiber length L_{tot} , and the factor 2 in Eq. 3.4a comes from the fact the light travels a round trip in the fiber. The time delay:

$$\tau_m = 2 \sum_{i=1}^m n(i) \Delta z / c \quad (3.5)$$

is a result of the round-trip time from the beginning of the fiber to the m_{th} scattered point. The optical power at the photodetector then becomes [71]:

$$\mathbb{P}(t) = |E_s(t)|^2 = \mathbb{P}_1(t) + \mathbb{P}_2(t) \quad (3.6a)$$

$$\mathbb{P}_1(t) = \sum_{m=1}^N E_0^2 r_e^2(z_m) e^{-2\alpha m \Delta z} \text{rect}\left(\frac{t - \tau_m}{W}\right) \quad (3.6b)$$

$$\mathbb{P}_2(t) = 2 \sum_{m=1}^N \sum_{k=m+1}^N E_0^2 r_e(z_m) r_e(z_k) \cos(\phi_{mk}) e^{-2\alpha(m+k)\Delta z} \text{rect}\left(\frac{t - \tau_m}{W}\right) \text{rect}\left(\frac{t - \tau_k}{W}\right) \quad (3.6c)$$

where $\phi_{mk} = 2\pi \nu (\tau_m - \tau_k)$. Eq. 3.6b represents the sum of independently scattered waves and is only dependent on the input power as well as the fiber loss, but shows no dependence on the phase of the light, thus exhibits no dependence on the strain and temperature of the fiber or the frequency of the light. $\mathbb{P}_2(t)$ is the term of interest here, as it accounts for the interference between the individual light waves scattered from distinct scatterers within the input pulse width, and causes the jagged appearance of a typical ϕ -OTDR trace. The quantity ϕ_{mk} denotes the phase difference between the backscattered waves from the m_{th} and k_{th} scatterer, and it can be written as

$$\phi_{mk} = \frac{2\pi \nu \sum_{i=m}^k n(i) \Delta z}{c}. \quad (3.7)$$

Environmental perturbations resulting in temperature and/or strain variations will change ϕ_{mk} , yielding a different interference intensity pattern $\mathbb{P}_2(t)$, thus the notion of "phase-sensitive"

technique. From Eq. 3.7 we can see that ϕ_{mk} is proportional to the laser frequency ν , the local refractive index n_i , and the spacing Δz between the scatterers. The scatterers are solidified in the fiber once it is manufactured thus the spaces between scatterers are fixed for a given fiber. Temperature and strain will induce a linear change of the fiber refractive index (on a relatively small range which will be discussed later in more details).

3.1.3 Experimental setup

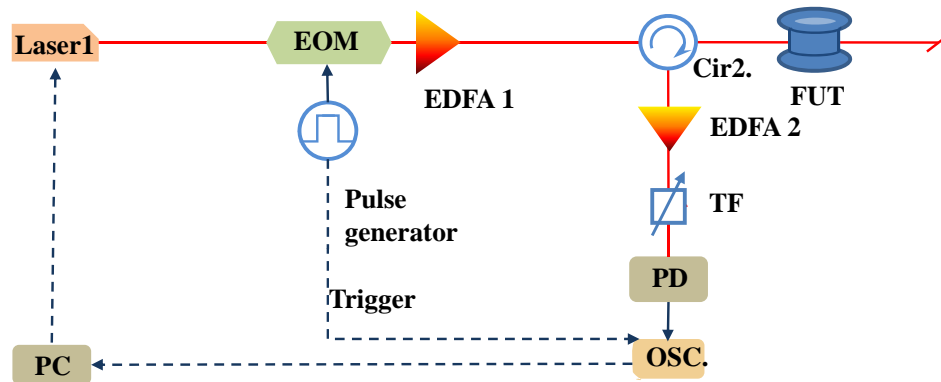


Figure 3.3 – Diagram of a typical ϕ -OTDR setup. (EOM: electro-optic modulator, Cir.: circulator, TF: tunable filter, PD: photodetector, OSC: oscilloscope, PC: personal computer)

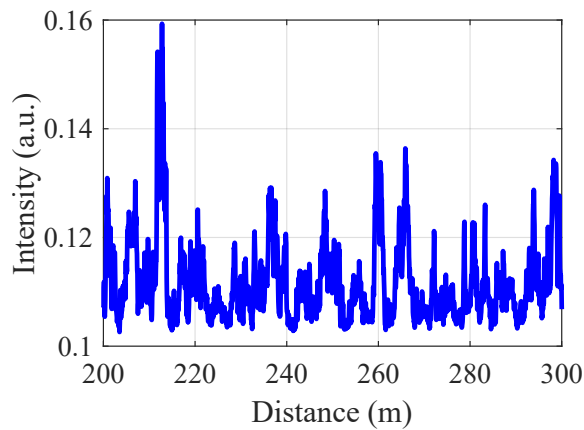


Figure 3.4 – Optical intensity of Rayleigh backscattering light along the fiber distance

A typical ϕ -OTDR setup is shown in Fig. 3.3. A narrow linewidth laser (normally ≤ 1 MHz) is used as the light source. The light is then intensity modulated by an electro-optic modulator (EOM) for pulse shaping and amplified by an EDFA before being sent into the fiber under test (FUT). The back-scattered light is pre-amplified by another EDFA where amplified spontaneous emission (ASE) noise is suppressed by a tunable filter (TF). The optical signal

is then converted to an electrical signal by a photodetector (PD) and sampled by an oscilloscope (OSC.). An example of the obtained intensity trace of the Rayleigh scattering from the fiber is drawn in Fig. 3.4, showing a jagged pattern typical of ϕ -OTDR.

3.1.4 Statistical properties of ϕ -OTDR traces

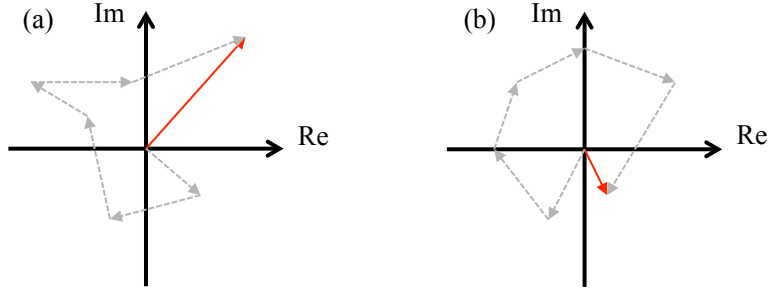


Figure 3.5 – Random walk process of the phase of the Rayleigh scattered light from different scatterers: (a) constructive summation; (b) destructive summation

As described by Eq. 3.6, the electric field of the backscattered signal at a location z is the summation of the electrical field E_s of the Rayleigh-scattered light in the range $[z, z + W/2]$. This coherent summation can be regarded as a random walk process of phasors [72], as shown in Fig. 3.5. The analysis of coherent Rayleigh scattering is thus performed based on the random walk theory [73], with assumptions that are valid for coherent Rayleigh scattering:

- 1 The amplitude and the phase of the reflected light are statistically independent of each other;
- 2 The phase of the scattered light, after wrapping, is considered to be uniformly distributed in the range $[-\pi, \pi]$;
- 3 Both amplitude and phase of the light reflected from the scatterers are statistically independent from one position to another.

We can express the real \Re and imaginary part \Im of the electric field E_s as:

$$\begin{aligned}\Re &= \sum_{m=1}^M |E_s| \cos(\phi_m) \\ \Im &= \sum_{m=1}^M |E_s| \sin(\phi_m)\end{aligned}\tag{3.8}$$

where $M = W/(2\Delta z)$ represents the number of scattering points inside the pulse and ϕ_m is the phase of the scattered light E_s . Both \Re and \Im can be regarded as Gaussian random variables and their variance can be calculated as follows.

From assumption 1 here above we, the expected value of $\sin\phi_m$ and $\cos\phi_m$ is zero, consequently, the expected values for the real and imaginary parts $EV(\Re)$ and $EV(\Im)$ are also zero, since the amplitude and phase are considered to be mutually independent. Besides, the correlation between the real and imaginary parts can be proved to be zero:

$$EV(\Re\Im) = \sum_{m=1}^M EV[|E_s|^2] EV[|\sin(\phi_m)\cos(\phi_m)|] = \sum_{m=1}^M EV[|E_s|^2] EV\left[\frac{1}{2}|\sin(2\phi_m)|\right] = 0 \quad (3.9)$$

Furthermore, since E_s is independent of the positions, the variance of \Re has the following expression:

$$\begin{aligned} \sigma_{\Re}^2 &= EV(R^2) = \sum_{m=1}^M \sum_{k=m+1}^M EV[|E_s(m)||E_s(k)|] EV[|\cos(\phi_m)\cos(\phi_k)|] \\ &= \sum_{m=1}^M EV[|E_s(m)|^2] EV[\cos^2(\phi_m)] \\ &= \frac{1}{2} \sum_{m=1}^M EV[|E_s(m)|^2]. \end{aligned} \quad (3.10)$$

Similarly, the variance of \Im is expressed as:

$$\sigma_{\Im}^2 = \frac{1}{2} \sum_{m=1}^M EV[|E_s(m)|^2], \quad (3.11)$$

which equals σ_{\Re}^2 . Therefore, the joint probability density function (PDF) for \Re and \Im is:

$$\text{PDF}_{\Re,\Im}(\Re, \Im) = \frac{1}{2\pi\sigma_J^2} \exp\left[-\frac{(\Re^2 + \Im^2)}{2\sigma_J^2}\right] \quad (3.12)$$

where $\sigma_J = \sigma_{\Re} = \sigma_{\Im}$. Thus we have

$$\text{PDF}_{E_s,\phi}(E_s, \phi) = \text{PDF}_{\Re,\Im}(\Re, \Im) \left\| \begin{array}{cc} \frac{\partial \Re}{\partial E_s} & \frac{\partial \Re}{\partial \phi} \\ \frac{\partial \Im}{\partial E_s} & \frac{\partial \Im}{\partial \phi} \end{array} \right\| = \frac{E_s}{2\pi\sigma_J^2} \exp\left[-\frac{E_s^2}{2\sigma_J^2}\right] \quad (3.13)$$

where E_s is the amplitude of E_s . Integrating Eq. 3.13 against ϕ from $[-\pi, \pi]$, the PDF of E_s yields:

$$\text{PDF}_{E_s}(E_s) = \int_{-\pi}^{\pi} \text{PDF}_{E_s,\phi}(E_s, \phi) d\phi = \frac{E_s}{2\sigma_J^2} \exp\left(-\frac{E_s^2}{\sigma_J^2}\right). \quad (3.14)$$

Equation (3.14) describes a Rayleigh distribution with a scaling parameter σ_J , which we can be expressed as

$$2\sigma_J^2 = \sum_{i=1}^M EV[E_s^2(i)] = \sum_{i=1}^M EV[I(i)] = M \cdot \bar{I}_s \quad (3.15)$$

where \bar{I}_s is the average intensity of the scattered light within the pulse width. Since the intensity of the Rayleigh scattered light is $I = |E_s|^2$, then the PDF of the Rayleigh scattered light is derived as:

$$\text{PDF}_I(I) = \text{PDF}_{E_s}(\sqrt{I}) \left| \frac{dE_s}{dI} \right| = \frac{1}{2\sqrt{I}} \text{PDF}_{E_s}(\sqrt{I}). \quad (3.16)$$

Combining with Eq. 3.14 and Eq. 3.15 we obtain:

$$\text{PDF}_I(I) = \frac{1}{M \cdot \bar{I}_s} \exp\left(-\frac{I}{M \cdot \bar{I}_s}\right) \quad (3.17)$$

which obeys an exponential distribution. An example of PDF of the Rayleigh scattered light is shown in Fig. 3.6, where the experimental data are obtained using the setup shown in Fig. 3.3 with a pulse width of 10 ns.

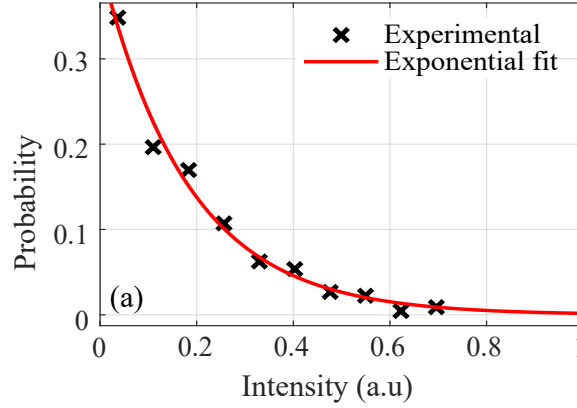


Figure 3.6 – Probability of density function of ϕ -OTDR trace

From Fig. 3.3 we can see that, the probability of low intensity values (close to zero) is high, which means that the signal-to-noise ratio (SNR) is almost zero at most locations. This is the so called fading phenomenon, which was first observed when researchers started to use coherent detection for OTDR systems [74] in 1984. From Eq. 3.6c we can see that the sensing relevant term $\mathbb{P}_2(t)$ is not linearly proportional to the phase ϕ_{mk} , hence quantitative measurements of temperature and/or strain changes require sophisticated phase recovery schemes, which are detailed in the following sections. However, the fading problem mentioned here above will result in failure of the phase demodulation due to the low Rayleigh scattering intensity at many locations. This issue is intrinsic to the random nature of coherent Rayleigh scattering, and can not be simply solved by additional averaging.

According to the random walk process theory, the statistical distribution of the measured power is dependent on the number of degrees of freedom M_f , which corresponds to the number of statistically independent field components. Therefore, in a more general case, the

probability density function can be expressed as [75]:

$$PDF_I(I, M_f) = \frac{(M \cdot \bar{I}_s)^{M_f-1}}{(M_f - 1)!} \left[\frac{M_f}{M \cdot \bar{I}_s} \right]^{M_f} \exp\left(-\frac{M_f I}{M \cdot \bar{I}_s}\right), \quad (3.18)$$

The function obeys a Gamma distribution with shape parameter M_f , which means that if the probe covers a broad band of frequencies (M_f tends to be infinitely large), the PDF of the reflected Rayleigh intensity will converge to a Gaussian distribution centered on the average intensity and with low relative variance. This explains why in incoherent OTDR, where the light source bandwidth is broad, the jag-like pattern typical of coherent OTDR vanishes (see Fig. 2.8). Finally, note that the light polarization state is an additional degree of freedom that reduces the visibility of the noise-like pattern [76].

3.2 ϕ -OTDR with phase demodulation

While initially used to only detect (and locate) the occurrence of induced perturbations along the fiber, ϕ -OTDR has been recently upgraded to quantitatively measure strain [77, 78, 79, 80, 81]. Since local strain/temperature changes induce linear phase variations of the light reflected from the strain/temperature-affected scatterers, the key to a proper retrieval of the strain/temperature variations along the fiber relies on demodulating the phase of the backscattered light. Different methods have been proposed, such as detection using interferometric phase demodulation schemes (e.g. Mach-Zehnder (MZ) interferometer [79] and Michelson interferometer [80]), coherent detection [82, 83] and pulse-engineered schemes [84, 77]. A brief introduction to several phase demodulation schemes is given below.

3.2.1 Interferometric phase demodulation

Phase demodulation using an interferometric scheme for coherent Rayleigh scattering was proposed by Posey *et al.* [35], and the same interferometer was adapted to ϕ -OTDR for distributed and dynamic strain sensing in 2013 [79]. Later on, different interferometric schemes were proposed to directly demodulate the phase of coherent Rayleigh scattering [80, 85]. In general, these techniques rely on sending a conventionally intensity-modulated optical pulse into an optical fiber while a dedicated interferometer located at the receiver demodulates the phase of the backscattered light. All methods have in common to induce a path difference ΔL in the arms of the interferometer, which translates into a time delay $\tau = n\Delta L/c$, yielding the phase difference $\Delta\phi(t) = \phi(t) - \phi(t - \tau)$. Since a single readout of the interferometer does not provide with a unique phase, multiple acquisitions or more advanced techniques such as phase-generated carrier [80] are needed in order to recover unambiguously the phase information. Schematic diagrams of two different interferometric phase demodulation schemes are illustrated in Fig. 3.7.

Fig. 3.7 (a) shows an MZ interferometer consisting of a 2×2 coupler and a 3×3 coupler,

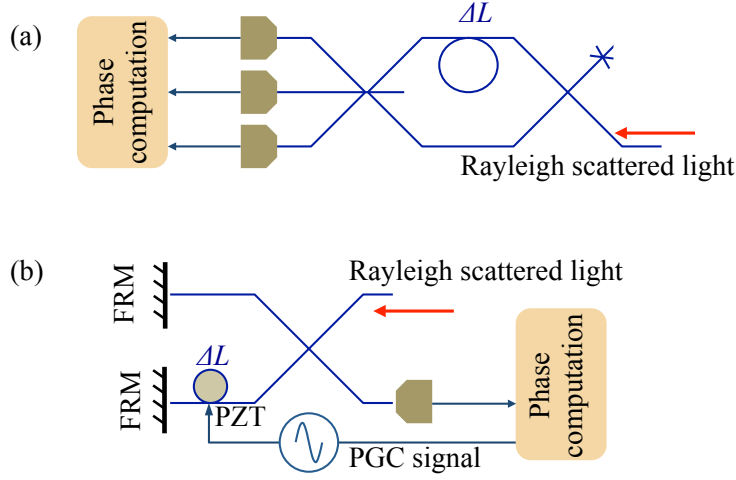


Figure 3.7 – Schematic diagrams of phase demodulation using interferometric receiving schemes: (a) Mach-Zehnder interferometer; (b) Michelson interferometer with phase-generated carrier (PGC). FRM: Faraday rotator mirror; PZT: piezoelectric transducer.

which induce a 120° phase difference between each of the three outputs:

$$I_1 = D + I_0 \cos[\Delta\phi(t)] \quad (3.19a)$$

$$I_2 = D + I_0 \cos\left[\Delta\phi(t) - \frac{2\pi}{3}\right] \quad (3.19b)$$

$$I_3 = D + I_0 \cos\left[\Delta\phi(t) + \frac{2\pi}{3}\right] \quad (3.19c)$$

where D and I_0 are constants. With the knowledge of I_1 , I_2 and I_3 , the phase $\Delta\phi$ can be retrieved unambiguously [86].

Another example to demodulate the phase is shown in Fig. 3.7 (b), adapting a phase-generated carrier (PGC) technique to a Michelson interferometer. A phase modulator driven by a piezoelectric transducer (PZT) is added in one of the interferometer arms to generate specific tones in the detected signal. At the fundamental and first harmonic of the modulation tones, the in-phase and quadrature components are found to be:

$$I(t) = -I_0 J_1(C) \sin[\Delta\phi(t)] \quad (3.20a)$$

$$Q(t) = -I_0 J_2(C) \cos[\Delta\phi(t)] \quad (3.20b)$$

where $J_1(C)$ and $J_2(C)$ are the first and second order Bessel functions of the first kind, respectively, while the phase is demodulated following:

$$\Delta\phi(t) = \text{arctg}\left[\frac{I(t)}{Q(t)}\right]. \quad (3.21)$$

One of the drawbacks of these systems is that at least 2 couplers are needed (in Fig. 3.7 (b) there is only one coupler, however, the signal pass through it twice), which strongly attenuate the signal, so that the power received at the photodetector is usually very low. A relatively long pulse is needed to increase the interrogating pulse energy which limits the spatial resolution to a few meters in general.

3.2.2 Coherent detection

In the past decades, coherent detection has drawn increasing attention within the optical communication community for its capacity to perform phase recovery [87]. It has also been adapted for phase demodulation in ϕ -OTDR, including both heterodyne and homodyne detection, the schematic diagrams of which are shown in Fig. 3.8.

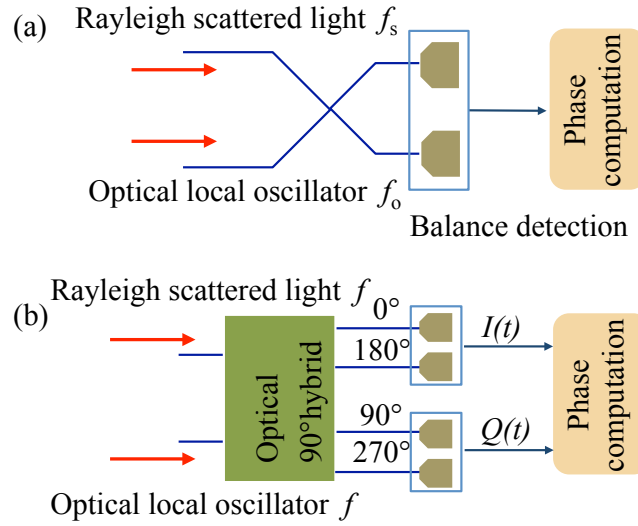


Figure 3.8 – Schematic diagrams of phase demodulation with coherent detection: (a) heterodyne detection; (b) homodyne detection.

One possible implementation for heterodyne detection is shown in Fig. 3.8 (a). The Rayleigh back-scattered light from an optical pulse is mixed with an optical local oscillator (OLO) via a coupler. The resulting beat signal is detected and further processed in order to extract the local phase information. The OLO is a continuous-wave light, which is often generated from the same narrow linewidth laser source as the interrogating pulse, but the frequency of OLO is shifted so that the frequency of the detected beat signal will be $f_b = |f_s - f_o|$. The electric current measured after balanced detection is:

$$I_{\text{hetero}}(t) \propto E_{rs} E_o \cos [2\pi f_b t + \phi(t)]. \quad (3.22)$$

where E_{rs} and E_o are the amplitudes of the Rayleigh scattered light wave and the OLO, respectively. The in-phase and quadrature components can be obtained using the Hilbert transform [88], enabling to recover the phase of the signal using Eq. 3.21 after frequency

down-conversion. It should be noted that, here the phase $\phi(t)$ is actually the phase difference between the Rayleigh scattered light wave and the OLO, i.e. $\Delta\phi(t) = \phi(t) - \phi(t_0)$ where $\phi(t_0)$ is the phase of the OLO, so $\Delta\phi(t)$ will accumulatedly increase along with the fiber length. Therefore, phase unwrapping algorithms [82] need to be implemented. In fact, the actual quantity of interest, is the differential phase $\Delta\phi(t) - \Delta\phi(t) - \tau$ across a certain distance interval (the gauge length ΔL and $\tau = 2nL/c$), which can be obtained by a simple subtraction.

A possible implementation of homodyne detection using optical 90° hybrid is shown in Fig. 3.8 (b). Here the frequencies of the Rayleigh scattering light and the OLO are the same. Both the signal and the OLO are splitted into two beams and one signal beam beats with one OLO beam directly to obtain the in-phase $I(t)$ component; as for the other two beams, a 90° phase shift is induced in the OLO arm in order to get the quadrature components $Q(t)$.

The main advantage of coherent detection is that it provides phase recovery with high signal-to-noise ratio, since the detected electric current is proportional to the OLO amplitude. However, it suffers from several drawbacks:

- It requires a light source with high coherence;
- The phase noise accumulates all long the fiber [89];
- It suffered from the fading problems as mentioned before [90]. Additionally, it also suffers from polarization fading (the beating signal tends to be zero when the polarization states of the OLO and the scattering light are orthogonal with respect to each other).

To avoid the problems listed hereabove, pulse engineered schemes have been proposed, and the upcoming section is devoted to provide the main concepts related to this technique.

3.2.3 Pulse-engineered ϕ -OTDR

Instead of modifications on the receiving part of conventional intensity-based ϕ -OTDR, methods of engineering the interrogating pulse were proposed to retrieve the phase information, such as dual-pulse schemes [84, 91, 92] and chirped-pulse schemes [93].

In dual pulse implementation, two pulses with different carrier frequencies (or $\pi/2$ shifted phase) are launched into the fiber, and the backscattered signal is acquired via heterodyne (or homodyne I/Q) detection. Since the optical local oscillator (OLO, one of the pulses) is propagating together with the signal (the other pulse), both pulses experience the same optical path. As a consequence, many detrimental effects common to both pulses such as phase noise and environmental perturbations are canceled out.

As for chirped-pulse implementation, the technique relies on imposing a linear chirp on the interrogating pulse [93] prior to its injection into the sensing fiber. Let us assume that the

frequency profile of the linear chirped pulse is

$$\nu(t) = \nu_0 + \left(\delta\nu/2 - \frac{\delta\nu}{W} t \right), \quad (3.23)$$

which has a central frequency of ν_0 , a spectral width of $\delta\nu$ and frequency chirp rate of $\delta\nu/W$. Injecting 3.23 in Eq. 3.7, the phase term of the Rayleigh backscattered light becomes:

$$\phi_{mk} = \frac{2\pi \sum_{i=m}^k n(i) \Delta z}{c} \left(\nu_0 + \frac{\delta\nu}{2} - \frac{\delta\nu}{W} t \right) \quad (3.24)$$

Therefore the phase change induced by external temperature or/and strain can be derived as:

$$\Delta\phi_{mk} = - \frac{2\pi \sum_{i=m}^k n(i) \Delta z}{c} \left(\frac{\delta\nu}{W} \right) \Delta t \quad (3.25)$$

which means that the phase change experienced by the pulse due to the fiber refractive index change is reflected by a time delay Δt in the measured Rayleigh scattering trace. The sensitivity reads:

$$\left(\frac{\Delta n}{n_{ave}} \right) = \left(\frac{1}{\nu_0} \right) \left(\frac{\delta\nu}{W} \right) \Delta t \quad (3.26)$$

where Δn is the equivalent refractive index change induced by the targeted measurand variations, e.g. temperature and strain, while Δt can be obtained through cross correlation^I of the obtained Rayleigh scattered traces.

The above mentioned pulse-engineered methods exhibit the solid advantage of avoiding the need for stringent stabilization (acoustic and thermal isolation) of an interferometer as well as of releasing the requirement on the linewidth of the laser source used in coherent detection schemes. The fading problem is also eliminated here since the phase change is not retrieved from the Rayleigh scattering of a single position (which can be low). Instead, the phase change is retrieved from the time delay of the Rayleigh scattering pattern, where statistically the intensity can not be always low as long as the pulse power is high enough. However, the bandwidth required at the receiver is the same as for coherent detection, which restricts the maximum measurable strain/temperature range. The spatial resolution is also often limited to meter range due to the weak intensity of the Rayleigh scattered light. To achieve high spatial resolution and improved sampling rate, phase demodulation techniques using pulse engineered schemes are often paired with coherent detection [78, 81].

3.3 Frequency-scanned ϕ -OTDR

Alternatively, instead of implementing complex phase demodulation schemes, the phase shift of the signal can be retrieved by sweeping the carrier frequency of optical pulse sent into the

^IDetails about cross correlation will be given in the next chapter.

fiber. As detailed in the following section, variations of the refractive index due to environmental changes can be compensated by a frequency shift. Therefore, the phase change of an optical pulse traveling along a fiber can be estimated by comparing two spectral distributions at each location and estimate their frequency shift. Conventionally, cross correlation is utilized for the frequency shift estimation, therefore, this technique is known as correlation-based optical time domain reflectometry (COTDR). However, in the literature, COTDR is also sometimes referring to OTDR with coherent detection. To avoid any confusion, we will refer in this manuscript to ϕ -OTDR based on frequency shift (FS) retrieval as frequency-scanned ϕ -OTDR.

3.3.1 Working principle

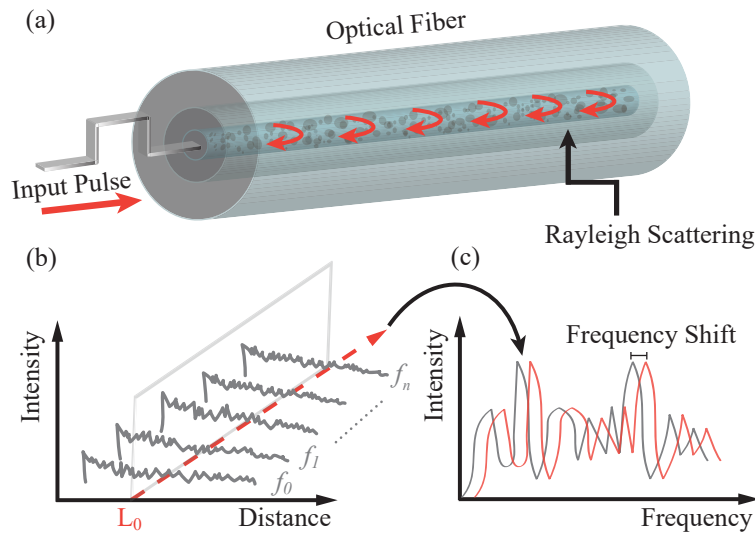


Figure 3.9 – Principle of frequency-scanned ϕ -OTDR: (a) conceptual view of interrogation in frequency-scanned ϕ -OTDR; (b) Intensity of Rayleigh backscattered traces for the different scanning optical frequencies; (c) Rayleigh spectra of reference and measurement showing the strain/temperature-induced frequency shift at position L_0 .

Conventional operation of frequency-scanned ϕ -OTDR requires acquiring Rayleigh scattering intensity traces as a function of the input laser frequency within a given range. The refractive index distribution is fixed along the fiber once for ever after solidification such that, at a given position and under stable experimental conditions, the measured intensity as a function of frequency will be repeatable and can be regarded as a reference spectrum. When the fiber is subjected to any strain or temperature change, this local spectrum will experience a frequency shift induced by the refractive index variation, as illustrated in Fig. 3.9. By performing a cross-correlation operation between the newly measured local spectral response and the reference spectrum will result in a correlation peak located at a frequency shift proportional to the local temperature and strain variations. The proportionality relation is directly function of the thermo-optic and elasto-optic responses of silica, and is strictly equal to the coefficients scaling the spectral response of fiber Bragg gratings.

Assuming that the phase change due to temperature and strain variations is $\Delta\phi_{ik}$, it can be compensated completely when the optical frequency of the interrogating pulse is shifted by $\Delta\nu$ such that:

$$\Delta\phi_{mk} = \frac{2\pi n(z_m - z_k)}{c} \Delta\nu \quad (3.27)$$

Here we replace n_{ave} by n for simplicity. From Eq. 3.27 we can see that, the phase change is linearly proportional to the frequency shift $\Delta\nu$ in the Rayleigh backscattering spectra.

3.3.2 Experimental setup

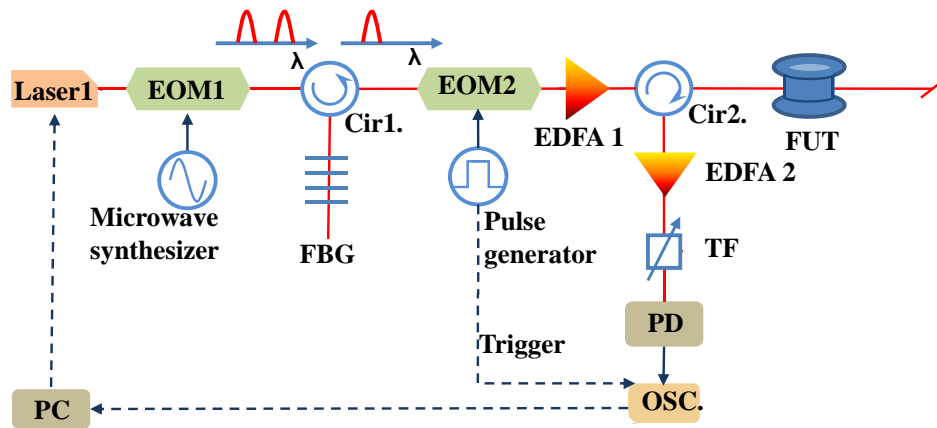


Figure 3.10 – Diagram of a typical ϕ -OTDR setup. (EOM: electro-optic modulator, Cir.: circulator, TF: tunable filter, PD: photodetector, OSC: oscilloscope, PC: personal computer, FBG: fiber Bragg grating)

A frequency-scanned ϕ -OTDR setup is shown in Fig. 3.10. The only conceptual change compared with a conventional single-frequency ϕ -OTDR, is the insertion of a frequency scanning section, which is implemented by a two-sidebands modulator (EOM1) followed by an optical filter (Fiber Bragg grating) to suppress one of the sidebands (as shown in Fig. 3.10). Alternatively, the frequency scanning function can be realized by inserting a single sideband modulator or by direct tuning of the laser frequency.

Experimental time-domain acquisition at a fixed frequency and frequency-domain spectra at a fixed position are shown in Fig. 3.11 and both traces show jagged patterns typical of ϕ -OTDR.

Eq. 3.17 is derived assuming a single optical frequency, a single mode fiber and only one polarization mode. For a fixed position, the spectra of the frequency-scanned ϕ -OTDR also obeys an exponential decay distribution, since the number of degrees of freedom is the same

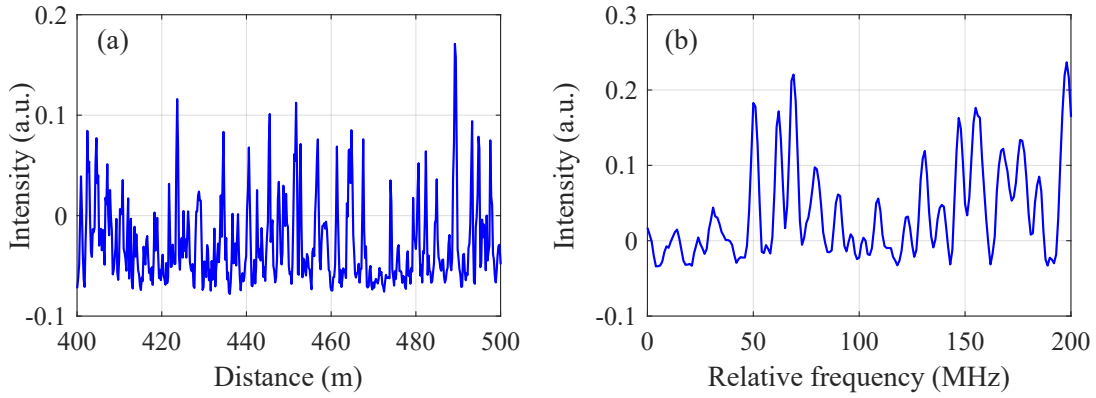


Figure 3.11 – Experimental traces of frequency-scanned ϕ -OTDR: (a) time-domain trace (distribution along distance); (b) frequency-domain trace. The data are obtained with a 10 ns pulse width, which corresponds to a spatial resolution of 1 m.

as in Eq. 3.18. The PDF of a typical spectrum obtained using frequency-scanned ϕ -OTDR is compared with an exponential decay fit in Fig. 3.12, showing excellent agreement.

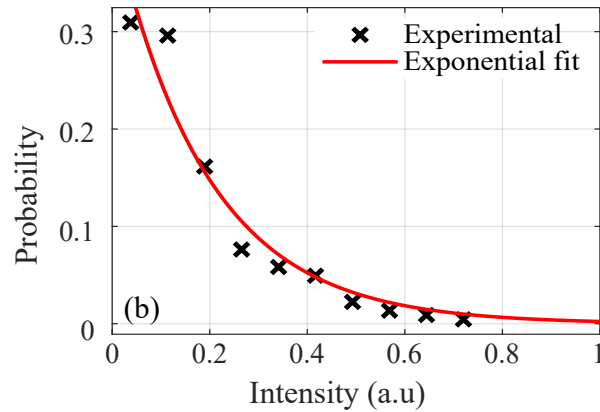


Figure 3.12 – Probability of density function of a spectra obtained from the frequency-scanned ϕ -OTDR at a certain position

3.3.3 Temperature, strain and pressure sensitivities

To calculate the sensitivity of frequency-scanned ϕ -OTDR, let us recall Eq. 3.7. For simplicity, we can replace the optical path $n_{ave}(k-m)\Delta z$ by nL , and rewrite the phase of the travelling light 3.7 in more general terms as:

$$\phi = \frac{2\pi\nu nL}{c} \quad (3.28)$$

Similar to fiber Bragg gratings (FBGs), environmental perturbations (temperature, strain, pressure change and so on) modify the phase ϕ of the travelling light through different influences. In this subsection the sensitivities of standard single mode fibers (SMF) to the aforementioned quantities are derived.

Temperature sensitivity

There are two effects accounting for the temperature induced phase change $\Delta\phi_T$ of the light travelling in an optical fiber: the change in fiber length due to thermal expansion (or contraction) and the temperature-induced refractive index change (thermo-optic effect) [94]. The overall phase change reads:

$$\frac{\Delta\phi_T}{\Delta T} = \frac{2\pi\nu nL}{c} \left(\frac{1}{L} \frac{dL}{dT} + \frac{1}{n} \frac{dn}{dT} \right) \quad (3.29)$$

where T in all terms denotes the temperature. Here we ignore variations in the fiber diameter. In Eq. 3.29, the first term represents the thermal expansion associated to the temperature dependent coefficient $\frac{1}{L} \frac{dL}{dT}$. An experimental result for a specimen of fused silica (SRM 793; BY US NIST) is shown in Fig.3.13, and the sampled data points are interpolated as follows [95]:

$$\frac{1}{L} \frac{dL}{dT} (10^6 K) = a(b/T)^c \frac{\exp(b/T)}{[\exp(b/T) + 1]^2} + d(e/T)^2 \frac{\exp(e/T)}{[\exp(e/T) - 1]^2} \quad (3.30)$$

where: $a = -4.22 \pm 0.04$, $b = 35.5 \pm 0.8$, $c = 0.335 \pm 0.015$, $d = 1.253 \pm 0.022$ and $e = 535 \pm 9$.

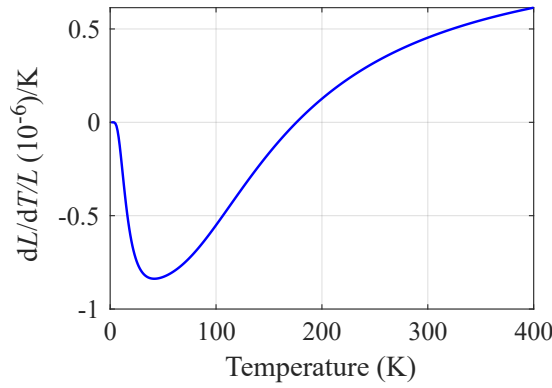


Figure 3.13 – Thermal expansion coefficient of fused silica SRM 739

As for the thermo-optic coefficient $\frac{1}{n} \frac{dn}{dT}$, it is both frequency (or wavelength) and temperature dependent. A widely used model to describe the refractive index with respect to temperature and wavelength for optical glass is the Sellmeier model [96]:

$$n^2(\lambda, T) - 1 = \sum_{i=1}^3 \frac{S_i(T)\lambda^2}{\lambda^2 - \lambda_i^2(T)} \quad (3.31)$$

where λ is the optical wavelength^{II}. S_i and λ_i are the strength and central wavelength of the resonance features in the material, respectively, and can be written as:

$$S_i(T) = \sum_{j=0}^4 S_{ij} T^j \quad (3.32a)$$

$$\lambda_i(T) = \sum_{j=0}^4 \lambda_{ij} T^j \quad (3.32b)$$

The corresponding parameters for Corning 7980 fused silica, which are valid over a temperature range of [30 K, 300 K] and over a wavelength range of [0.4 μm , 2.3 μm], are listed in Table 3.1. By inserting all the above-mentioned parameters in Eq. 3.30 and Eq. 3.31, the thermal expansion coefficient γ_T and thermo-optic coefficient β_T at room temperature (25 °C) for an operating wavelength of 1550 nm can be calculated approximately to be:

$$\gamma_T = \frac{1}{L} \frac{dL}{dT} = 4.5 \times 10^{-7} \text{ K}^{-1} \quad (3.33a)$$

$$\beta_T = \frac{1}{n} \frac{dn}{dT} = 2 \times 10^{-5} \text{ K}^{-1} \quad (3.33b)$$

In general, the thermal expansion coefficient γ_T is 2 orders of magnitude lower than the

j	S_{1j}	S_{2j}	S_{3j}
$j=0$	1.101227	1.78752×10^{-5}	7.93552×10^{-1}
$j=1$	-4.94251×10^{-5}	4.76391×10^{-5}	-1.27815×10^{-3}
$j=2$	5.27414×10^{-7}	-4.49019×10^{-7}	1.84595×10^{-5}
$j=3$	-1.59700×10^{-9}	1.44546×10^{-9}	-9.20275×10^{-8}
$j=4$	1.75949×10^{-12}	-1.57223×10^{-12}	1.48829×10^{-10}
j	λ_{1j}	λ_{2j}	λ_{3j}
$j=0$	-8.90600×10^{-2}	2.97562×10^{-1}	9.34454
$j=1$	9.08730×10^{-6}	-8.59578×10^{-4}	-7.09788×10^{-3}
$j=2$	-6.53638×10^{-8}	6.59069×10^{-6}	1.01968×10^{-4}
$j=3$	7.77072×10^{-11}	-1.09482×10^{-8}	5.07660×10^{-7}
$j=4$	6.84605×10^{-14}	7.85145×10^{-13}	8.21348×10^{-10}

Table 3.1 – Parameters in the Sellmeier model for Corning 7980 fused silica[96]

thermo-optic coefficient β_T for silica glass (as shown in Fig. 3.14). Therefore, the thermal-expansion coefficient can be usually neglected, except at very low temperature, since the thermo-optic coefficient drops with temperature while the thermal expansion coefficient becomes negative when $T < 175 \text{ K}$.

As for the temperature sensitivity for frequency-scanned ϕ -OTDR, what we are interested in is often the frequency shift induced by temperature since the sensor is based on frequency shift measurement. A typical value for the temperature sensitivity for frequency-scanned

^{II}In the approximation, S_i and λ_i have no real physical meaning, but is used to generate an adequately accurate fit to empirical data. The value of the wavelength inserted in the equation for estimation should be in units of μm

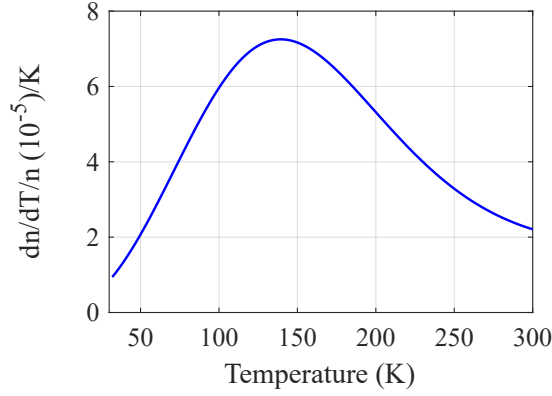


Figure 3.14 – Thermo-optic coefficient at wavelength 1550 nm

ϕ -OTDR is:

$$\frac{\Delta\nu}{\Delta T} = \frac{\nu}{n} \frac{dn}{dT} \approx 1.33 \text{ GHz/K} \quad (3.34)$$

Later on, the strain sensitivity will be calculated and we can see that the sensitivity of frequency-scanned ϕ -OTDR is more than 1000 times larger than that of BOTDA (see Eq. 2.9), which distinguishes the frequency-scanned ϕ -OTDR as an interrogation with ultra-high sensitivity.

Longitudinal strain sensitivity

We now consider the phase change caused by longitudinal strain (strain along the fiber axial direction) $\varepsilon = \frac{\Delta L}{L}$. The strain dependent phase change is written as [97]:

$$\Delta\phi_s = \frac{2\pi\nu}{c}(n\varepsilon L + L\Delta n(\varepsilon)). \quad (3.35)$$

where the first term represents the physical length change and the second term accounts for strain-induced refractive index changes (strain-optic effect), respectively. The waveguide mode dispersion effect due to changes in the fiber diameter is negligible and ignored here. The strain-optic effect is described by the optical indicatrix:

$$\Delta\left(\frac{1}{n^2}\right)_i = \sum_{j=1}^6 p_{ij} \mathbb{S}_j. \quad (3.36)$$

Here p_{ij} is the photo-elastic tensor and \mathbb{S}_j is the strain vector. The subscripts are in the standard contracted notation. In this section, we consider only the longitudinal strain and the strain vector is represented as below:

$$\mathbb{S}_j^T = \begin{bmatrix} \varepsilon & -\mu\varepsilon & -\mu\varepsilon & 0 & 0 & 0 \end{bmatrix} \quad (3.37)$$

where μ is the Poisson ratio of the material. For a homogeneous isotropic medium such as silica glass, the strain-optic tensor p_{ij} can be written as:

$$p_{ij} = \begin{bmatrix} p_{11} & p_{12} & p_{12} & 0 & 0 & 0 \\ p_{12} & p_{11} & p_{12} & 0 & 0 & 0 \\ p_{12} & p_{12} & p_{11} & 0 & 0 & 0 \\ 0 & 0 & 0 & p_{44} & 0 & 0 \\ 0 & 0 & 0 & 0 & p_{44} & 0 \\ 0 & 0 & 0 & 0 & 0 & p_{44} \end{bmatrix} \quad (3.38)$$

where $p_{44} = (p_{11} - p_{12})/2$. Therefore the change in the optical indicatrix induced by longitudinal strain is:

$$\Delta\left(\frac{1}{n^2}\right)_{x,y} = \varepsilon(1 - \mu)p_{12} - \mu\varepsilon p_{11} \quad (3.39)$$

The refractive index change can then be written as:

$$\begin{aligned} \Delta n(\varepsilon) &= -\frac{1}{2}n^3\Delta\left(\frac{1}{n^2}\right)_{x,y} \\ &= -\frac{1}{2}n^3[\varepsilon(1 - \mu)p_{12} - \mu\varepsilon p_{11}]. \end{aligned} \quad (3.40)$$

Replacing Δn in Eq. 3.35 with Eq. 3.40 we get:

$$\Delta\phi_s = \frac{2\pi\nu n L \varepsilon}{c} \left\{ 1 - \frac{1}{2}n^2[(1 - \mu)p_{12} - \mu p_{11}] \right\}. \quad (3.41)$$

Assuming that the phase change induced by the longitudinal strain can be compensated by a frequency shift $\Delta\nu$, and using typical parameters for silica glass, i.e. $n=1.5$, $\mu=0.17$, and $p_{11}=0.11$, $p_{12}=0.25$, the sensitivity of the frequency-scanned ϕ -OTDR can be derived as:

$$\frac{\Delta\nu}{\varepsilon \times 10^{-6}} = \nu \left\{ 1 - \frac{1}{2}n^2[(1 - \mu)p_{12} - \mu p_{11}] \right\} = 152.44 \text{ MHz}/\mu\varepsilon. \quad (3.42)$$

Pressure sensitivity

We consider the effect of an isotropic stress induced by a pressure P . Eventually yielding a longitudinal strain, the phase change caused by pressure can be represented as [94]:

$$\Delta\phi_P = \frac{2\pi\nu}{c}(n\varepsilon L + L\Delta n) \quad (3.43)$$

Again, the first term is the change in the fiber physical length, while the second term is the refractive index change due to strain. Variations in the waveguide are once more ignored.

Assuming no shear stress (hydrostatic pressure), the stress tensor reduces to:

$$\sigma = \begin{bmatrix} -P \\ -P \\ -P \end{bmatrix}. \quad (3.44)$$

The strain vector is then:

$$\varepsilon = \begin{bmatrix} \varepsilon_x \\ \varepsilon_y \\ \varepsilon_z \end{bmatrix} = \begin{bmatrix} -P(1-2\mu)/E \\ -P(1-2\mu)/E \\ -P(1-2\mu)/E \end{bmatrix}. \quad (3.45)$$

Here E is the Young's modulus of glass. The first term on the right-hand side of Eq. 3.43 reads,

$$n\varepsilon L = -nLP(1-2\mu)/E. \quad (3.46)$$

As for the strain-optic effect, the optical indicatrix is given by Eq. 3.36. Without shear strain, the strain-optic tensor is:

$$p_{ij} = \begin{bmatrix} p_{11} & p_{12} & p_{12} \\ p_{12} & p_{12} & p_{12} \\ p_{12} & p_{12} & p_{11} \end{bmatrix}. \quad (3.47)$$

Thus we can derive the change in optical indicatrix as:

$$\begin{aligned} \Delta\left(\frac{1}{n^2}\right)_{x,y,z} &= (1-2\mu)p_{11}P/E - 2(1-2\mu)p_{12}P/E \\ &= (1-2\mu)(p_{11} + 2p_{12})P/E \end{aligned} \quad (3.48)$$

Therefore, the refractive index change in the z direction (longitudinal direction) is:

$$\begin{aligned} \Delta n &= -\frac{1}{2}n^3\Delta\left(\frac{1}{n^2}\right)_{x,y} \\ &= \frac{1}{2}n^3(1-2\mu)(p_{11} + 2p_{12})P/E \end{aligned} \quad (3.49)$$

Inserting Eq. 3.49 and Eq. 3.46 into Eq. 3.43, we can calculate the phase change induced by the pressure P :

$$\Delta\Phi_P = \frac{2\pi\nu nL}{c}(1-2\mu)\left[\frac{1}{2}n^2(p_{11} + 2p_{12}) - 1\right]\frac{P}{E} \quad (3.50)$$

The Young's modulus of glass is typically about 7.1×10^{10} N/m². The sensitivity of a frequency-scanned ϕ -OTDR to an external pressure is therefore

$$\frac{\Delta\nu}{P} = \frac{(1-2\mu)\frac{1}{2}n^2(p_{11} + 2p_{12}) - 1}{E} \approx -1.49 \text{ kHz/Pa} \quad (3.51)$$

Since the Young's modulus of fused silica is fairly large, conventional fibers are normally not very sensitive to pressure, compared e.g. with their sensitivity to temperature. It should be noted that the effect of the coating is not considered in the calculation, while it does actually impact the sensitivity. Therefore, polymer-coated fibers have a higher demonstrated pressure sensitivity [98, 99]. In order to further improve the sensitivity, specially designed fibers are needed, such as fibers with air holes in the cladding which overall reduce the equivalent Young's modulus of the fiber [100, 101].

3.3.4 Key criteria of the interrogator

For any distributed fiber sensing interrogator, key criteria include, among others, sensing distance, spatial resolution, acquisition time (or sampling rate inversely) and dynamic range. The limits of these parameters are introduced briefly in this section.

Sensing distance

Of all parameters, the sensing distance is one of the most crucial, as it defines the maximum length of the sensing fiber the system can measure. It is directly linked to the signal-to-noise ratio (SNR) of the remotest monitoring point. The signal power is related to many aspects, such as the interrogation pulse energy, the Rayleigh reflectivity, the fiber loss, etc. The total noise from a given system may originate from various sources, i.e. the phase noise of the interrogation light [89], the light leakage from the optical modulation [102], the amplified spontaneous emission (ASE) noise from the optical amplification and finally the thermal and shot noise from the photodetector. For standard single-mode fiber, the Rayleigh reflectivity and fiber loss is fixed, therefore the received power is mainly limited by the pulse energy. To increase the pulse energy, one can increase either the peak power of the optical pulse and/or the pulse duration. However, on one hand, the peak power of the optical pulse is limited to the threshold of nonlinear optical effects, so that it has to be kept below a certain value, especially for long fibers. In ϕ -OTDR, the input power of the pulse is limited to be ~ 100 mW by modulation instability (MI) [103], which is usually the first nonlinear optical effect to arise. The net effect of MI is to broaden the spectrum of the optical signal, thus lowering the coherence of the Rayleigh scattered light, leading to a localized fading of the recorded interference pattern; on the other hand, the pulse duration determines the spatial resolution (which will be discussed after) thus must be kept shorter than a given width in order to fulfill the requirement on the spatial resolution.

Over the years, several strategies have been developed in order to further extend the maximum sensing distance of ϕ -OTDR and/or other interrogation schemes. For instance, distributed fiber amplification has been introduced to compensate for the attenuation of the interrogating pulse [68]. Coherent detection is also beneficial to amplify the signal and reach shot noise limited regime at the photodetector, thus improving the SNR [63]. Recently, backscattering enhanced fibers have been proposed [104], demonstrating a scattering coeffi-

cient 10 dB higher than conventional fibers, enabling to extend the sensing distance.

Spatial resolution

The spatial resolution is the minimum distance between two events taking place along the fiber enabling to distinguish them. Similar to any other OTDRs, the spatial resolution in ϕ -OTDR is determined by the duration of the interrogating pulse, which is illustrated in Fig 3.16.

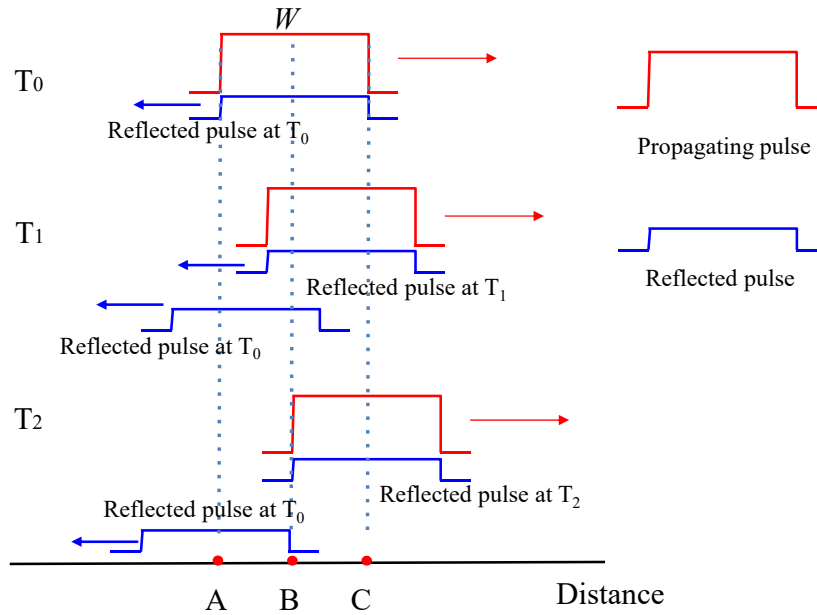


Figure 3.15 – Illustration of the spatial resolution of OTDRs

Let us consider a propagating optical pulse with a duration of W . Assume that at time T_0 , the pulse leading and trailing edges are at point C and A respectively. Through Rayleigh scattering, the incident pulse generates a backward propagating reflected pulse. As the incident pulse continues to propagate in the fiber, the newly generated reflected pulse at time T_1 will overlap with the reflected pulse generated at T_0 (shown in Fig. 3.16). Due to the counter-propagating motion, it is not until a time T_2 corresponding to half of the pulse duration that the reflected pulse generated at T_0 is completely spatially separated from the incident pulse. Therefore, the reflected pulses can only be discriminated when they are generated with a time difference larger than $T_2 - T_0 = W/2$. Thus the spatial resolution is:

$$\Delta Z = \frac{W}{2} \frac{c}{n} = \frac{Wc}{2n} \quad (3.52)$$

where c is the light speed in vacuum and n is the refractive index. From Eq. 3.52, we can see that ΔZ is proportional to W . A pulse duration of 10 ns corresponds to a spatial resolution of 1 m approximately, assuming the refractive index of the fiber is 1.5. In real applications, a shorter spatial resolution is generally preferred together with a large sensing distance. The

decrease of the pulse duration will enhance the spatial resolution but reduce the pulse energy, hence limit the sensing range. This trade-off between spatial resolution and sensing range is general, and applies to any OTDR system.

Dynamic range

The dynamic range here is the maximum acquirable range of the measurands (e.g. temperature, strain etc.) of interest, which is directly linked in frequency scanning ϕ -OTDR to the extent of the frequency scan. As mentioned before, the phase change caused by any measurand will induce a frequency shift in the Rayleigh spectra, which can be retrieved by proper frequency estimation algorithm.

Quite naturally, cross-correlation seems at first indicated to identify this frequency shift as the position corresponding to the maximum of the cross correlation spectrum[71]. The estimation relies on the cross-correlation between the reference and the subsequent measured traces. If the frequency shift in the spectra is so large that the spectra pattern has moved out of the reference scanned window, no correlation will be found between the traces, thus resulting in the failure of the frequency estimation. The reference scanned window, i.e. the frequency scanning range, thus determines the maximum measurable range. An empirical approximation is that the maximum frequency shift can be half of the scanning range, as the spectrum might shift towards both spectral directions. However, from an estimation error analysis performed in the next chapter, it appears that at high spatial resolution, the allowable frequency shift is much less than this "half range approximation".

Measurement time

The measurement time of frequency-scanned ϕ -OTDR can be written as:

$$T_m = N(\mathbb{N}_{\text{ave}} T_p + t_s) \quad (3.53)$$

where \mathbb{N}_{ave} is the number of averaging, N is the number of scanned frequency, T_p is the period of the optical pulse (the inverse of the repetition rate) and t_s is the frequency switch latency.

There is a minimum requirement for the optical pulse period since the second pulse can not be sent to the fiber until the Rayleigh scattering light of the previous pulse at the remotest sensing position has arrived at the beginning of the fiber, making sure to prevent any overlapping between the backscattered signals from the different pulses. This period T_p must be larger than the time of flight of the optical pulse in the fiber, i.e. $T_p > t_f$ has to be satisfied where

$$t_f = \frac{2nL_{\text{tot}}}{c}. \quad (3.54)$$

Here L_{tot} is the total fiber length. For a fixed frequency scan step, the number of scanned

frequency N is proportional to the frequency scan range. This comes as an additional trade-off between the measurable range and the measurement time in frequency-scanned ϕ -OTDR.

3.3.5 Two main sources of noise

As mentioned in the last section, there are many different noise sources that will impact the SNR and decrease the measurement accuracy and sensing distance. The impact of two different noise sources, which are the most relevant noise sources in the thesis, is addressed here.

Light leakage from the optical modulation

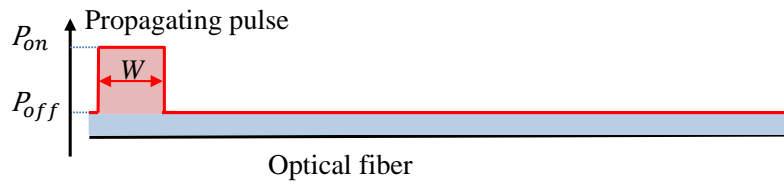


Figure 3.16 – Effect of the extinction ratio on the pulse modulation

As shown in Fig. 3.16, the continuous wave (CW) light leakage from the modulator can lead to a high power of integrated background light between pulses and results in Rayleigh backscattered noise, decreasing the SNR and sensing accuracy. The noise from this light leakage can not be suppressed using an optical filter, since the optical frequency of this noise contribution is the same as that of the signal, therefore it needs to be carefully reduced in the system at its origin.

This leakage results from a finite extinction ratio (ER), which is defined as:

$$ER = \frac{P_{on}}{P_{off}} \quad (3.55)$$

where P_{on} and P_{off} are the optical power when the modulation of the optical light is on and off, respectively. Ideally, P_{off} is zero, which means no light can pass the modulator when it is off, which allowing an infinitely large ER; however, typical modulators such as EOM and AOM (acoustic-optical modulator) show a finite ER, resulting from a continuous light leakage through the modulator. To address the effect of the finite ER on the SNR of a system, a pulse with duration W and a sensing fiber with length L are considered, as shown in Fig. 3.16. Actually, under the assumption that $P_{off} = 0$, the power of the Rayleigh backscattered light at the PD at a position z is given by Eq. 2.33 and can be rewritten as:

$$P_s = \frac{1}{2} F \alpha_r v_g W P_{on} e^{-2\alpha z}, \quad (3.56)$$

However, if P_{off} is not zero, the power received by PD is increased by the CW leakage induced Rayleigh backscattered light [102] as:

$$P_{\text{cw}} = F\alpha_r \int_0^L P_{\text{off}} e^{-2\alpha z} dz = \frac{F\alpha_r P_{\text{off}} (1 - e^{-2\alpha L})}{2\alpha}. \quad (3.57)$$

The noise in the detector will result from the beating between the Rayleigh-backscattered light from the optical pulse and that from the CW leakage. So the SNR limited by the ER can be approximated as

$$\begin{aligned} \text{SNR} &= \frac{P_s}{2\sqrt{P_s P_{\text{cw}}}} \\ &= \frac{1}{2} \sqrt{\text{ER}} \sqrt{\frac{\nu_g W e^{-2\alpha z}}{1 - e^{-2\alpha L}}} \end{aligned} \quad (3.58)$$

Here the self-beating of the Rayleigh scattering purely due to the CW leakage is ignored. As a rough estimation, we assume a short fiber, so that the loss is negligible and we then find

$$\text{SNR} = \frac{1}{2} \sqrt{\text{ER}} \sqrt{\frac{\nu_g W}{L}}, \quad (3.59)$$

from which we can see that sensing with high spatial resolution over a long distance requires a high ER for the modulation. For instance, a spatial resolution of 1 m (10 ns pulse width) for 10 km sensing distance, the ER has to be larger than 43 dB to result in a SNR larger than 1.

In the following chapters, two cascaded EOMs are used to secure a high enough ER, and in Chapter 6, to fulfill the requirement of high spatial resolution and zero frequency switch latency for the interrogating pulse, we use an RF (radio frequency) pulsing scheme [105] reaching extreme values for the ER, which will be addressed in more details later.

Phase noise of the light source

As ϕ -OTDR can be regarded as an interferometer, phase noise will be naturally a concern for the measurement results. The impact of phase noise in distinct interrogating schemes is different. For the sake of the simplicity of the demonstration, we mainly deal with the coherent length, which is a measure of the phase noise ^{III}.

For any interferometer, the coherent length should be larger than the optical path difference between the two arms of the interferometer. For a frequency-scanned ϕ -OTDR, as well as a pulse-engineered ϕ -OTDR, the requirement on the light coherent length is quite loose. From Eq. 3.7 and Eq 3.25, we can see that, the detected light comes from scatters within the pulse width. Therefore, the coherent length only needs to be larger than the fiber segment covered by a pulse width. However, for the coherent-detection based ϕ -OTDR, the coherent length

^{III} Another measure of phase noise is the linewidth δF of the laser, and the coherent length is $c\delta F$

should be in contrast larger than twice the fiber length, since the maximum optical path difference between the local oscillator and the signal corresponds to the round trip along the entire sensing fiber (Eq. 3.22). Hence, it sets a much stricter requirement on the linewidth of the laser. As far as an interferometric phase demodulation scheme is concerned, the coherent length must be larger than the length difference between the two interferometer arms, as shown in Eq. 3.22.

3.4 Conclusions

In this chapter, fundamental notions on ϕ -OTDR have been briefly introduced. This includes the technique working principle as well as various phase demodulation strategies. Emphasis has been put on frequency-scanned ϕ -OTDR as it allows quantitative measurements, requires the least hardware modification compared with conventional intensity-demodulated ϕ -OTDR without sacrificing the spatial resolution and bandwidth of the system, at the expense of added measurement time. Frequency-scanned ϕ -OTDR is thus suitable for static measurement (such as temperature sensing and hydrostatic pressure sensing) where high spatial resolution is needed. In chapter 5-7, different sensing applications will be investigated and demonstrated, which shows the potential of frequency-scanned ϕ -OTDR in diverse industrial areas.

4 Large errors on frequency estimation

As mentioned in the previous chapters, the quantitative measurement of ϕ -OTDR relies on the frequency shift (FS) estimation in the Rayleigh backscattering spectra, which is also used in optical frequency domain reflectometry (OFDR) for the quantification of the measurand [106]. In both systems, the problem of the large errors on the FS estimation emerged as outlier peaks or multi-peaks may appear in the correlated spectra when the cross correlation (CC) algorithm is used for the FS estimation [107, 108, 109]. This reduces the reliability of the system and limits the measurable temperature/strain range. In this chapter, the measurement errors are addressed and evaluated when using CC as the FS estimation algorithm.

In fact, CC is a common method that has been extensively studied for shift/time delay estimation in several applications, such as sonar and radar. The method for frequency shift estimation in ϕ -OTDR is mathematically equivalent to the time delay estimation problem, which means that we can use a similar approach to model it. Later on, experiments have been performed to verify the theory and a least mean square (LMS) algorithm has been proposed in frequency-scanned ϕ -OTDR to reduce the large errors. Finally, temperature sensing with high spatial resolution and large temperature dynamic range has been demonstrated experimentally based on frequency-scanned ϕ -OTDR with LMS .

The content of this chapter has been published in [34]¹, and this is a collaborative work with University of Alcala.

4.1 Frequency shift estimation using cross correlation

The conventional measurement technique in frequency-scanned ϕ -OTDR requires acquiring Rayleigh intensity traces as a function of the input laser frequency within a given frequency range. The refractive index distribution is fixed along the fiber once for ever after solidification,

¹© 2019 IEEE. Reprinted, with permission from L. Zhang, L. D. Costa, Z. Yang, M. A. Soto, M. Gonzalez-Herráez and L. Thévenaz, Analysis and Reduction of Large Errors in Rayleigh-Based Distributed Sensor, Journal of Lightwave Technology, Sept./2019, doi: 10.1109/JLT.2019.2917746.

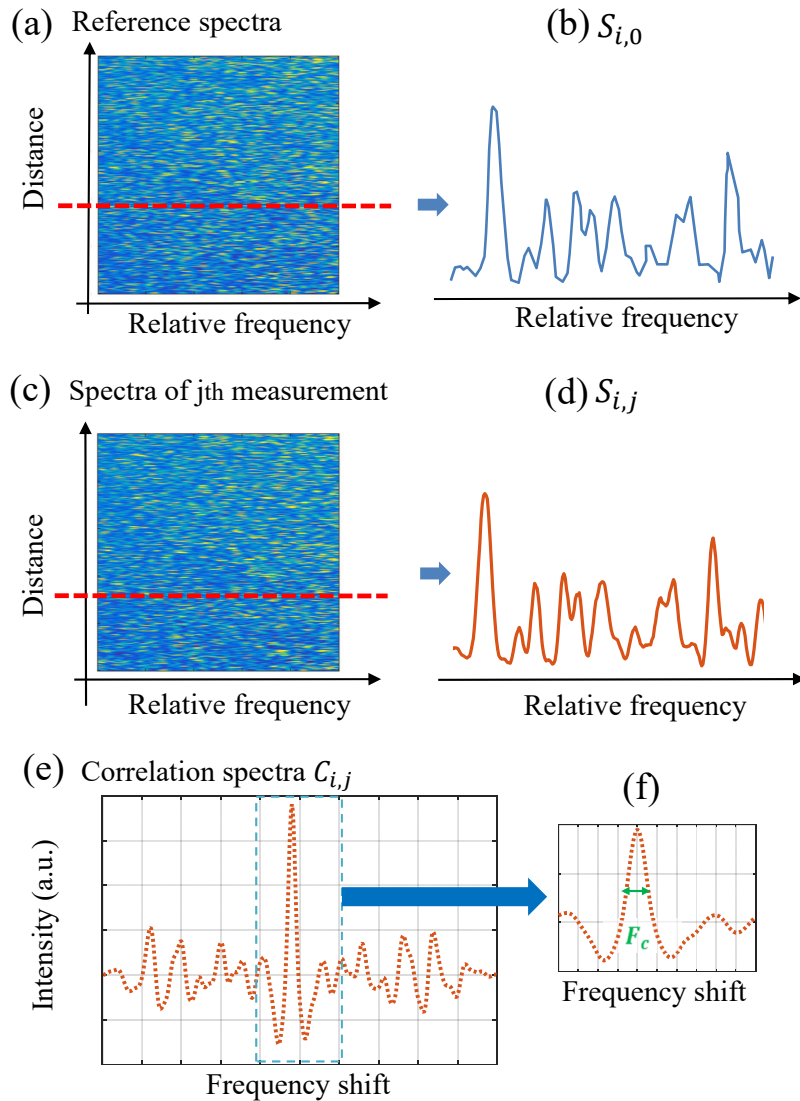


Figure 4.1 – Frequency estimation using cross correlation for frequency-scanned ϕ -OTDR: (a) 2-D intensity map of the reference and (b) spectrum at the i_{th} position point in the reference measurement; (c) 2-D intensity map of the j_{th} measurement; (d) spectrum at the i_{th} position point of the j_{th} measurement; (e) local correlation spectrum at the i_{th} position point; (f) close-up view of the correlation peak.

so that at a given position the intensity observed as a function of frequency will not change and can be regarded as a reference spectrum before the fiber is subjected to any strain or temperature change. In this case, a spectral shift of this local intensity versus frequency distribution is caused by the induced refractive index variation. Cross correlating the new measured local spectral response with the reference spectrum will result in a correlation peak placed at a frequency shift proportional to the local temperature and strain variations. The

proportionality is directly function of the thermo-optic and elasto-optic responses of silica and is strictly equal to the coefficients scaling the spectral response of fiber Bragg as mentioned earlier.

Let assume that the spectral response measured at the i_{th} sampling point along the position axis of the fiber is $S_{i,0}$ for the reference, and $S_{i,j}$ for a subsequent measurement at the same sampling point, as shown in Fig. 4.1 (b) and (d). The procedure to obtain the cross correlation spectrum is then:

$$C_{i,j}(\delta f) = \frac{1}{F_t} \int_0^{F_t} S_{i,j}(f) S_{i,0}(f - \delta f) df, \quad -F_t \leq \delta f \leq F_t \quad (4.1)$$

where F_t is the total frequency scanning range over the spectrum. The estimated FS $\widehat{\delta f}$ is located at

$$\widehat{\delta f}_{i,j} = \operatorname{argmax}_{-F_t \leq \delta f \leq F_t} C_{i,j}(\delta f) \quad (4.2)$$

representing the spectral location of the highest peak of the correlation spectrum (Fig. 4.1 (e) and (f)). In presence of noise, the accuracy of the method is directly related to the width of the correlation peak (F_c), which is in turn function of the shape and width of the interrogating pulse. For example, for a transform-limited square pulse with a width W , F_c is $1/W$. Incidentally, it means that a sharper spatial resolution (smaller W) decreases proportionally the accuracy on the measurement. The width F_c of the correlation peak will be used later in the definition of the large errors.

4.2 Large errors analysis

Despite of the small errors in the estimation, which causes uncertainties and defines the accuracy of the system, there is another type of errors observed in the frequency shift estimations, where the error is larger than the half width at the half-maximum of the correlation peak. The estimation error can be reasonably defined as

$$\epsilon_{i,j} = \left| \widehat{\delta f}_{i,j} - \delta f_{true,i,j} \right|, \quad (4.3)$$

and the large error $\epsilon_{i,j}$ is when

$$\epsilon_{i,j} \geq \frac{1}{2} F_c \quad (4.4)$$

Obviously, poor values of signal-to-noise ratio (SNR) or insufficient sampling rate may lead to errors of this type. However, later we will show that these large errors occur even for perfect SNR and sufficient oversampling of the frequency spectrum, for pure statistical reasons. Here we restrict our study to the error originating from the shift estimation method itself (cross

correlation), while the impact of other parameters (such as SNR and sampling rate) are out of the scope. Hence, all over our theoretical derivation, we will always assume that the SNR is sufficiently high, and we will ensure this high SNR in the experiments by performing a large number of trace averaging.

4.2.1 An example of large errors

An example of the occurrence of large errors in the estimation of frequency shift by cross correlation (CC) is illustrated in Fig. 4.2. A total frequency range F_t of 50 GHz for the reference is scanned. We deliberately change the temperature of the fiber, so that δf_{true} should be around -2 GHz in the measurement spectra (i.e. $\delta f_{true} \approx 2$ GHz). Fig. 2 (a) and (b) show, respectively, the reference and measurement spectra at the 2047_{th} sampling point along the fiber. We can see that most part of the reference spectrum is preserved in the measurement spectrum (see shaded spectral section with a frequency range of F in Fig. 4.2 (a) and (b) respectively). Fig. 4.2 (c) shows the cross correlated spectra between the reference and measurement at two positions along the fiber (points 2000_{th} and 2047_{th}). Although only a small shift of around -2 GHz is introduced in the measurement spectrum, the peak position in the correlation spectrum at position 2047_{th} is not located at the right position, unlike the 2000_{th} sampling point (see Fig. 4.2(c)). Thus, upon the FS profile shown in Fig. 4.2(d), a huge spike at the 2047_{th} sampling point can be observed, representing a large estimation error (much larger than $\frac{1}{2}F_c$).

From Fig. 4.2 (c) it can be also observed that, at the 2047_{th} point where the large error takes place, the spectral location of this misleading peak matches the frequency difference between the highest peaks in both the reference and measurement spectra, respectively. This can be explained by the fact that the CC spectra corresponds to the windowed convolution of the reference and measurement spectra (i.e. the integral of multiplied vectors, as a function of the relative shift). Hence, the spectral data with higher intensity contributes much more to the correlation magnitude. In other words, the CC process gives more weight to the high-intensity points and almost no weight to the low-intensity ones. From the point of view of shift estimation, however, all points carry the same amount of information. In the case of Rayleigh spectra, the probability density function (PDF) of the scattered intensity obeys a negative exponential distribution [72], which means that most of the points in the spectra are low-intensity points. Whenever a high intensity point appears in the finite analyzed spectral window, the peak cross correlation value may be biased towards this new position, giving rise to large errors.

However, this feature is not restricted to exponential distributions. Any data statistical distribution would lead to a similar failing. The key issue is the finite analyzed spectral window. As observed in Fig. 4.2 (a) and (b), the measurement spectrum at a given position can be divided into a correlated signal within a spectral range F and an uncorrelated spectral section appearing in the measurement due to an induced temperature or strain change (within a spectral range F_0). Thus the total measured spectral range can be described as $F_t = F_0 + F$. Only

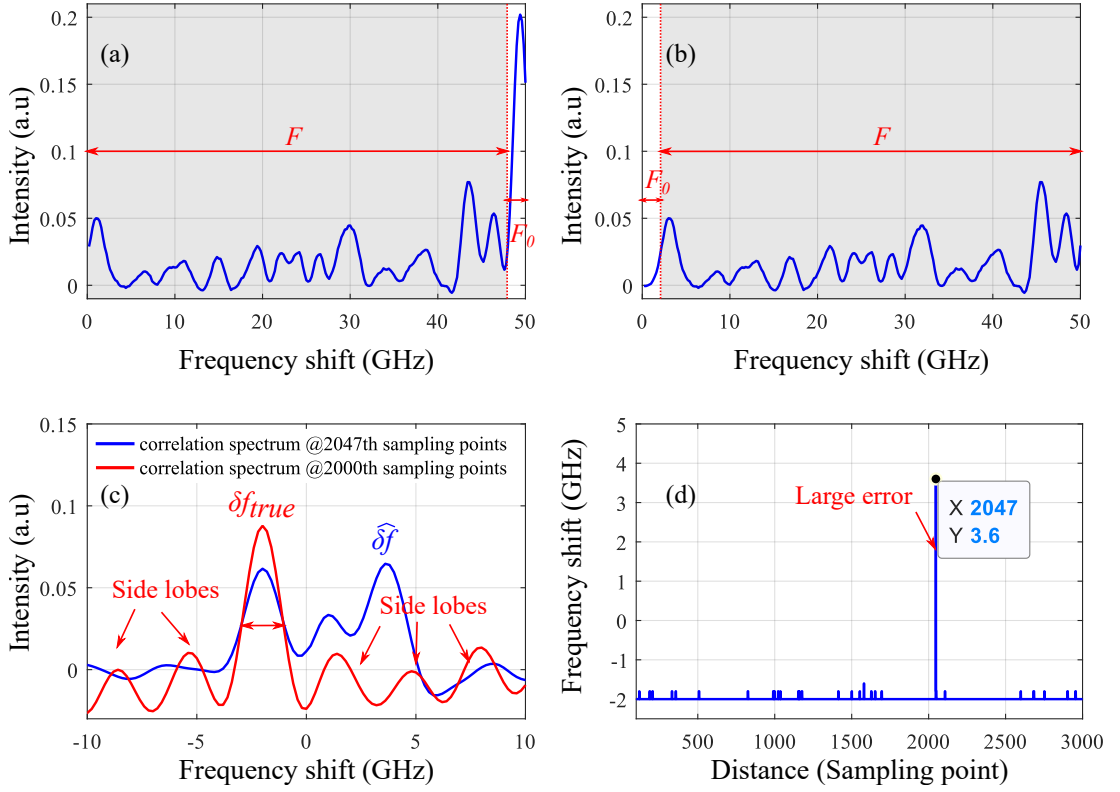


Figure 4.2 – An example of the occurrence of large errors: (a) the reference spectrum and (b) the measurement spectra at the position of the 2047th sampling point (c) correlation spectra at the 2047th sampling point (with error) and the 2000th sampling point (without large error). (d) Estimated FS profile obtained by cross correlation showing the occurrence of a large error.

the correlated spectral section will contribute to the FS estimation through cross correlation while the uncorrelated spectra will essentially give irrelevant contributions. If the spectral response in this region is high enough, this uncorrelated area may induce a spurious peak higher than the true correlation peak. This is the essence of the large errors when using CC as shift estimation method.

4.2.2 Analytical model for Large errors analysis

The appearance of large errors imposed by CC for stochastic signals has already been observed and modeled in time delay estimation [110, 111, 112]. The method for FS estimation in ϕ -OTDR and OFDR is mathematically equivalent to the time delay estimation problem, which means that we can use a similar approach to model it. By adapting the model from time delay estimation literature [111], the probability of large errors (PLE) in ϕ -OTDR can be written as:

$$PLE = (M - 1) \sqrt{\frac{1}{2\pi C}} \exp\left(-\frac{C^2}{2}\right) \tag{4.5}$$

where

$$C = \sqrt{B_s F} \frac{\text{SNR}}{[(\text{SNR})^2 + 2(\text{SNR} + 1)^2]^{1/2}} \quad (4.6)$$

and

$$M = 2F_0 / F_c. \quad (4.7)$$

M is a unitless coefficient scaling the relative importance of the uncorrelated spectral range F_0 with respect to the width of the correlation peak F_c . B_s is the statistical bandwidth which is defined as:

$$B_s = \left[\int_{-\infty}^{\infty} \rho^2(f) df \right]^{-1} \quad (4.8)$$

wheres $\rho(f)$ the normalized correlation function of the signals [110]. For example, for a square pulse of width W and considering an exponential delay distribution, the calculated $B_s \approx 1.38W$. Note that the SNR in the above expressions is the ratio between the variance of the spectrum and the variance of the noise across the full measured spectral window, hence the impact of fading signals is averaged out. Under the assumption of $\text{SNR} \gg 1$ we have:

$$\frac{\text{SNR}}{[(\text{SNR})^2 + 2(\text{SNR} + 1)^2]^{1/2}} \approx \frac{1}{\sqrt{3}}. \quad (4.9)$$

Therefore, the expression of PLE can be simplified as

$$PLE = \frac{\sqrt{\frac{3}{2\pi}} (2F_0 / F_c - 1) \exp(-\frac{B_s F}{6})}{\sqrt{B_s F}}. \quad (4.10)$$

For a square pulse, $F_c = 1/W$ and $B_s = 1.38W$, so that Eq. 4.10 can be rewritten as

$$PLE = \frac{\sqrt{\frac{3}{2\pi}} (2F_0 W - 1) \exp(-\frac{1.38WF}{6})}{\sqrt{1.38WF}}. \quad (4.11)$$

From Eq.4.11, it is possible to observe that: with a certain pulse width W , the PLE is linearly related to F_0 when $F_0 W \gg 1$, while the frequency range F decreases the PLE exponentially. Intuitively speaking, the spectra in the range of F for reference and measurement are correlated and therefore contribute to the same peak in the correlation spectrum. Consequently, this peak, placed at δf_{true} , grows exponentially with the increase of F , leading to an exponential reduction of the PLE . On the other hand, any perturbation applied on the fiber (such as temperature or strain change) leads to a loss of correlation in the data points, which are replaced by uncorrelated data over a range F_0 . This feature contributes to the occurrence of random side lobes in the cross correlation spectrum, showing an increasing probability to turn higher than the true correlation peak. As a result, the increase of F_0 increases the PLE linearly ($F_0 W \gg 1$).

4.2.3 Comparison of the theoretical and experimental *PLE*

To investigate the impact of the measurement parameters, such as the pulse width, the scanned frequency range and the scanning frequency step on the *PLE*, a direct-detection based ϕ -OTDR is implemented to obtain the experimental spectra along a sensing fiber.

The experimental setup is depicted in Fig. 4.3. A distributed feedback (DFB) laser with 1 MHz linewidth is used as a coherent light source. Two electro-optical modulators (EOM) are cascaded to shape the continuous-wave light into optical pulses having a width of 0.5-1 ns with high extinction ratio, thereby allowing a spatial resolution of 5-10 cm. An erbium-doped fiber amplifier (EDFA) is then inserted to boost the pulse peak power, though at a level below the onset of nonlinear optical effects in the sensing fiber. The coherent pulse is launched into the sensing fiber and the back-captured Rayleigh scattering is then pre-amplified using another EDFA before photo-detection. The amplified spontaneous emission (ASE) noise introduced by this EDFA is filtered out by an optical filter with a bandwidth of 1 nm. The bandwidth of the PD is 3 GHz. An oscilloscope operating at a sampling rate of 5/10 Gs/s is used to digitize the electrical signal for further analysis. The sensing fiber here is a single-mode fiber with a length of about 860 m, from which 5 m are immersed into a water bath to apply temperature changes (see later Section 5). The sweep of the optical frequency is performed by directly modulating the temperature or current of the laser using a remote controlled laser power supply. The frequency step Δf is set to be 100 MHz and 200 MHz when using 1 ns pulse and 500 ps pulse, respectively, in order to adapt to the broadening of the pulse spectrum. To secure a high enough *SNR*, each retrieved trace is averaged 4000 times.

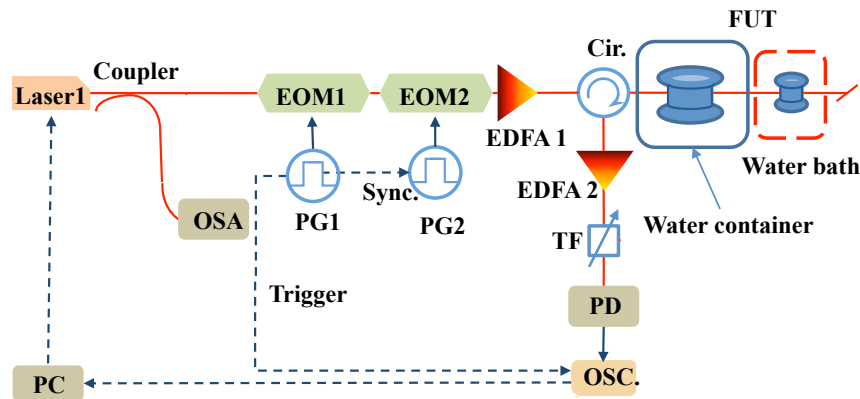


Figure 4.3 – Experimental setup of frequency-scanned ϕ -OTDR (EOM: electro-optical modulator, EDFA: erbium-doped fiber amplifier, Cir: circulator, FUT: fiber under test, TF: tunable filter, PD: photodetector, OSC: oscilloscope, PC: personal computer, PG: pulse generator, Sync, synchronization).

Using this scheme, the coherent Rayleigh spectrum of the entire fiber is measured with a spatial resolution of 5 cm and 10 cm, over a frequency scanning range of 100 GHz. To obtain the experimental *PLE* for different scanning ranges F_t , the following procedure was applied:

- 1 Obtain the Rayleigh spectrum of the fiber over a range of 100 GHz: $X_{i,j}(f)$, $f \in [0, 100 \text{ GHz}]$. Here, i denotes the position along the fiber and j denotes the measurement sequence;
- 2 Choose ‘reference’ and ‘measurement’ data from $X_{i,j}(f)$. For a certain scanning range F_t and frequency shift F_0 , let the reference spectrum be $S_{i,0}(f) = X_{i,0}(f)$, $f \in [0, F_t]$ and the measurement spectrum be $S_{i,j}(f) = X_{i,0}(f)$, $f \in [F_0, F_0 + F_t]$. Therefore, the spectrum of the reference $S_{i,0}$ and the measurement $S_{i,j}(f)$ are subsets from the same data set, will span over a total range F_t and the true FS is $\delta f_{true} = F_0$. Since both $S_{i,0}(f)$ and $S_{i,j}(f)$ are taken from $X_{i,0}(f)$, the two spectra can be considered to have perfect SNR (effectively there is no variance between the two correlated spectra);
- 3 Cross correlate $S_{i,0}(f)$ and $S_{i,j}(f)$ to get the correlation spectrum $C_{i,j}(\delta f)$ and obtain the estimation using Eq. 4.1 and Eq. 4.2;
- 4 Determine if $\epsilon_{i,j}$ is a large error by determining if $\epsilon_{i,j} = |\delta f_{i,j} - \delta f_{i,true}| \leq \frac{1}{2} F_c$;
- 5 Repeat steps a-d for each sampled position to get the total number of large errors. *PLE* is estimated as the ratio between the number of large errors and the total number of sampled positions.

The experimental results are obtained through the aforementioned process, and the theoretical results are calculated by Eq. 4.11 by replacing F with $F_t - F_0$. An exponentially decaying tendency of the *PLE* as a function of the frequency scanning range F_t is shown in Fig. 4.4(a) and (b), as predicted. Fig. 4.4 (c) shows a comparison of the *PLE* (in log scale) obtained with two different pulse widths. It can be seen clearly that, with the same frequency scanning range F_t , the *PLEs* of the longer pulse decrease faster than that of the shorter pulse, demonstrating that the implementation of a robust Rayleigh sensor with high spatial resolution becomes extremely challenging due to the increased probability of large errors. Fig. 4.4 (d) shows a quasi-linear relation between the FS and the *PLE*. Similarly, the *PLE* grows faster with the increase of the frequency shift F_0 using a shorter pulse, which means the measurable temperature and strain change must be kept smaller in high spatial resolution scheme. It must be noted that similar *PLEs* will be obtained at high spatial resolution by simply rescaling proportionally the frequency scanning range, since eventually this is the width of the correlation peak normalized to the frequency scanning range that scales the *PLE*.

In all these cases, the experimental results show a good agreement with the theoretical results, validating the model proposed in the previous section. This means that the *PLE* can be reliably predicted using Eq. 4.11 when all the measurement parameters are known. For instance, Fig. 4.4 (c) shows that $PLE=10^{-3}$ when the spectral scanning range is 50 GHz and the pulse width is 500 ps. This means that, in principle, in a 50 m-long sensor with 5 cm spatial resolution (i.e. having only 1,000 sensing points) and high enough SNR, there will be statistically one large error for each measurement. If the scanning range increases up to

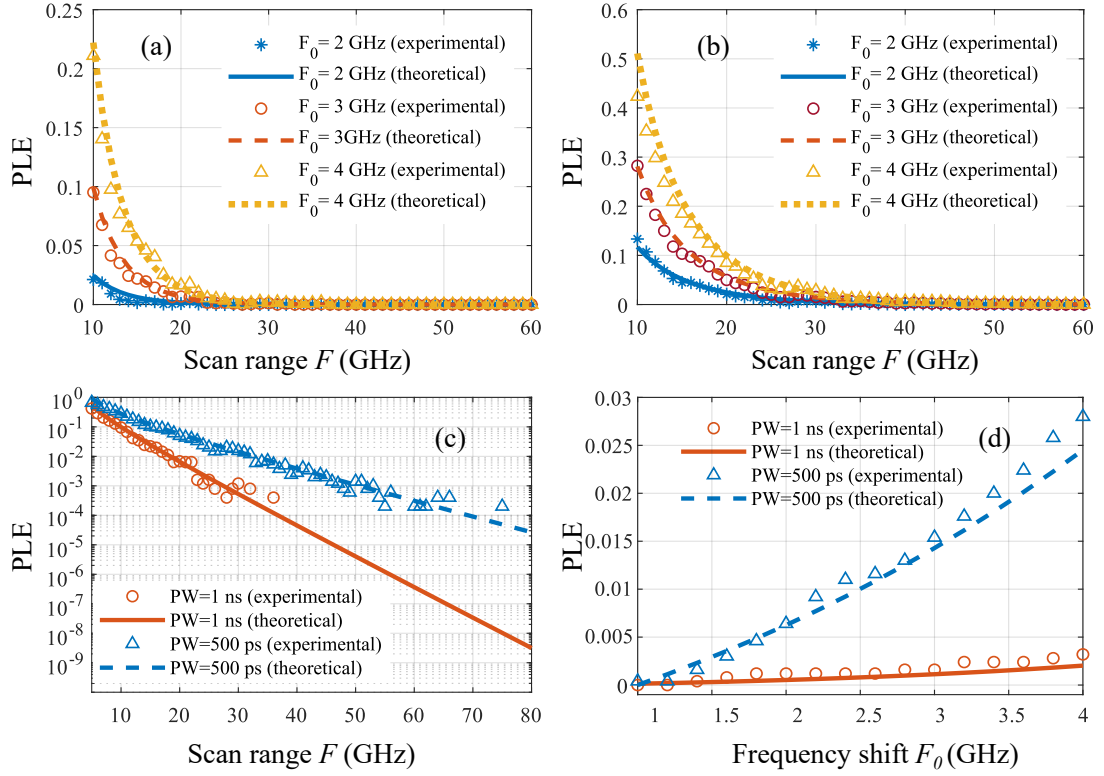


Figure 4.4 – Comparisons between experimental and theoretical results. The probability of large error v.s. scan range F_t with a pulse width of (a) 1 ns and (b) 500 ps, F_0 is the frequency offset between measurement and reference spectra; (c) comparative PLE using different pulse widths ($F_0=3$ GHz) (d) PLE dependence on FS ($F_t=30$ GHz) (PW: pulse width)

70 GHz, the PLE reduces to 10^{-4} , which is statistically still not low enough to allow reliable measurements if the number of sensing points is large.

It may be argued that the above mentioned large error problem can be alleviated by extending the frequency scanning range of the reference only, while keeping the measurement spectrum bounded to the same value. Let the scanning ranges of reference and measurement be F_t and F_s , respectively, F_t being larger than F_s , as shown in Fig. 4.5. In this case, the range relevant for correlating the signals can be kept as F (i.e. $F=F_s$) even through there is a shift δf_{true} in the measurement spectrum, as long as $\delta f_{true} \leq F_d$, where $F_d = \frac{1}{2}(F_t - F_s)$. However, since the ranges of the reference and measurement are different in this case, there will always exist some spectral samples in the reference that are not contained in the measurement set (thus being uncorrelated) even when there is no temperature or stain change to the fiber. These samples are expected to contribute to the generation of random spurious peaks, increasing the PLE . The FS estimation in this case is made using the equations as below:

$$C_{i,j}(\delta f) = \frac{1}{F_s} \int_0^{F_s} S_{i,j}(f) S_{i,0}(f - \delta f) df, \quad -F_d \leq \delta f \leq F_d \quad (4.12)$$

$$\widehat{\delta f_{i,j}} = \underset{-F_d \leq \delta f \leq F_d}{\operatorname{argmax}} C_{i,j}(\delta f) \quad (4.13)$$

The experimental results are calculated following the same procedure as before, but in step 2, the data used for cross correlation have been changed into:

- 2 For a certain measurement scan range F_s and range difference F_0 , Let $S_{i,0}(f) = X_{i,0}(f)$, $f \in [0, F_0 + F_s]$ and $S_{i,j}(f) = X_{i,0}(f)$, $f \in [0, F_s]$;

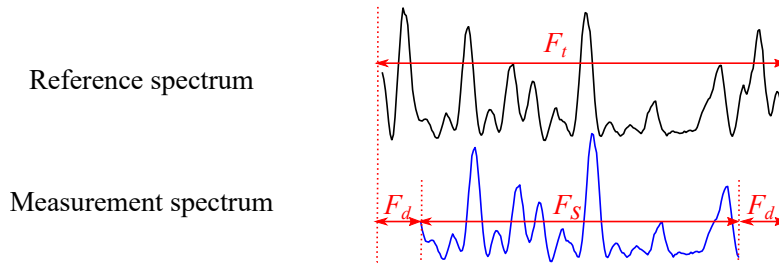


Figure 4.5 – Diagram to show the different scan ranges of reference and measurement.

In this case, the correlated spectral range F equals to the measurement scanning range F_s , while the uncorrelated spectral range F_0 equals to $2F_d$. The results of the calculated *PLE* through experimental data and the presented analysis method are shown in Fig. 4.6. An exponential decay tendency of *PLEs* versus the increase of F_s is again visible, indicating that the *PLE* grows as the range difference F_0 between measurement and reference increases. It suggests that the larger the difference between the reference scan range F_t and the measurement scan range F_s , the larger the *PLE*, due to the presence of a larger number of uncorrelated points.

In short, as long as there are different samples entering the spectral scanning windows of measurement and reference, the *PLE* remains larger than 0, no matter if the new sampled points are due to temperature or strain-induced frequency shift or simply due to differences in the reference and measurement scanning ranges. In principle, only when both reference and measurement scanning ranges are the same and temperature or strain do not change, the *PLE* reaches zero (under the assumption of no statistical noise). This condition is of course in total contradiction with the purpose of a sensing system.

It must be noted that, all calculations are based on the same measurement, which has been obtained under a very high SNR condition. In normal conditions, under the presence of significantly higher noise levels, the level of correlation between common spectral sections will be reduced, thus increasing the *PLE*.

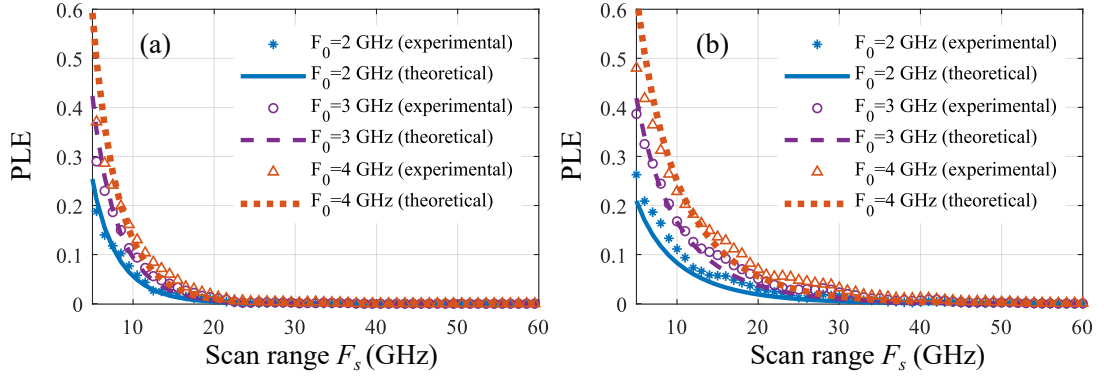


Figure 4.6 – *PLE* vs. spectral scanning range of measurement F_s with a pulse width of (a) 1 ns and (b) 500 ps when the scanning ranges of the reference and measurement are different. F_0 is the frequency range difference between the measurement and reference spectra i.e. $F_0 = 2F_d$.

4.3 Least mean square for reducing the large errors

4.3.1 *PLE* of least mean square algorithm

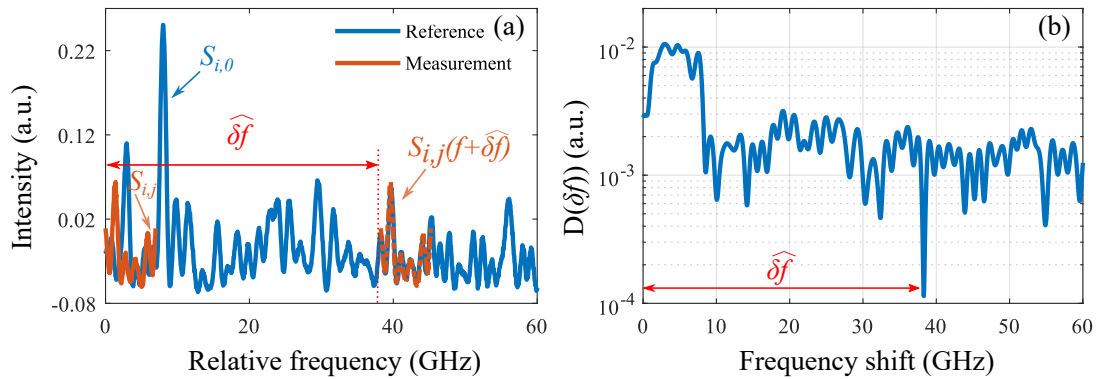


Figure 4.7 – Principle of the frequency shift estimation using the proposed least mean squares (LMS) method. (a) The measurement spectrum at a given point (orange) is swept over the broad reference spectrum (blue) and LMS are calculated for each relative spectral position δf . (b) Mean square errors as a function of the frequency shift δf showing a clear minimum value which is the estimation of the best similarity.

As discussed in the previous section, the *PLE* using cross correlation is often not negligible to secure confident sensing conditions. The question arises if another method is more effective to reliably estimate the frequency shift. Here, an approach based on least mean squares (LMS) is proposed for retrieving the frequency shift in Rayleigh sensing, by evaluating the degree of similarity between particular sections of the spectra and estimating the offset between them. Assuming that the scanning ranges of reference and measurement are F_t and F_s respectively,

the mean square error between reference and measurement is defined as

$$D_{i,j}(\delta f) = \frac{1}{F} \int_0^F (S_{i,j}(f) - S_{i,0}(f - \delta f))^2 df, \quad -F_d \leq \delta f \leq F_d \quad (4.14)$$

and the FS estimation is

$$\widehat{\delta f_{i,j}} = \arg \min_{-F_d \leq \delta f \leq F_d} D_{i,j}(\delta f) \quad (4.15)$$

LMS measure the amplitude difference between two spectral regions, so that the estimated frequency shift is the one associated to the minimum LMS. This way the weight of each spectral points is identical – even the most frequently occurring spectral points of low amplitude equally contribute to the estimation – thereby the seldom-occurring high-amplitude points would not lead to large error. In reality, the minimum value will not be zero due to the presence of noise; however, the minimum LMS will be located only at the frequency shift corresponding to the true spectral shift, as illustrated in Fig. 4.7.

Fig. 4.8 compares the *PLE* obtained when using cross correlation and the proposed LMS method using the same datasets. In Fig. 4.8 (a), *PLE* is calculated with infinitely high SNR (when $S_{i,j}$ and $S_{i,0}$ are obtained from the same dataset $X_{i,0}(f)$, using different scanning ranges for the reference and measurement). It can be seen that, with no statistical variations (noise), the *PLE* is always zero using LMS even if the scanning range of the measurement F_s is only 2 GHz. In Fig. 4.8 (b), the $S_{i,j}$ and $S_{i,0}$ used for calculation are taken from different datasets ($S_{i,0}$ is taken from $X_{i,0}(f)$, and $S_{i,j}$ from $X_{i,j}(f)$ ($j \geq 0$)), hence noise is present. The figure shows that, in presence of noise, the *PLE* is not always zero when using LMS, as expected, but still, it is significantly reduced by the LMS estimation compared to cross correlation. The results also clearly indicate that when the scanning range F_s reaches 8 GHz, the *PLE* becomes negligible in our experiment using LMS. In other words, only a scanning range of 8 GHz is required using the proposed method, significantly speeding the acquisition.

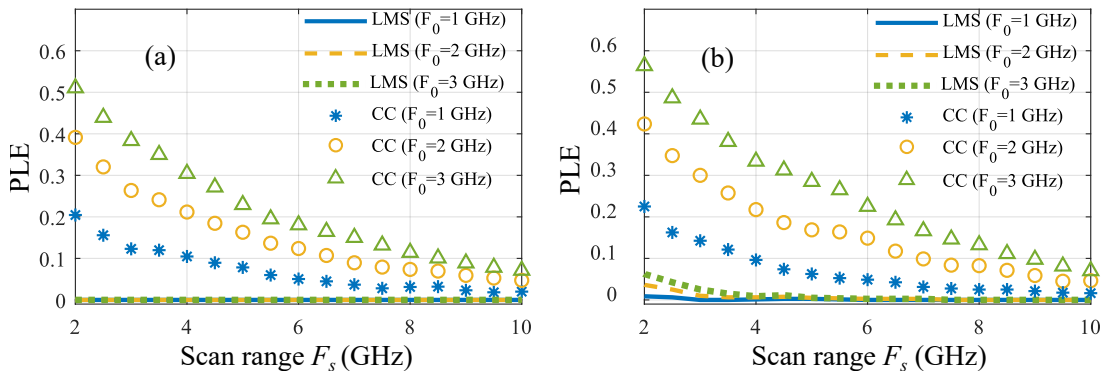


Figure 4.8 – Comparison of *PLE* between LMS and correlation with increasing scan range of measurement F_s (PW=1 ns), (a) with noise; (b) without noise.

To explain the mathematical difference between LMS and CC, we can open the brackets in Eq. 4.14, and rewrite it as:

$$D_{i,j}(\delta f) = \frac{1}{F} \left[\int_0^F S_{i,j}^2(f) df + \int_0^F S_{i,0}^2(f - \delta f) - 2 \int_0^F S_{i,j}(f) S_{i,0}(f - \delta f) df \right], -F_d \leq \delta f \leq F_d \quad (4.16)$$

Comparing Eq. 4.16 with Eq. 4.12 shows that the minimum of $D_{i,j}(\delta f)$ will be co-located with the maximum of $C_{i,j}(\delta f)$, provided that the first two terms on the right hand of Eq. 4.16 are constant with respect to δf . This condition is fulfilled when the mean energy of the process does not depend on the size of the integration window, proving the theoretical convergence. Practically, this co-location can only be strictly true in absence of CC large errors, i.e. when the signal and reference windows are infinitely large as stated by Eq. 4.10 and Eq. 4.11.

4.3.2 Temperature sensing with high spatial resolution

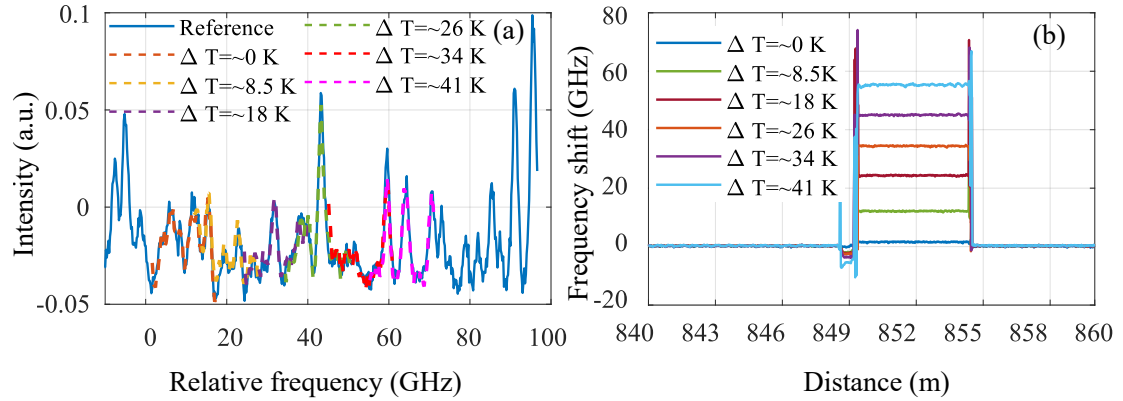


Figure 4.9 – Experimental results of temperature sensing using the proposed LMS-based ϕ -OTDR: (a) Spectra of the reference (blue line, obtained by tuning the temperature of the laser) and 6 measurements at different temperatures (at a fiber position of ~ 852 m, obtained by tuning the current of the laser); (b) Retrieved frequency shift profiles.

In order to validate the performance of the proposed LMS-based method, a temperature sensing experiment is set up by placing the last few meters of fiber into a temperature controlled water bath to create a hotspot. A 500 ps pulse is used, corresponding to a spatial resolution of 5 cm. The temperature sensing experiments are carried out with a 200 MHz frequency scanning step. A reference measurement over a ~ 140 GHz range is first acquired, which is realized by tuning the laser temperature. This lengthy acquisition is made once forever under controlled conditions (stable temperature). In contrast, the spectral scanning for the live measurements is realized by laser current tuning, so that the acquisition can be way faster (~ 15 s). The scanning range of the measurement spectrum is set to cover 16 GHz, which is much shorter than the reference spectrum. A $100\times$ averaging is performed at acquisition

before any data processing. The temperature at the hotspot is varied from 0 K to 41 K with respect to room temperature.

Fig. 4.9(a) shows the measured spectra for different temperatures at a particular sensing point (distance 852 m), along with the reference spectrum (solid blue curve). It clearly shows that the measurement spectra match well with the corresponding sections of the reference spectrum. These results also suggest that:

- 1 The maximum measurable temperature range is actually limited by the spectral range of the reference but not that of the measurement. Therefore, a large FS range can be attained by only extending the reference spectrum while maintaining the high sensitivity of the system and a fast acquisition for sequential measurements. This is in clear contrast with the CC estimation.
- 2 A measurement scanning range containing only few peaks (e.g. 2-3) in the spectral window is sufficient to estimate the frequency shift without large errors. This provides a crucial advantage in terms of measurement speed, since the number of scanning points for the measurement spectrum can be reduced. Besides, the measurement time is further reduced since the minimum scan range of the measurement is only a few tens of GHz (16 GHz in this experiment), the scan of the optical frequency is performed by tuning the current of the laser, which is practically faster settled than tuning the temperature of the laser.

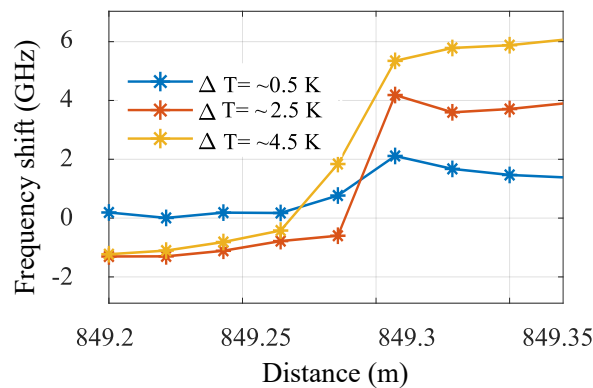


Figure 4.10 – frequency shift distributions around the edge of the hotspot which confirms a spatial resolution of less than 5 cm.

The profiles of the frequency shift along the end section of the fiber are shown in Fig. 4.9(b), estimated using LMS at different temperatures. In the hotspot (starting from 849.5 m), clear frequency shifts can be seen without large errors, being also in good agreement with the preset water temperature. A few glitches are present at fiber positions corresponding to transitions to and from the heated water bath, where the temperature is unstable and non-uniform over the interrogating spatial resolution.

A spatial resolution of less than 5 cm can be verified in Fig. 4.10, showing the frequency shift distributions around the front edge of a hot spot and confirming a transition in the measured profiles of 4.28 cm.

Lastly, the frequency shift repeatability is calculated to be 0.026 K, estimated by obtaining the standard deviations of each local estimated FS from 10 consecutive independent measurements, which shows a temperature dynamic range as large as 36.5 dB (an accuracy of about 1/5000 of the measurable temperature change).

4.4 Conclusions

The probability of large errors (*PLE*) occurring in ϕ -OTDR employing frequency shift estimation through cross correlation is addressed for the first time in this section. It turns out to be a critical limitation and *PLE* occurrences are essentially unpredictable. According to the proposed model, the *PLE* decreases exponentially with the frequency scanning range and grows linearly with the applied frequency shift (when $F_0W \gg 1$). The results of our analysis agree well with the experimental results. The analytical model clearly shows that large errors on the FS estimation of ϕ -OTDR unavoidably occur when using cross correlation techniques due to purely stochastic reasons related to the limited spectral window of analysis, even in conditions of perfect signal to noise ratio. Moreover, we have proposed a method to circumvent these large errors, employing a least mean squares estimation of the similarity between reference and measurement spectra. Using this method, the stochastic cause of large errors can be totally suppressed and becomes only limited by noise. The maximum temperature measurement range can be safely enlarged while keeping a limited spectral scan for running acquisitions. As a result, a frequency-scanned ϕ -OTDR system with a spatial resolution of 5 cm and sensing range of about 860 m is demonstrated, which has a dynamic range of temperature change of about 36.5 dB and very robustly immune to large statistical errors.

Finally, it should be noted that large errors do not only occur in correlation-based ϕ -OTDR. A similar model can be developed for any Rayleigh-based distributed sensor employing frequency shift estimation of the backscattered spectra based on cross correlation, such as coherent OFDR.

5 Distributed pressure sensing

Traditional distributed optical fiber sensors (DOFSs) using standard single mode fibers (SMFs) are mostly focused on temperature and axial strain sensing. Recently, it was shown that by properly designing the sensing fiber, different quantities (such as chemical, radiation and humidity) will induce temperature and/or strain variations in the fiber, therefore can be measured through these DOFSs [113, 114, 115]. In this chapter, distributed pressure sensing based on frequency-scanned ϕ -OTDR using special designed fibers is proposed and experimentally demonstrated.

Pressure sensing has important applications in domains such as structural health monitoring, security surveillance, oil, gas and other energy-related industry [1, 2, 3]; what is more, a mean to monitor the local pressure at multiple locations is subject to a high demand from today's complex industrial facilities and systems[116]. A few distributed pressure sensing (DPS) schemes have been proposed based on dynamic gratings[116, 117] or optical frequency-domain reflectometry (OFDR)[36], demonstrating the great potential of DPS using DOFS technology. However, either the pressure sensitivity is relatively low due to the large Young's modulus of the fiber material (silica)[116, 117], or the sensing range is fundamentally limited by the sensing range of OFDR [36]. Design of fiber cables are also studied to enhance the pressure sensitivity [118, 119].

Owing to the ultra high sensitivity of ϕ -OTDR, temperature sensing using single mode fiber with sharp spatial resolution (5 cm) [34] has been demonstrated in the previous chapter with almost 1 km range sensing distance based on a least mean square algorithm. Based on a similar scheme, a DPS system based on frequency-scanned ϕ -OTDR is proposed, by replacing the conventional SMF with either a photonic crystal fibers (PCFs) or an elliptical core fiber with side air holes (SAHF) in the cladding, and measuring the fiber changes in birefringence when pressure is applied.

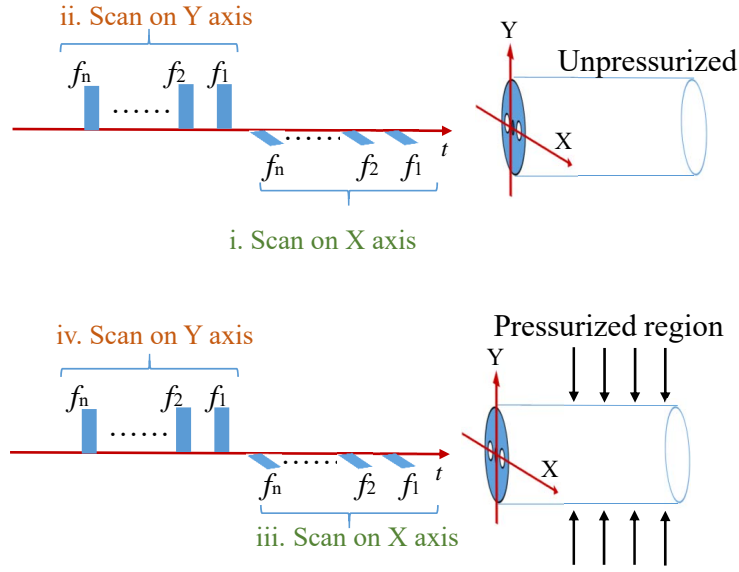


Figure 5.1 – Scanning procedure of the interrogating pulses for the reference and measurement.

5.1 Principle

The working principle of the proposed DPS is based on the distributed birefringence measurement of the fiber, which is similar to the scheme proposed in [120]. Instead of using non-birefringent SMF, the DPS fibers exhibit pressure-dependent birefringence. The polarization state of the interrogating pulses have to be aligned to both principal axes of the fiber, thus delivering the Rayleigh spectra (RS) corresponding to the two orthogonal principal polarization states. Owing to the anisotropic structure of the fiber cross section, the phase changes induced by external pressure on the two axes are different. The change in birefringence can be calculated as:

$$\Delta B(P, z) = \Delta n_x(P, z) - \Delta n_y(P, z) \quad (5.1)$$

In order to obtain the RS spectra for both linear principal polarization states axes and at all positions along the fibers, the optical frequency needs to be scanned along both axes (denoted X and Y) separately, as shown in Fig. 5.1. In the actual experiment, the scanning order is as below:

- i Take the reference traces by scanning on the fiber X-axis before any pressure is applied;
- ii Take the reference traces by scanning on the fiber Y-axis before any pressure is applied;
- iii Scanning on the fiber X-axis after pressure change is applied;
- iv Scanning on the fiber Y-axis after pressure change is applied.

- v Repeat step **iii** and step **iv** for repeating the measurement operation.

The pressure induced phase changes can then be compared by performing cross-correlation on each axis between their reference and measurement spectra (i-iii and ii-iv) using Eq. 5.1. To illustrate this, experimentally obtained spectra are shown in Fig. 5.2, respectively.

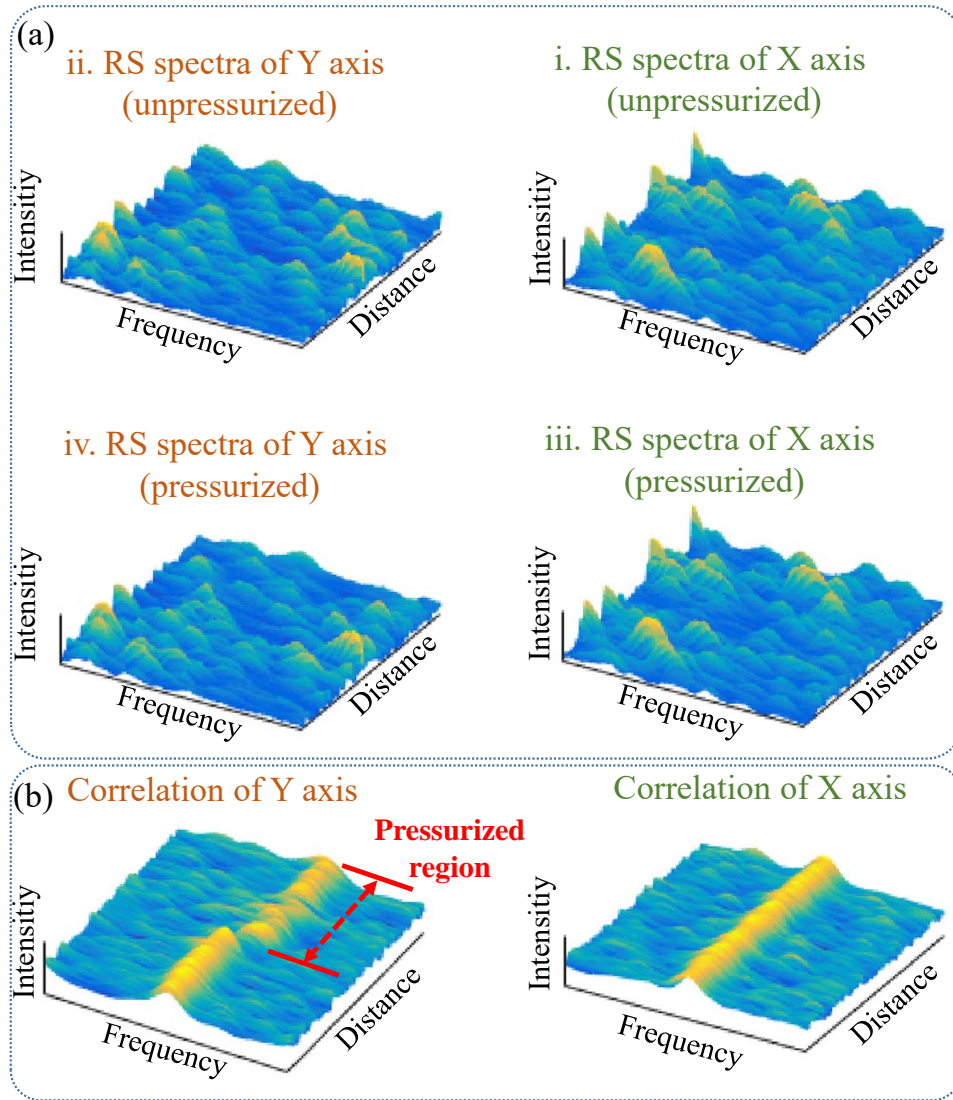


Figure 5.2 – Pressure sensing principle: (a) obtained Rayleigh scattering (RS) spectra; (b) correlation spectra between Y references and measurements on each polarization axis, respectively.

5.2 Experimental setup

The experimental setup is shown in Fig. 5.3, where the interrogator, while very similar to the one used in the previous chapter, is equipped with some polarization controlling components

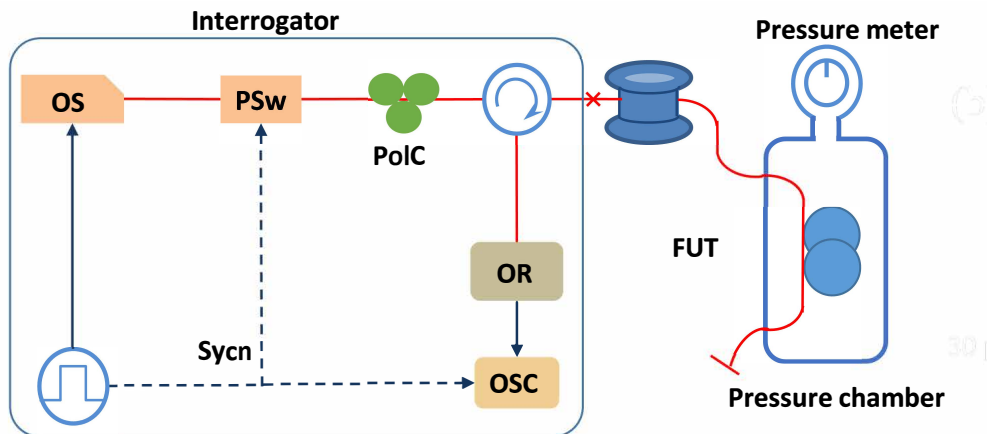


Figure 5.3 – Experimental setup. OS: optical source, PSw: polarization Switch, PoIC: polarization controller, FUT: fiber under test, OR: optical receiver, OSC: oscilloscope.

in order to align and switch the polarization states of the optical pulses. The light source consists of a distributed feedback laser (DFB) with a linewidth of 1 MHz, followed by an intensity modulator and an optical amplifier to shape optical pulses with high extinction ratio. The optical pulses are then sent into a polarization switch before passing through a polarization controller (PoIC), so that their polarization states can be aligned with each principal axis of the fiber under test (FUT), alternatively. The frequency shift (FS) induced by a temperature change δT or a pressure change δP can be evaluated separately along both axes through the cross correlation of their independent RS spectra. Fast and broad (50 GHz) frequency scans of the interrogating pulses are achieved by direct tuning of the laser current with a frequency scanning step of 80 MHz. About 5 m long fiber at the end is placed into a pressure chamber (hydro-static oil pipe) including an integrating pressure meter.

5.3 Distributed pressure sensing using "butterfly" PCFs

Photonic crystal fibers (PCFs) have received increasing attention for their potential application in non-linear optics, lasing, sensing, etc., since their advent in 1996 [121, 122, 123, 124, 125]. In PCFs, light is trapped by a periodic lattice with a wavelength-scale pitch made of microscopic holes in the cladding glass. Ultra-high birefringence (10^{-3}) PCFs have been proposed and demonstrated [126, 127], and an in-depth analysis of the influence of temperature and pressure on the propagation constants of these fibers [128, 129] show that the temperature sensitivity of highly birefringent PCFs (dB/dT) is at least one order of magnitude lower than that of conventional birefringent fibers (such as "bow-tie" [130] or "Panda" fibers [131]), due to the absence of thermal stress. Therefore, hydrostatic pressure sensing is a promising application for highly birefringent PCFs, in particular considering that they exhibit low cross-sensitivity with temperature .

In this section, distributed pressure sensing carried out using two high birefringent PCFs is

addressed¹.

5.3.1 "Butterfly" photonic crystal fibers

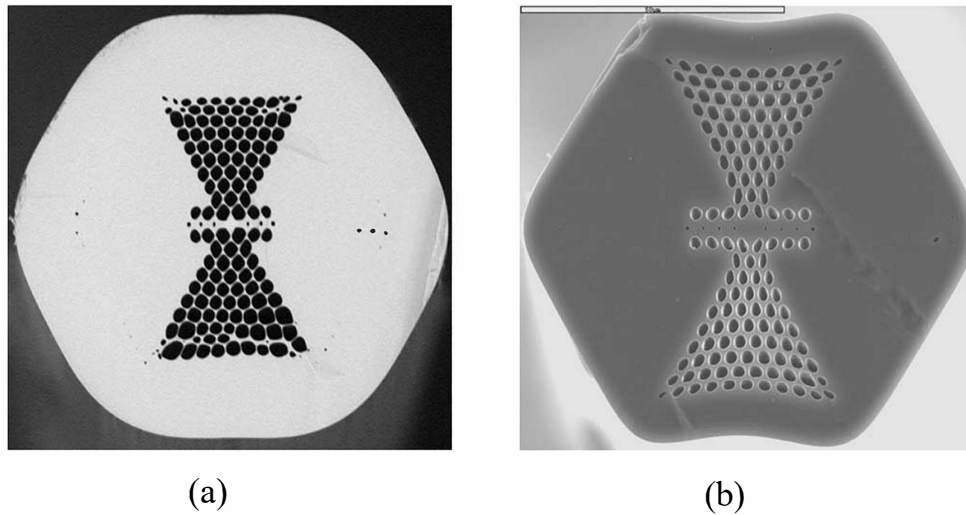


Figure 5.4 – Scanning electron microscope (SEM) images of the cross sections of the two PCFs under test: (a) fiber A; (b) fiber B

The pressure sensitivity dB/dP of PCFs mainly relies on the mechanical asymmetry of their microstructured region [129], which results in large differences in terms of the stress components generated in the fiber core. Enlarging the diameter of the holes located along one of the fiber symmetry axes can enhance the required mechanical asymmetry in the fiber cladding by preventing the transfer of applied external stress to the core along that axis, thus enhancing the pressure sensitivity. Based on this strategy, two PCFs with high pressure sensitivity and minimized cross-talk between the two normal modes of propagation have been designed and manufactured [132]. The cross sections of the fibers under test in the experiment, further denoted as fiber A and B, are shown in Fig. 5.4. Since the shapes of the air holes in the cross sections resemble the wings of a butterfly, the fibers are thus named "butterfly" fibers. Owing to the low cross-sensitivity of their birefringence to pressure and temperature, these Butterfly fibers are candidates of choice for experimenting in distributed pressure sensing. Earlier measurements [133] have shown that the average phase modal birefringence B of the 26.5 m-long fiber A is $7.2 \cdot 10^{-4}$ and the birefringence of the 48 m-long fiber B is $1.7 \cdot 10^{-4}$ at

¹Partial results of the presented work in this section have been published in © 2019 IEEE, S. Mikhailov, L. Zhang, T. Geernaert, F. Berghmans and L. Thévenaz, "Distributed Hydrostatic Pressure Measurement Using Phase-OTDR in a Highly Birefringent Photonic Crystal Fiber," in *Journal of Lightwave Technology*, vol. 37, no. 18, pp. 4496-4500, 15 Sept. 15/ 2019, doi: 10.1109/JLT.2019.2904756, where my contribution includes proposing and building the experimental setup, and performing the experiment.

$\lambda = 1550$ nm.

5.3.2 Experimental results

To demonstrate the pressure sensing capability of the aforementioned butterfly fibers, the samples are placed in a pressure chamber at various pressure levels, while monitoring the frequency shift difference between the orthogonal polarizations of each fiber. The differential frequency shift distributions along fiber A and B are shown in Fig. 5.5 (a) and (b), respectively. The measured birefringence decreases with increasing pressure and the pressure responses of the fibers are slightly non-uniform over their length. Such behavior can be caused by variations of the airhole microstructure along the fiber, small fluctuations of the polarization state of the scanning pulse over measurement time and pressure leakage from the chamber during the measurements (up to 0.2 bar/min).

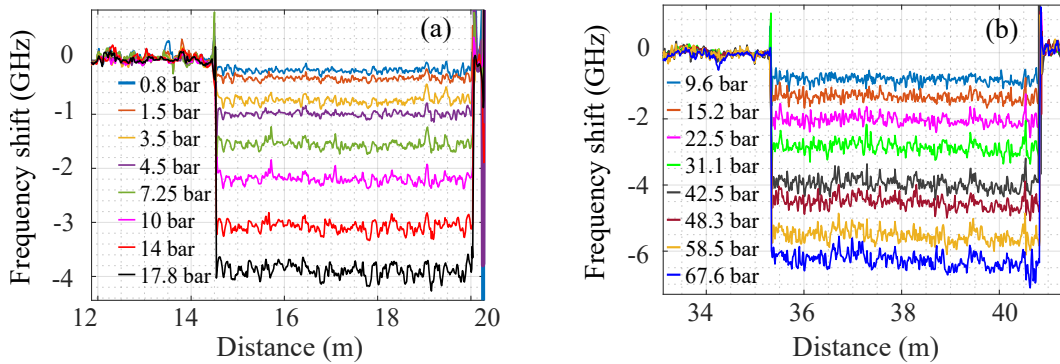


Figure 5.5 – Differential frequency shift distributions along (a) fiber A and (b) fiber B under various applied pressures, respectively

Fig. 5.6 shows the mean differential frequency shift as a function of pressure. The pressure sensitivities dv/dP are extrapolated from linear fits performed on the experimental data, yielding -219 ± 2.5 MHz/bar for fiber A and -95.4 ± 1.6 MHz/bar for fiber B, respectively. These values are in good agreement with previously reported measurements [133]. The standard deviation, i.e. the experimental accuracy on the determined values is computed by making use of the variations of the differential frequency shift along the unpressurized portions of the fibers. We found an accuracy of ~ 49 MHz (corresponding to a pressure accuracy of 0.22 bar) for fiber A, and ~ 52 MHz (pressure accuracy of 0.59 bar) for fiber B.

To the best of our knowledge, this is the first time that distributed pressure measurements are performed using ϕ -OTDR in two dedicated pressure sensitive "butterfly" PCFs. The pressure sensitivity of the samples is from 3.8 to 8.8 times larger than reported in other proposed distributed pressure measurements [116, 117, 36] based on PCFs. Sub-bar measurement resolution (up to 0.3 bar for the fiber with the highest pressure sensitivity and a frequency scanning resolution of 64.5 MHz) has been demonstrated. The maximal sensing length (~ 40 m

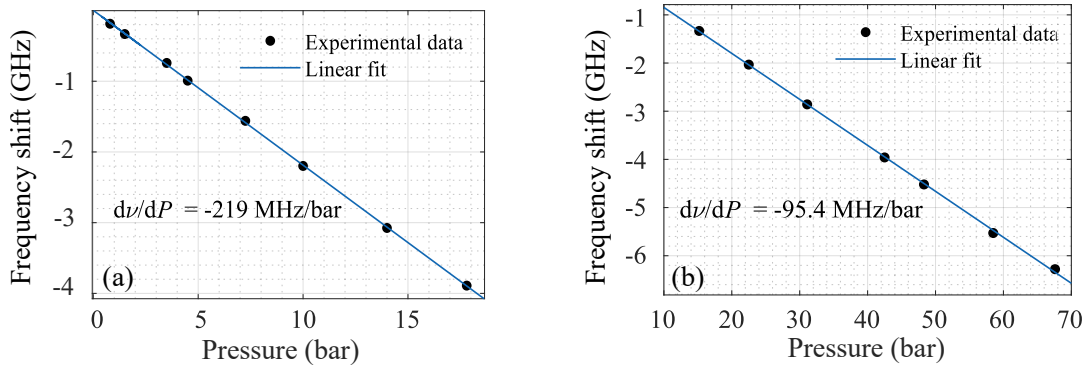


Figure 5.6 – Mean frequency shift in (a) fiber A and (b) fiber B as a function of pressure change

in the experiment) is limited by the high propagation losses of the studied fibers (~ 24 dB/km), but can theoretically be extended to a few hundred meters. However, achieving sensing over longer distances would require fibers with lower propagation losses.

5.4 Distributed pressure sensing using side air-hole fiber

5.4.1 Side air-hole fiber

In 1986, optical fibers known as side air-hole fibers (SAHF) were dedicatedly designed to achieve pressure sensing [101]. The two large air holes in their cladding bring a strong asymmetry to the fiber cross-section, with the direct purpose that external pressure variation will induce changes in the fiber birefringence. The sensitivity of SAHF to pressure is high since the volume occupied by the air holes as well as the asymmetry of the fiber cross section is large. [134].

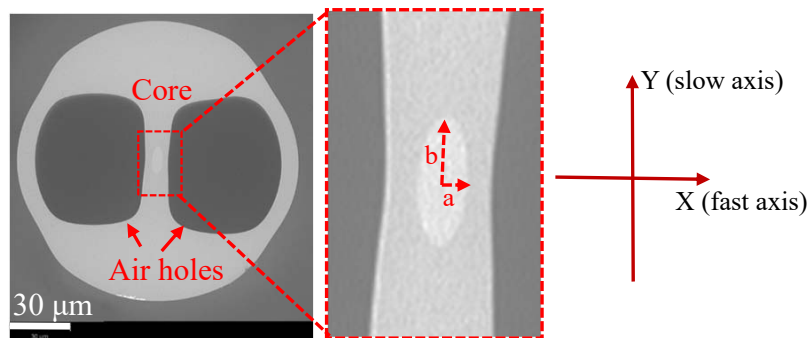


Figure 5.7 – SEM image of the cross section of side-hole fiber

The fiber we are using here is shown in Fig. 5.7. The fiber structure resembles the polarization-maintained panda fiber, except that, the fiber core is here surrounded by two large air holes instead of stress rods. Besides, the SAHF core is elliptical, with the lengths of the semi-minor

semi-major axes being $2.4 \mu\text{m}$ and $6 \mu\text{m}$, respectively. Normally, due to the large Young's modulus of silica, the impact of pressure on standard single mode fibers (SMF) or any other solid fiber made of glass is very limited, as discussed in Chapter 2. However, owing to the large air holes in the cladding of the SAHF, the stress induced by pressure loading on the fiber is better transferred to the Y axis (slow axis), resulting in a significant enhancement of the pressure sensitivity of this axis, similar to the butterfly fibers. Therefore, the phase change of Y axis (or slow axis) will be much larger than the X axis (or fast axis) under the same pressure change condition, resulting in a large FS in Y axis while the other axis shows little FS change as validated in the oil pressure chamber and illustrated in Fig. 5.2 (b).

Unlike butterfly PCFs presented in the previous section, which can also see their pressure sensitivity enhanced by inducing air holes in the claddings [135], the structure of the SAHF is simple and its core dimensions are similar to SMFs. This translates into much lower propagating loss (3 db/km) compared to butterfly PCFs (20 db/km) together with reasonable splicing loss (less than 1 dB), making SAHFs promising candidates for long distance distributed fiber sensing.

5.4.2 Experimental results

Pressure and temperature sensitivities

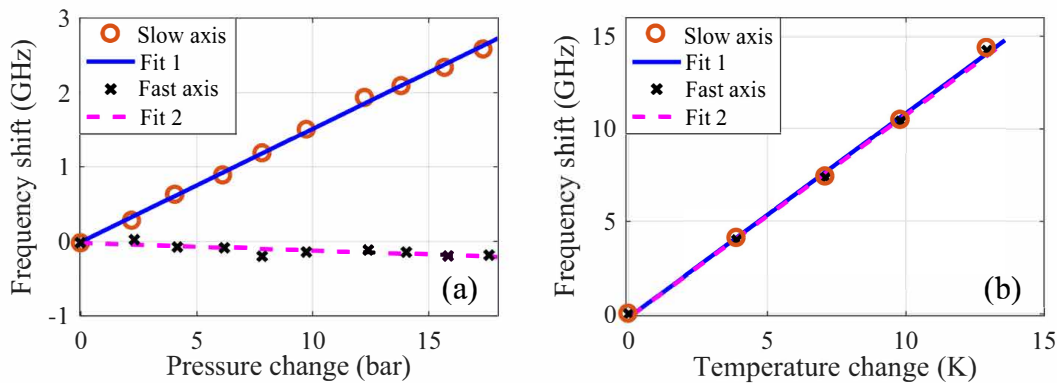


Figure 5.8 – (a) pressure and (b) temperature response along the two polarization axes of the fiber, respectively.

The SAHF under test shows a birefringence of $\sim 5 \times 10^{-5}$ in terms of refractive index for a total length of ~ 720 m. The fiber is first probed with a pulse width of 2 ns, corresponding to a spatial resolution of 20 cm. The pressure-induced frequency shift for the two orthogonal polarizations are measured from 0 to 18 bars respectively, and the results are drawn in Fig. 5.8(a). The sensitivities of the two axes are calculated to be 148.6 ± 9.5 MHz/bar and -10.4 ± 5.9 MHz/bar, respectively. The temperature sensitivity of the birefringence was also tested by placing a section of the SAHF into a temperature controlled water bath. From the results shown in

Fig. 5.8 (b) we can see that the responses in terms of frequency shift with respect to temperature on both axes are nearly the same. Furthermore, the measured sensitivity is similar to side hole fibers with fiber Bragg grating (FBG) imprinted on the fiber core [136]. The temperature sensitivities are 1.121 ± 0.091 GHz/K and 1.116 ± 0.089 GHz/K for the fast axis and slow axis, respectively.

The calculated change in birefringence due to temperature (6 MHz) by 1°C is much smaller than that of the variation induced by pressure (159 MHz/bar), which are both obtained as the difference from the individual responses of the fiber axes. The reason for the small temperature sensitivity is that, temperature induced phase changes are mainly due to the different thermal expansion coefficients between the cladding and the core of the fiber as well as from temperature-induced refractive index changes (thermal optics effect), which should be similar for both fast and slow axes.

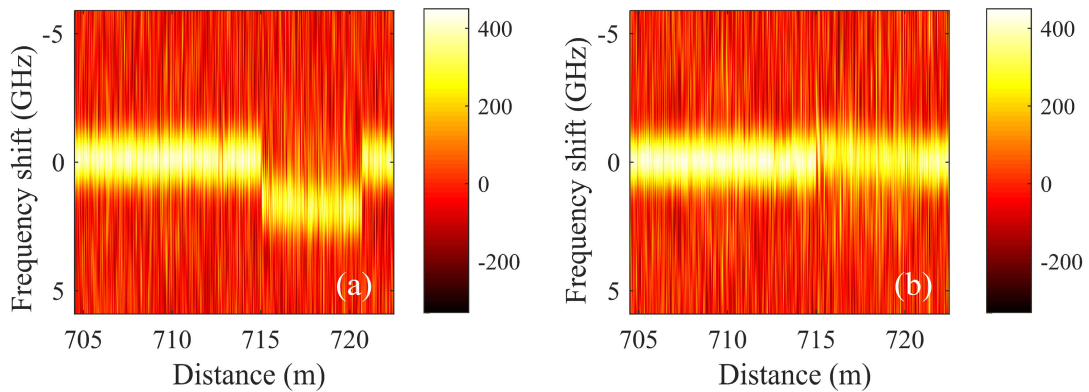


Figure 5.9 – Correlations of RS spectra when 12 bar pressure is applied. (a) slow axis; (b) fast axis. (5 cm spatial resolution)

Long-distance distributed pressure sensing with high spatial resolution

After characterizing the fiber sensitivities, the pulse width is brought down to 500 ps (i.e. 5 cm spatial resolution) in order to further evaluate performances of the system. The correlation spectra measured along both polarization axes under a pressure of 12 bar are illustrated in Fig. 5.9. A clear frequency shift can be seen for the slow axis (in Fig. 5.9(a)) but no frequency shift for the fast axis in Fig. 5.9(b). In Fig. 5.10, the pressure change distribution along the fiber is calculated through the pressure sensitivity obtained in the previous section. The results matches well with the applied pressure (12 bar) while the high spatial resolution of the measurement is demonstrated by observing the falling edge of the transition from high (12 bar) to low (0 bar) pressure in Fig. 5.10 (b). The calculated pressure accuracy is 0.49 bar.

It should be noted that the measured pressure variations are larger in the pressure chamber than out of the pressure chamber, which might be caused by some gas bubbles in the oil pressure pipe.

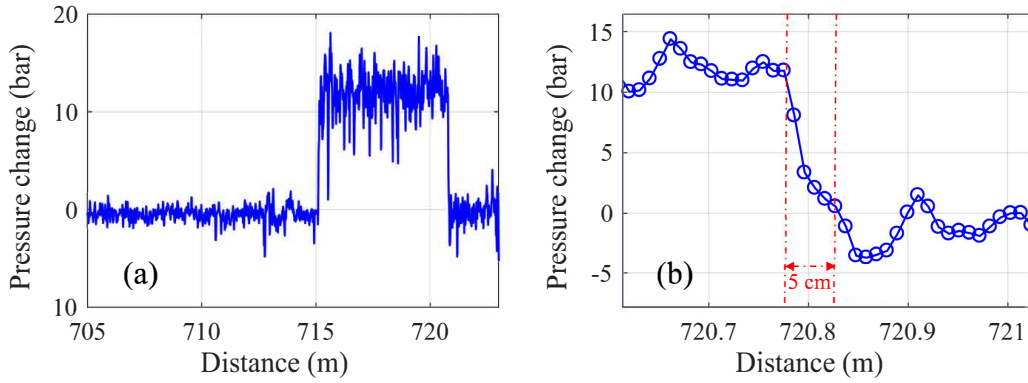


Figure 5.10 – (a) Pressure change distribution along the fiber; (b) Zoom-in at the pressure transition

Pressure and temperature discrimination

The different frequency shift responses in terms of temperature and pressure change on both polarization axes shown in Fig. 5.8 provide a way to discriminate the two measurands. Similar to [137], the frequency shifts of the system can be described as follows:

$$\begin{bmatrix} \delta F_{fast} \\ \delta F_{slow} \end{bmatrix} = \begin{bmatrix} S_{t,fast} & S_{t,slow} \\ S_{p,fast} & S_{p,slow} \end{bmatrix} \times \begin{bmatrix} \delta T \\ \delta P \end{bmatrix} \quad (5.2)$$

where δT , δP and δF are the temperature change, pressure change and the frequency shift of the system, respectively. The subscript of δF represents the polarization axis. $S_{i,j}$ is the sensitivity where i represents the temperature (t) and pressure (p), and j represents the polarization axis.

A demonstration of the discrimination between pressure and temperature/strain is shown in Fig. 5.11. The length of the fiber under test is 8 m. The first 3 m are placed into a water bath to keep the temperature constant while the last 2 m (6-8 m) are placed in a pressure chamber. About 3 m of fiber in between is exposed to air and is subject to room temperature change. The frequency shift responses on both polarization axes are measured at different pressures (3 bar, 6 bar and 9 bar). The results depicted in Fig. 5.11 (a) and (b), from which we can see that frequency shifts not only take place in the pressure chamber but also in the section of fiber exposed to air. Through Eq. 5.2, both the pressure and temperature changes can be retrieved, which are shown in Fig. 5.11 (c) and (d). The demodulated pressure changes match well the applied pressure (3, 6 and 9 bar), and we can see the influence of ambient temperature variations on the leading fiber between the water bath and the pressure chamber. It should be noted that the fiber unfortunately broke due to the expansion of the pipe during the experimental procedure, so that only 2 m of fiber in the chamber are probed. It also explains why the traces drop in the pressure chamber in Fig. 5.11 (d), which very likely originates from induced strain.

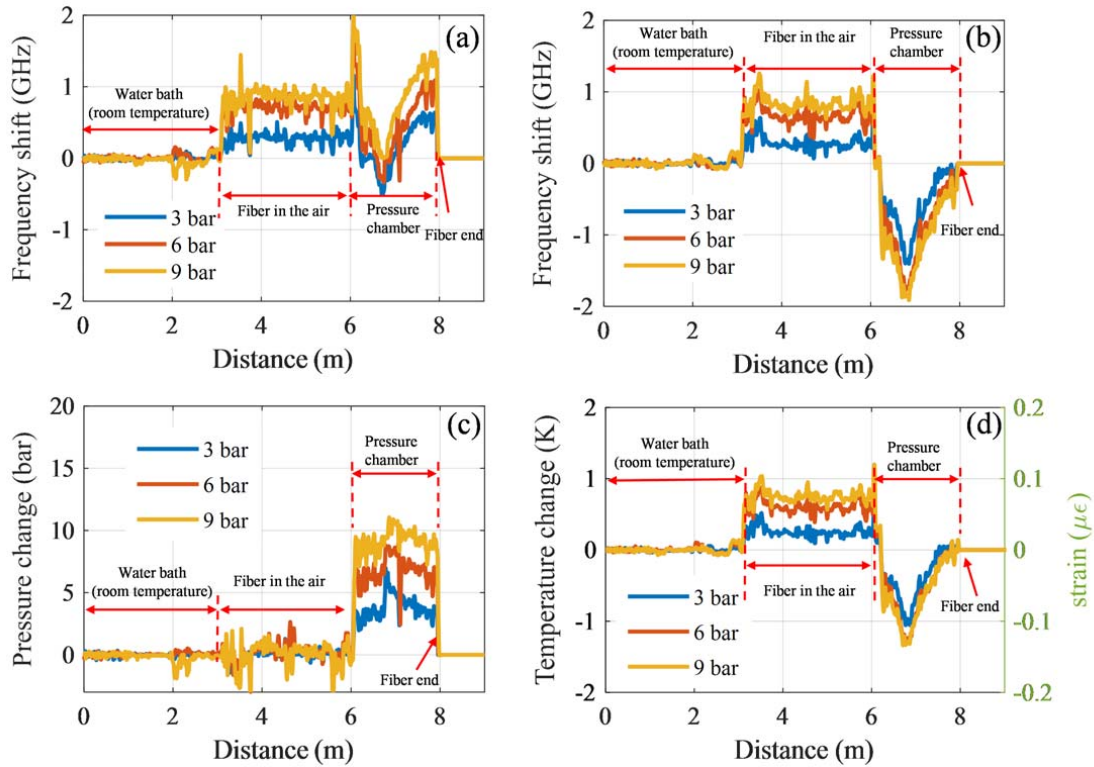


Figure 5.11 – Responses of (a) fast and (b) slow axis when 3 bar, 6 bar and 9 bar pressure changes are applied to the fiber; (c) pressure distributions and (d) temperature/strain distributions demodulated from the discrimination algorithm

5.4.3 Discussions

Crosstalk between pressure and temperature/strain

Although it is difficult to dissociate the impact from temperature and strain on the fiber, the temperature and strain sensitivities can be simply canceled out by subtracting the responses of the two axes as in Fig. 5.10. The experimental results show that the temperature sensitivity of the fiber birefringence is negligible (6 MHz/K), compared with the high pressure sensitivity (159 MHz/bar). In addition, the temperature sensitivity can be further reduced by proper fiber design. Indeed, the two main contributions to the birefringence change of the fiber induced by temperature are: first, the difference of the thermal expansion coefficients between the cladding and the core of the fiber; second, the temperature-induced change in the refractive index of the fiber [94]. The performances of the SAHF used in the experiments in terms of temperature sensitivity can hypothetically be improved on at least two aspects. First, the SAHF has two large air holes in the cladding, which may impact the birefringence through thermal expansion. Second, the core shape of the fiber is elliptic, so that the impact of a given temperature change on the effective refractive index of the two polarization modes is different, which will contribute to further modifying the fiber birefringence. It means that, with proper

design on the structure of the fiber, the temperature sensitivity on the birefringence can be alleviated and possibly completely canceled out when taking these two factors into account.

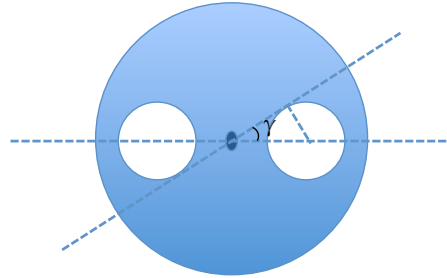


Figure 5.12 – The pressure sensitivity depends quadratically on the angle γ [138]

As for the dependency of the pressure sensitivity on the fiber geometry, it has been demonstrated that the pressure sensitivity is linearly proportional to γ^2 , where γ is the angle between the line connecting the core and air hole centers and the tangent to the air hole connected to the fiber center, as shown in Fig. 5.12 (the air holes is assumed to be circular for simplicity) [138]. As a consequence, the variation of the core ellipticity has in principle no impact on the pressure sensitivity.

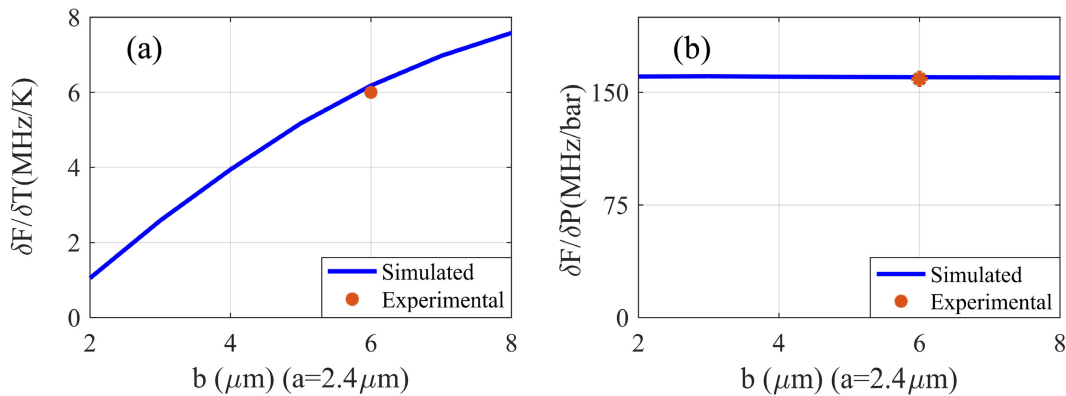


Figure 5.13 – (a) Temperature and (b) pressure sensitivities with different core diameters. Parameters used for simulation: 72 GPa, 0.17, 1.14×10^{-6} [1/K], and 5.5×10^{-7} [1/K] for Young's modulus, Poisson's ratio and thermal expansion coefficient for core and cladding, respectively

To verify this idea, simulations were run using Comsol by sweeping the length of the semi-major axis b of the elliptical core and calculating the pressure and temperature sensitivity of the birefringence of the fiber. The results are shown in Fig. 5.13, the blue lines denoting the sensitivity obtained from the simulations while the experimental results are represented as orange dots. The results show that the temperature sensitivity lowers as b decreases and reaches a value as low as 1.05 MHz/K when $b = 2 \mu\text{m}$, which is 5 times smaller than the SAHF we used in the experiment. However, the pressure sensitivity does not change much with the decrease of b . Finally, note that the experimentally measured sensitivity on the sample available are in excellent agreement with the values obtained from simulations.

It should be noted that, there exists a trade-off between the temperature sensitivity and fiber loss. As the core gets smaller, the optical field will be less confined in the core and the loss due to surface wave scattering will increase, thus limiting the sensing range. The uniqueness of SAHF is that it offers a high pressure sensitivity and a moderately low temperature sensitivity with small fiber loss, which is suitable for long range distributed pressure sensing. Note that reaching zero temperature sensitivity was addressed by making use of birefringent photonic crystal fibers [139].

Polarization crosstalk

Since the pressure sensitivities of the two polarization axes are different, the accumulated crosstalk between polarization distorts the Rayleigh spectrum when pressure changes are applied to the fiber, thus limiting the sensing distance of the system. This issue is addressed in this section.

Polarization mode-coupling is due to waveguide fluctuations and anisotropic Rayleigh scattering[140]. The strength of the polarization coupling can be characterized by the mode-coupling parameter:

$$h(\beta) = \frac{2\langle \hat{T} \rangle^2 l}{[1 + (\Delta\beta l)^2]} \quad (5.3)$$

where $\Delta\beta = |\beta_x - \beta_y|$ and β_x, β_y are the propagation constants of the two principle polarization axes, l is the correlation length of the fluctuations and \hat{T} is a constant satisfying that the local coupling coefficient $\Gamma_{xy}(z) = \hat{T}f(z)$ and $f(z)$ represents the fluctuation of the waveguide parameters. For high birefringence fibers, only polarization coupling due to waveguide fluctuation is taken into consideration, since its correlation length (in the order of 10^{-2} m) is much larger than that for Rayleigh scattering (much shorter than 10^{-6} m). We know that for Panda fibers, the mode coupling origin mainly from the deformations of stress-applying parts [141]. Similarly, here we assume that the deformations of the side holes is the main reason for mode coupling due to the structure resemblance between the two fibers. We may make the following approximation [141]:

$$\hat{T} = -\frac{2}{7}k(C_1 - C_2)(0.108 - \Delta)\hat{\theta}_d \text{ (m}^{-1}\text{)} \quad (5.4)$$

where k is the wavenumber in vacuum, C_1 and C_2 denote the stress-optical coefficients and $C_1 - C_2 = 3.36 \times 10^{-5} \text{ mm}^2/\text{kg}$, Δ is the relative difference in refractive indexes between core and cladding and $\hat{\theta}_d$ (in the unit of degree) denotes the rms deviation of the angle fluctuations in the side air holes.

As a rough estimation, we assume that $l = 0.01$ m, $\hat{\theta}_d = 0.2^\circ$, fiber length $L=1$ km and $\Delta = 0.4$ percent. The birefringence of our fiber is 5×10^{-5} at a wavelength of 1550 nm, so

the calculated $(\hat{T})^2 = 0.66 \text{ m}^{-2}$, $h = 6.4 \times 10^{-5} \text{ m}^{-1}$ and the crosstalk is then

$$CT \equiv 10 \log \frac{P_x}{P_y} = 10 \log(2 * hL) = -9 \text{ dB} \quad (5.5)$$

where the factor of 2 comes from the round-trip of the pulse.

It should be noted that waveguide deformations are intrinsic factors, laying the lower bound of the mode coupling. Microbendings and temperature fluctuations in real applications will also have an impact on the total crosstalk, which is beyond the scope of this work.

In summary, a long-distance distributed pressure sensing system has been demonstrated based on frequency-scanned ϕ -OTDR and a special design fiber exhibiting an elliptical core as well as two side air holes in the cladding. Thanks to the large air holes of the fiber, its birefringence is very sensitive to pressure change, i.e. the experimentally validated sensitivity is 159 MHz/bar, while the temperature sensitivity is only 6 MHz/K. Owing to the high sensitivity of ϕ -OTDR and low loss (transmission and splicing), long distance ($\sim 720 \text{ m}$) distributed pressure sensing is demonstrated with high spatial resolution (5 cm). The pressure/temperature sensitivity crosstalk and the polarization crosstalk are discussed.

5.5 Conclusions

In this chapter, frequency-scanned ϕ -OTDR has been explored for distributed pressure sensing:

- 1 Distributed pressure sensing has been proposed and demonstrated based on ϕ -OTDR for the first time to our best knowledge. In stead of direct measurement of birefringence change, it measures the phase change (by the frequency shift in the Rayleigh spectra) on the two orthogonal polarization axes of two highly birefringent PCFs. High sensitivity (-219 MHz/bar) and high spatial resolution (5 cm) have been demonstrated. The fibers have demonstrated ultra-low temperature sensitivity thus is fit for applications where zero temperature sensitivity is required; however, the fiber structure complexity results in much larger fiber loss and difficult in the fiber manufacture with long length.
- 2 Long-distance distributed pressure sensing has also been demonstrated experimentally with air side-hole fiber. Potential discrimination between temperature and pressure changes as well as polarization crosstalk have been thoroughly discussed. The large air holes in the fiber cladding increase the sensitivity on pressure and the simple structure of the fiber allows for low loss propagation such that the sensing range could be extended up to $\sim 800 \text{ m}$, which is the longest range achieved so far, which demonstrates the potential of such fiber for long distance pressure sensing. Besides, the fiber birefringence sensitivity on the temperature is moderately small. It is more suitable for the applications when the temperature impact is less essential.

6 Dynamic strain sensing

The content of this chapter is an extended version of a published article [142]¹, and this is a collaborative work with Tel Aviv University.

Distributed and dynamic fiber-optic sensing (DDFS) systems are an important branch of DOFSs, due to their potential in a wide range for applications, such as structural health monitoring (SHM), seismic detection and more [143, 144]. Many efforts have been carried out to push the sensing performance regarding to sensing range [145], spatial resolution [78, 146], measurand accuracy [77] and response frequency [147]. Relevant technologies are based on the Brillouin effect in standard fibers [24], the use of optical fibers imprinted with continuous fiber Bragg gratings [46] and finally, interrogation based on Rayleigh backscattering in standard single mode fibers.

Phase-sensitive optical time-domain reflectometry (ϕ -OTDR) [40], as an important Rayleigh-based distributed and dynamic fiber-optic sensing technique, has established itself as an effective and highly sensitive mean to probe standard single-mode fibers. As introduced in chapter 3, since a local strain linearly varies the phase of light reflected from the strain-affected scatterers, key to a proper retrieval of the strain variations along the fiber is phase demodulation of the backscattered light. Different phase demodulation schemes, such as detection using a 3×3 coupler [3], phase carrier modulation [80] and I/Q demodulation [82] were proposed.

In most applications, particularly in SHM, the strain change in a structure can be large and local, e.g., for the detection of cracks, therefore, a short spatial resolution associated with a large dynamic range is required in DDFS systems. Many efforts have been carried out to further improve the spatial resolution. To the best of our knowledge, all the systems with submeter spatial resolution are using coherent detection. Systems using linear frequency modulated interrogating pulses have been implemented in ϕ -OTDR, achieving the spatial

¹©2020 OSA. Reprinted, with permission from L. Zhang, Z. Yang, N. Gorbatov, R. Davidi, M. Galal, L. Thévenaz, and M. Tur, Distributed and dynamic strain sensing with high spatial resolution and large measurable strain range, Opt. Lett. 45, 5020-5023 (2020), doi=10.1364/OL.395922.

resolution to the 90 cm [78] and 34 cm [146]. Yet another ϕ -OTDR implementation based on Perfect Periodic Autocorrelation (PPA) coding, claims DDFS with a demonstrated spatial resolution of 10 cm [83]. As addressed in chapter 3, in the coherence detection systems, the coherent length of the laser may limit the sensing range, and the demonstrated strain range is limited to a magnitude of hundreds of ne (nanostrain) in the systems mentioned above.

Instead, in direct detection as frequency-scanned ϕ -OTDR, the phase change of the scattered light induced by the strain can be retrieved from an equivalent spectral shift of the Rayleigh interference pattern; however, the scan process of the light frequency limits the measurement time, so that frequency-scanned ϕ -OTDR is often used for static quantitative measurement of the strain and temperature changes, as demonstrated in chapter 4 and 5. A fast frequency-scan scheme has been proposed by a direct modulation of the laser current [148]. Alternatively, a single-shot measurement has been demonstrated using chirped-pulses ϕ -OTDR [93]. These system allows a distributed and dynamic strain sensing using direct detection, thus the sensing range is not intrinsic limited by coherence of the laser; on the other hand, the spatial resolution in these systems is not shorter than a few meters due to the low Rayleigh scattering coefficient.

In this section, we have tried to upscale the frequency-scanned ϕ -OTDR from a static system to a *direct-detection* distributed and dynamic strain system with high spatial resolution and large measurable strain range, based on frequency-scanned ϕ -OTDR. The key to achieve both the high spatial resolution and high speed simultaneously is a high frequency, high speed RF pulse modulation scheme in the setup, offering:

- 1 Practically zero latency in the frequency scanning, enabling a fast scanning speed;
- 2 High extinction ratio for the employed narrow optical pulses, to avoid any spatial crosstalk, thereby ensuring proper high spatial resolution. This will be detailed in Section 6.1.2.

A backscattering-enhanced fiber is implemented as sensing fiber, providing a back-scattered signal strong enough to eliminate the need for averaging, thereby making measurement sampling rate limited only by the fiber length and the number of frequency scanning steps. A post-processing algorithm based on a previously developed least mean square algorithm [34] (in chapter 3) is employed, allowing the minimization of the number of frequency scanning steps.

6.1 Experimental setup

6.1.1 Setup

The scheme of the sensing system is depicted in Fig. 6.1. A DFB laser with a standard 1 MHz linewidth is used as a light source. An EOM biased in carrier-suppressed mode, driven by a fast

arbitrary wave generator (AWG) (M8195A 65 GSa/s, courtesy of Keysight/Israel), together with a tunable sharp-edges optical filter (Filter 1, bandwidth of 45 GHz covering the full scanning range) and an Erbium-doped fiber amplifier (EDFA1), consist the subsystem that generates short and strong pulses with a high extinction ratio, see below for more details. The amplified pulses are then launched into the fiber under test (FUT) through a circulator. The Rayleigh backscattered light from the fiber is pre-amplified before the photodetector (PD) by EDFA2, whose amplified spontaneous emission (ASE) noise is strongly suppressed by another tunable optical filter (Filter 2, identical to Filter 1). A 1 GHz wide photodetector converts the optical signal into an electric voltage, which is then digitized by a fast oscilloscope. Strain is applied to a 30 cm segment at the end of a 55 m sensing fiber. The fiber segment is anchored on one side while its other end is glued to a movable PZT stage, which is driven by a sine/triangular wave generator.

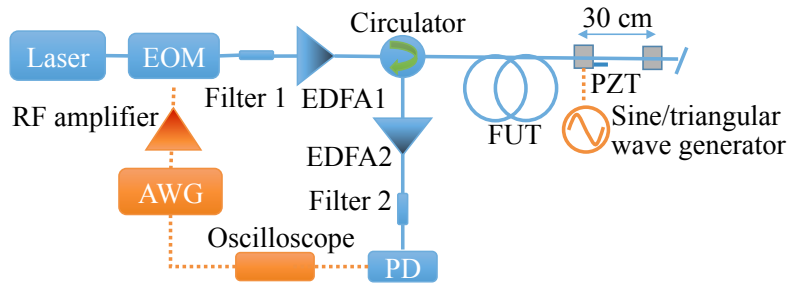


Figure 6.1 – Schematic of the experimental setup. AWG: arbitrary waveform generator; EOM: electro-optic modulator; FUT: fiber under test; PD: photodetector. The AWG helps the generation of short, high extinction ratio pulses, over a precise wide frequency range with close to zero switching latency

6.1.2 RF pulsing scheme

As mentioned in Chapter 3, in any time-domain distributed optical fiber sensor (DOFS), the extinction ratio of the modulation for the optical pulse is an important parameter, especially for a large number of resolved points.

In the previous chapters, two cascaded EOMs are used to secure a high enough ER. Here, to achieve high spatial resolution and minimize spatial crosstalk, we use an RF (radio frequency) pulsing scheme [105], in which an electro-optic modulator (EOM) modulates the light intensity at a preset high RF frequency and this modulation is *on* during the target pulse duration W . Then a single modulation sideband is selected by optically filtering out all other modulation spectral lines, including the optical carrier. The pulse extinction ratio, therefore, depends essentially on the optical filter rejection characteristics rather than on the modulator extinction ratio. This principle is schematically presented in Fig. 6.2, where a sequence of N RF pulses, spaced T apart and of width W , each carrying a different RF frequency (from 8 to 20.5 GHz in 50 MHz steps), are derived from the AWG.

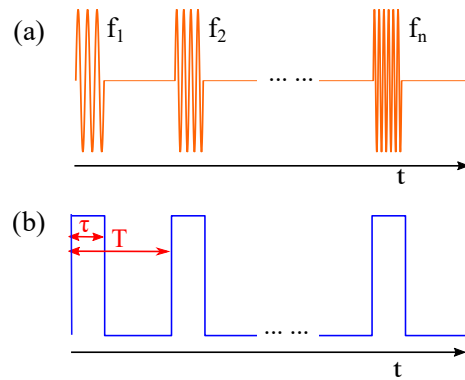


Figure 6.2 – Schematic diagrams of (a) the RF signal applied to the EOM and (b) the envelope of the generated pulse train after Filter 1.

The schematic diagrams of the RF signal applied to the EOM and the envelope of the generated optical pulse after Filter 1 are shown in Fig. 6.2 (a) and (b). The measured optical spectra before and after Filter 1 are shown in Fig. 6.3 for $T=0.6 \mu\text{s}$, allowing the interrogation of FUTs up to 60 m long and $\tau=2 \text{ ns}$ (20 cm of spatial resolution). It can be seen that both the carrier and the higher wavelength sideband are highly suppressed. Based on the ratio between the average powers of the transmitted sidelobe and the carrier (33.76 dB) and using the pulse duty cycle of 0.33%, the extinction ratio (the ratio between pulse peak power and carrier power) is determined to be 58.46 dB.

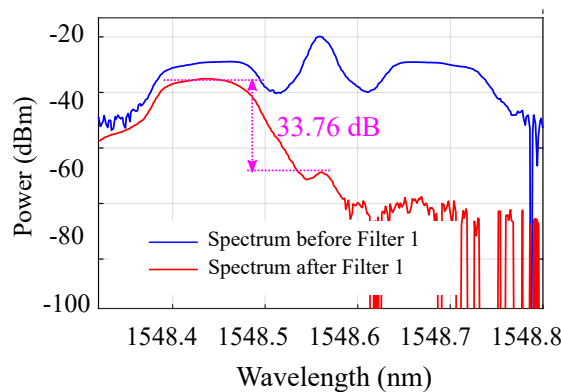


Figure 6.3 – Measured spectra of light before and after Filter 1 ($T=0.6 \mu\text{s}$ and $\tau=2 \text{ ns}$).

6.1.3 Backscattering-enhanced fiber

As discussed in Chapter 3, there is a trade-off between the sensing distance and spatial resolution. To have both high spatial resolution and long distance, averaging is performed for the OTDR traces to a high enough SNR in the previous experiment and it slows down the

sampling rate of the sensing systems by a factor of average time of N_{ave} .

To break the limit of the SNR on the measurement speed and sensing distance, approaches to enhance the Rayleigh backscattering have been proposed, including:

- 1 Increasing the numerical aperture (NA) of fiber through increasing the doping in the core, so that more Rayleigh scattered light is recaptured by the fiber [149];
- 2 Increasing the defects in the fiber by exposing the fiber to pulsed radiation, to obtain larger scattering intensity from them, rather than from the intrinsic density fluctuations [150]

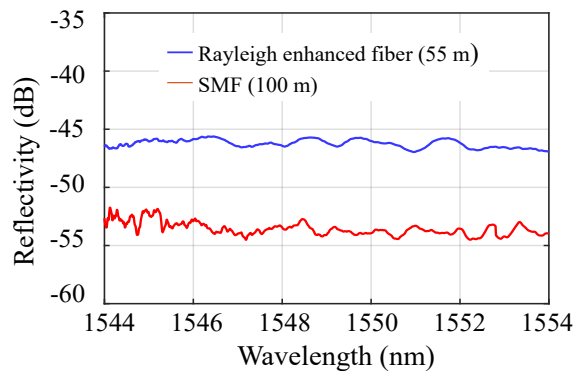


Figure 6.4 – The enhanced backscattering from the special fiber [104] used in the experiment. The two fibers were illuminated with the ASE from an EDFA and measured with an optical spectrum analyzer using a circulator. The reflectivity here is defined as the reflected spectrum normalized by the input spectrum.

The improvement of the first method is limited since the allowed doping increase is small due to the requirement of single-mode propagation and it also induces large attenuation; As for the second method, the elastic scattering can be well above the intrinsic Rayleigh scattering. Particularly through the exposing formation of periodic or quasi-periodic fiber Bragg gratings, the backscattering is enhanced without significant increase of the fiber loss, since only the backscattered light (not the other direction) is increased due to the periodic pattern in the fiber. Different methods have been developed for writing gratings over long fiber length such as point-by-point writing with ultraviolet [151] and infrared lasers [152], reel-to-reel setups [153], etc. Nearly continuous backscattering over many meters in fibers has been achieved using reel-to-reel fiber handling and a UV transparent coating [154], and based on this fabrication approach, works has been reported obtaining more than 10-dB increase in optical backscattering over the native Rayleigh scattering of the optical fiber with a length excess 10 km [104] and only 0.1 dB/km increase in the fiber loss.

In this experiment, to avoid slowing down the sampling rate with averaging and to still maintain a respectable signal to noise ratio (SNR), such a backscattering-enhanced fiber (cour-

tesy of OFS Ltd) is used, offering a significantly higher back-scattering signal, as compared to a standard single mode fiber, see Fig. 6.2.

6.2 Experimental results

6.2.1 Frequency shift estimation using cross correlation

First, a rather weak ($\sim 2 \mu\epsilon$ in amplitude), 1 kHz sinusoidal signal was applied to the PZT stage and the fiber was interrogated with $N=251$ frequency steps, leading to a strain sampling rate of $1/(T \cdot N)=6.64$ kHz. The demodulated response from the fiber is shown in the time-distance and frequency-distance maps of Fig. 6.5. The color scale maps the strain change along the fiber, which is calculated from the frequency shift between each measurement spectra and the reference spectra through cross correlation. Strain variations are clearly visible only at the vibrating segment, located at 53.5 m of distance in the fiber.

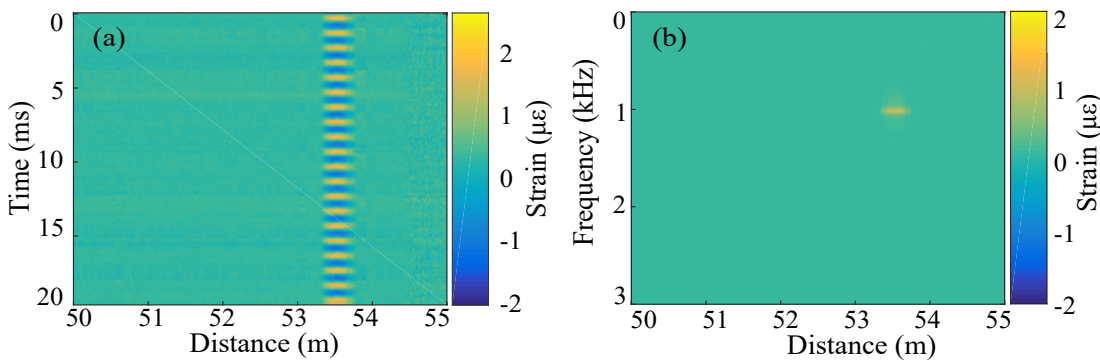


Figure 6.5 – Strain distribution along the fiber: (a) Time domain; (b) Frequency domain based on FFT of a 20 ms long acquisition.

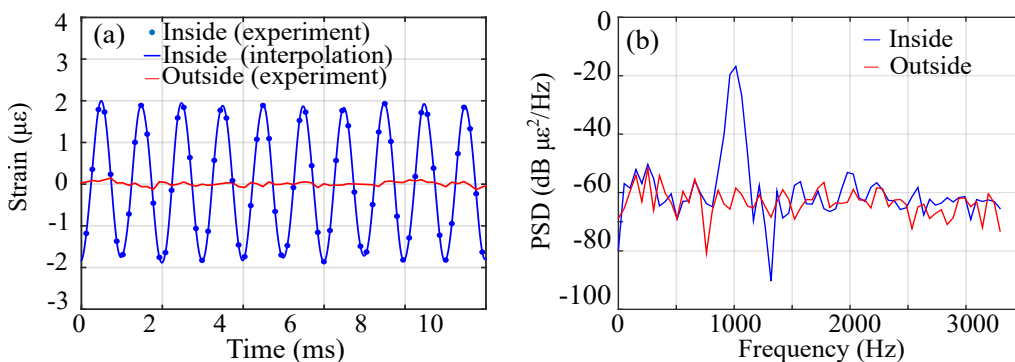


Figure 6.6 – Demodulated strain inside and outside of the vibrating fiber segment: (a) Time domain; (b) Power spectral density.

Fig. 6.6 shows the demodulated signals at 53.5 m (inside the vibrating segment and at 54 m (out of it), again in both domains: (a) Time (together with a sinc interpolation) and (b) Power spectral density (PSD) (Hanning-weighted periodogram-based PSD). The PSD of the strain in the vibrating section (Fig. 6.6 (b)) reveals a weak harmonic at 2000 Hz. Since no crosstalk is observed in the non-vibrating section, its signal will be treated hereafter as a noise reference, having an average value of $<1.3 \text{ n}\epsilon/\sqrt{\text{Hz}}$ below $\sim 700 \text{ Hz}$ and $<0.7 \text{ n}\epsilon/\sqrt{\text{Hz}}$ for higher frequencies, probably due to a larger environmental acoustic noise at lower frequencies.

Fig. 6.7 presents a temporal snapshot of the distribution of strain amplitude around the vibrating fiber segment. The rising edge is 20.3 cm, which is close to the expected spatial resolution from a 2 ns interrogating pulse width.

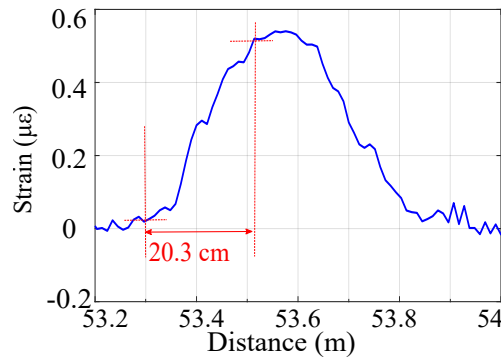


Figure 6.7 – Instantaneous strain distribution around the vibrating fiber segment, demonstrating the actual 20 cm spatial resolution.

6.2.2 Using least mean square

To further increase the measurement sampling rate by reducing the number of scanning frequencies, N , while keeping the same strain coverage (as determined by the frequency scanning range), as well as the frequency step size, we adopt a recently introduced least mean square algorithm that was shown to successfully extend the measurable range of frequency-scanning ϕ -OTDRs, while keeping a reduced number of scanning frequencies [34].

We first apply $N=251$ scanning steps to obtain a reference spectrum for each sensing position with the fiber statically at rest, covering the maximum measurable range offered by the $f_{max} - f_{min}=12.5 \text{ GHz}$ scanning range. Then, in operation, only $N = 60$ frequency scanning steps are used for dynamic measurements, allowing a response time of $36 \mu\text{s}$, which translates to a sampling rate of 27.8 kHz . The penalty on the strain accuracy remains minor ($<1.8 \text{ n}\epsilon/\sqrt{\text{Hz}}$).

To demonstrate the sensing capability for sizable strain variations, a 100 Hz triangular voltage signal, generating a peak-to-peak strain variations of $60 \mu\epsilon$, was applied to the PZT

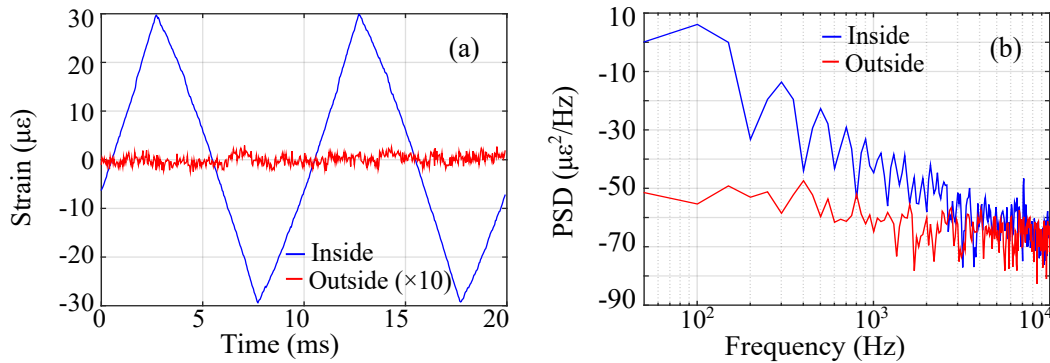


Figure 6.8 – Demodulated strain for a triangular driving voltage inside and outside of the vibrating segment: (a) Time domain; (b) Power spectral density.

stage and the measured strain is shown in Fig. 6.8. The observed deviations from linearity in the rise and fall sections of the recorded signal, Fig. 6.8(a), are probably due to the way the fiber-loaded stage generated the large, multiple-harmonics dynamic strain signal (Fig. 6.8(b)). The maximum stretching range of the PZT prevented us from achieving the maximum strain coverage $>80 \mu\epsilon$, which is the frequency scanning range (12.5 GHz), divided by the strain sensitivity ($150 \text{ MHz}/\mu\epsilon$) of this fiber. The noise average value is $<1.8 \text{ n}\epsilon/\sqrt{\text{Hz}}$ below $\sim 700 \text{ Hz}$ and $<0.7 \text{ n}\epsilon/\sqrt{\text{Hz}}$ for higher frequencies. The higher accuracy in the low frequency range compared with the previous scan scheme, is believed to be due to the environmental noise when acquiring the data. Note that in this technique the strain-induced frequency shift is estimated by correlating the dynamically varying spectra with a single reference spectrum. This procedure avoids noise accumulation which accompanies techniques which sum up differential strain changes [155].

While for a longer fiber the maximum sampling rate will decrease, for many applications, however, it will still be in the range of hundreds of Hz (*e.g.*, a 1 km sensing fiber allows for a sampling rate of 1666 Hz).

6.3 Conclusions

In conclusion, we demonstrated a simple configuration, based on a stable optical scheme, capable of detecting fast vibrations and localized faults of sizable strain, such as structural cracks. The proposed solution relies on simple direct detection and performs the function of frequency-scanning ϕ -OTDR using RF pulse modulation. The response time could be substantially improved using a backscatter-enhanced fiber, further highlighting the large potential of such fibers for distributed sensing [156].

For a direct-detection system a record high spatial resolution of 20 cm is demonstrated, concurrently with a relatively large strain measurement range of $60 \mu\epsilon$. Employing the least

mean square algorithm that requires a much restricted set of frequency scanning points, and benefiting from the practically instantaneous frequency switching and no averaging, we achieve a fast measurement sampling rate of 27.8 kHz, very close to the maximum possible value of 30 kHz for a 55 m long sensing fiber with 60 frequency steps. While not used here, real-time generation of strain values from the measured spectra seems to be technically possible using fast digital signal processors. For applications involving hundred of meters of fiber, this technique can reliably measure bandwidths of hundreds of Hertz at sub-metric spatial resolutions using a robust system compatible with field and on-board tests.

7 Distributed hydrogen sensing

The content of this chapter has been published in [142]¹, and this is a collaborative work with Maximilian Fisser from Victoria University of Wellington.

As a potential clean energy source, hydrogen is used for a variety of applications in the chemical and energy industry. The wide explosion range (4–75% in air), small ignition energy (0.02 mJ), large flame propagation velocity, and difficulty of leak-tight storage, demand hydrogen detection with fast and accurate response [157]. In particular, distributed gas sensing with a long sensing range is highly desired in today's complex industrial facilities, gas delivery systems and civil infrastructure sites.

Several distributed optical fiber sensors (DOFSs) for hydrogen detection have been reported [158, 159, 160], however, their performance is limited. In [158], the sensitivity is relatively low since the system is based on the loss of the pulse; in [159, 160] the sensing range are very limited because of the large loss of the acoustic wave propagating along the fiber [159] and the coherence of the laser [160].

Due to the inert chemical property of silica, optical fiber sensors for hydrogen detection often rely on palladium (Pd) as a transductive sensing element [157]. Atomic hydrogen is dissociated on the Pd surface and absorbed into the lattice. The absorption goes along with a volumetric expansion of the Pd. The expansion, which is correlated to the hydrogen concentration will apply a strain to the fiber, which is then measured by the optical fiber sensor [161]. This process is fully reversible, if any phase change is avoided [162].

In this section, we propose a distributed hydrogen monitoring system based on frequency-scanned ϕ -OTDR and a fiber customized by adhesively bonding thin Pd foils to it. A sensor design has been previously validated for fiber Bragg gratings [163]. In contrast to conventional coating process, Pd foils show a larger cross-sectional area, so that the hydrogen sensitivity is much enhanced. As a result, by measuring the strain change induced by the Pd foils

¹©2018 OSA. Reprinted, with permission from L. Zhang, M. Fisser, F. Yang, and L. Thévenaz, "Distributed hydrogen monitoring with phase-sensitive optical time-domain reflectometry," in 26th International Conference on Optical Fiber Sensors (2018), paper ThE17., doi=10.1364/OFS.2018.ThE17.

absorption, an ultra-high sensitive distributed hydrogen sensing with 5 cm spatial resolution is demonstrated.

7.1 Sensing fiber design

The customization for hydrogen sensing is based on an Ormocer coated fiber (FBGS, Germany) and segments with adhesively bonded Pd foils. As a conceptual demonstration, a fiber with 4 Pd-foil sensing segments have been prepared. The segments are each 50 mm long and the distance between the segments is 0.4 m. The segments structuring is made of the fiber sandwiched between two 20 μm thick Pd foils (width 2 mm) and bonded using a bisphenol-a epoxy resin. A custom tool, based on vacuum bagging, allows the compression of the foil-fiber composite while curing the adhesive at 100 $^{\circ}\text{C}$, generating a thin bond line between foil and fiber [163]. An SEM image of the cross-section of the sensor is shown in Fig. 7.1 (to generate a contrast between adhesive and potting epoxy, the latter was filled with silica nanoparticles). The image reveals a thin bond line on two sides between foil and fiber, and two large voids on the other side of the fiber. This design enables a much larger strain than conventional Pd coated fiber and increase the sensitivity by more than 10 times.

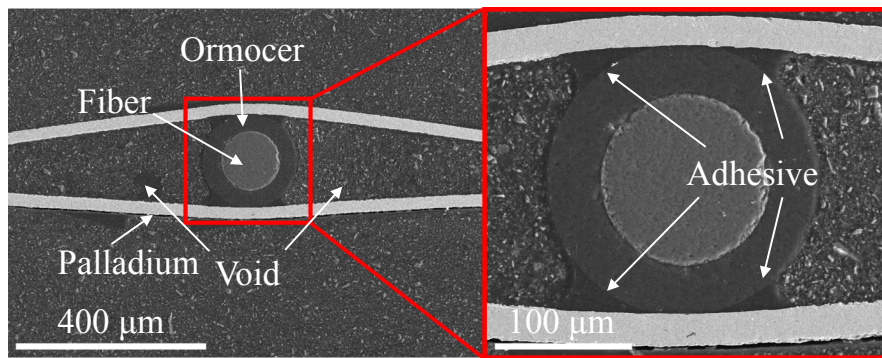


Figure 7.1 – SEM image of the cross-sectional view of the sensor. To increase the visibility of the adhesive, the SEM potting epoxy was filled with silica nanoparticles.

7.2 Experimental setup

A schematic drawing of the experimental setup is shown in Fig. 7.2. We use a distributed feedback laser with 1 MHz linewidth as a source. Two cascaded electro-optical modulators (EOMs) are used to modulate the continuous wave into pulses with a width of 500 ps, which result in a spatial resolution of 5 cm. Then an Erbium-doped fiber amplifier (EDFA) and a variable optical attenuator are used to deliver enough peak power to the pulses while preventing any nonlinear optical effect. The Rayleigh scattering signal is pre-amplified before the photodetector using another EDFA. The amplified spontaneous emission (ASE) noise of the EDFA is filtered out using a 1 nm bandwidth filter. The bandwidth of the photo-receiver is 3 GHz. A sampling rate of 10 Gs/s is set for the oscilloscope to digitize the electrical signal,

which is further analyzed by the software.

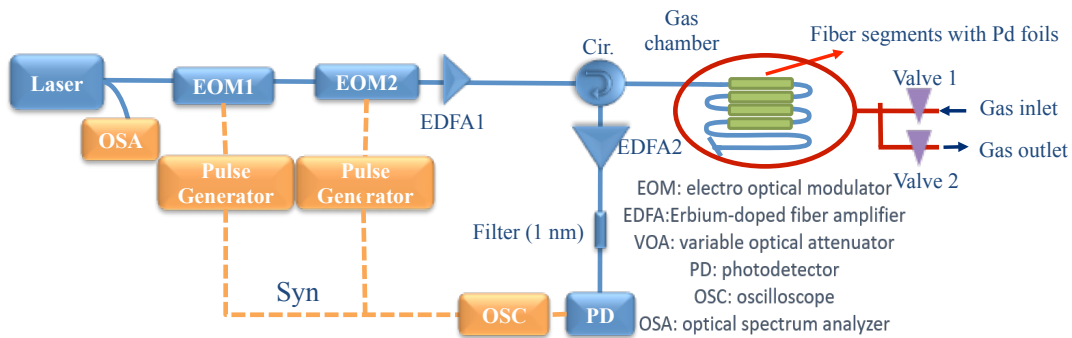


Figure 7.2 – Experimental setup for distributed hydrogen sensing

Short optical pulses with high enough extinction ratio are generated using a couple of cascaded EOMs. Since the pulse width is set to 500 ps, corresponding to a signal bandwidth of 2 GHz, a frequency scan step of 200 MHz is fine enough to recover the spectra at the sensing points. In this case, the frequency scanning can be performed by directly tuning the temperature or the current of the laser. In a first stage, a broad frequency range (100 GHz) is scanned by temperature-tuning the laser, as a reference to map large strain changes. Then a relatively small frequency range (20 GHz) is scanned for measurements by laser current tuning to enable a fast scanning (less than 10 seconds).

As a demonstration, the fiber we used is about 5 m long and 4 Pd foil segments are placed in a gas test chamber. To test the hydrogen sensing performance of the sensor, a reference is taken when the chamber is filled with air. Then the chamber is evacuated and filled with gas with different hydrogen concentrations. The expansion of the Pd due to hydrogen absorption induces strain change to the fiber. These changes are interpreted by different frequency shifts in the spectra obtained by the interrogator. To avoid a phase change of the Pd, the used hydrogen concentrations are kept below 1% at room temperature.

7.3 Experimental results

To test the monitoring ability of the system, we apply different hydrogen concentrations in the chamber during the 6 hours-long monitoring and the measurements are taken consecutively every minute over the 6 hours. We call each hydrogen concentration change in the chamber an event and 4 events are set during the campaign:

- 1 Event 1 at 20th minute: gas injection with 0.30% hydrogen;
- 2 Event 2 at 70th minute: gas injection with 0.38% hydrogen;
- 3 Event 3 at 85th minute: chamber vacuum, followed by ambient air injection;
- 4 Event 4 at 125th minute: gas injection with 0.60% hydrogen.

First, the frequency shift of the sensing fiber as a function of position along the fiber is shown in Fig. 7.3. The 6 traces in Fig. 7.3 correspond to responses taken every 5 minutes immediately after exposing the sensor to the gas with hydrogen concentrations of 0.3% and 0.6%, respectively. Clear peaks can be observed at 4 positions along the fiber, which correspond to the 4 fiber segments wrapped in Pd foils. The frequency shifts increase with time and a higher frequency shift at a given exposure time corresponds to a higher hydrogen concentration. Owing to the large Pd cross-sectional area, and good strain transfer of the sensor design and the sensitivity of the interrogator, the system shows a high sensitivity and observable frequency shifts can be obtained after the first minute of exposure to hydrogen with a concentration as low as 0.3%.

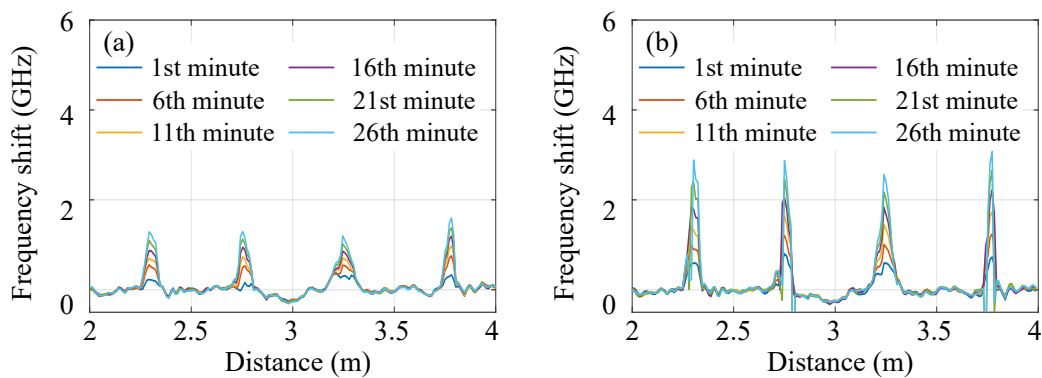


Figure 7.3 – Frequency shift responses of the sensing fiber every 5 minutes in half an hour: after exposing the sensor to the gas with hydrogen concentrations of (a) 0.3% and (b) 0.6%, respectively

The frequency shift temporal evolution of the 4 sensing segments is illustrated in Fig. 7.4. All the traces show initial sharp increases of the frequency shift when the hydrogen concentration is raised (Event 1, Event 2 and Event 4 in Fig. 7.4), even for a small increment from 0.3% to 0.38% (Event 2 in Fig. 7.4). Details of the trace change of Event 1 and Event 2 are drawn in Fig. 7.5. On the other hand, the frequency shift decay is clearly observed after the gas with hydrogen is evacuated (Event 3 in Fig. 7.4) and then a faster increase resumes when the fiber is exposed to 0.6% hydrogen (Event 4 Fig. 7.4), which makes fully sense for a doubled concentration.

This essentially demonstrates the ultra-high sensitivity of the system for distributed hydrogen monitoring and its relatively fast response entirely related to the Pd intrinsic reactivity. It should be noted that the responses of the 4 sensing segments are not identical, which result from the non-uniform strain transfer of the palladium foils to the fiber. This can be calibrated by measuring the temperature or strain sensitivity of the fiber, as addressed in [161]. Besides, there is a sharp drop of frequency shift for sensing segment 2 in 0.6% after 220 minutes. This is widely unexplained, but a tentative explanation may be a birefringence change in the fiber when subject to an increasing strain, as a result of the asymmetric structure of the sensing

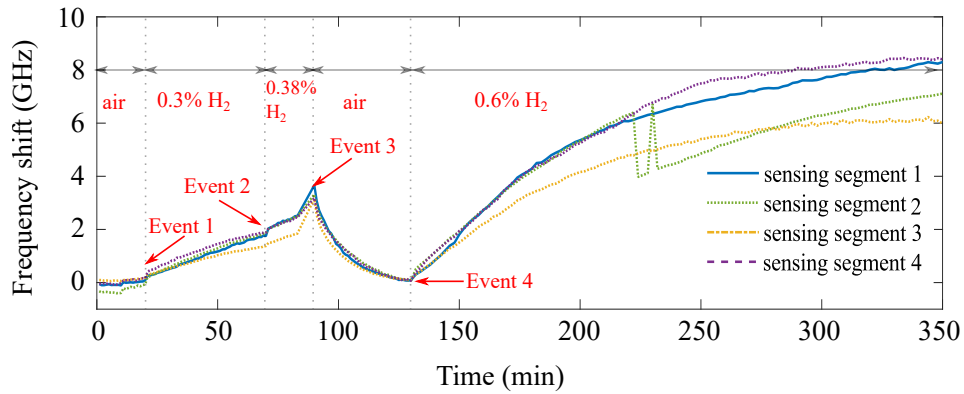


Figure 7.4 – Frequency shift responses of the 4 sensing segments over 6 hours. The hydrogen concentration-changing events are indicated in the time chart.

segment (as shown in Fig. 7.1). This leads to a mismatch between the polarization state of the interrogating pulse and the fiber eigen polarization axis and this needs to be confirmed in a future work.

It should be noted that, the impact of the temperature variations on the frequency shift has been compensated by using as reference the measured values from segments without bonded Pd foils. The silica fiber by itself is inert to hydrogen, so that it turns out to be only sensitive to temperature. Another point worth to mention is that the system has a spatial resolution as sharp as 5 cm. In this proof-of-concept implementation, the total length of the sensing fiber is only 5 m; however, the distance range of the sensor can easily reach 1 km, which offers a potential for an extended sensing coverage.

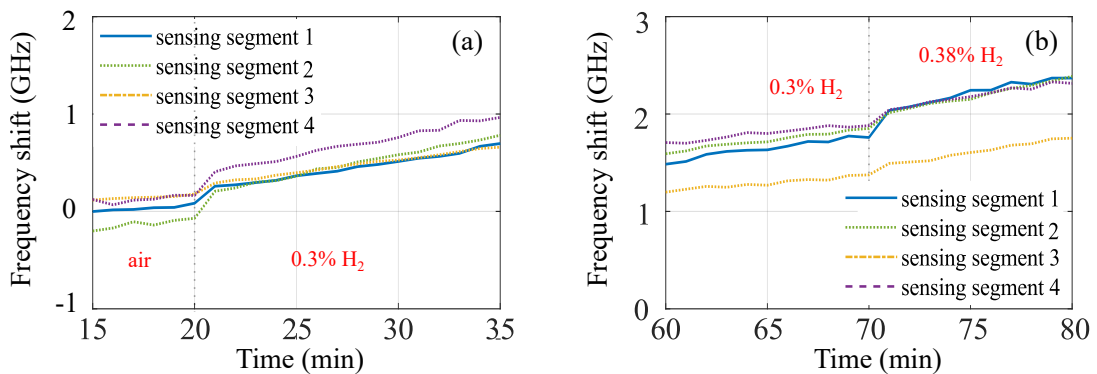


Figure 7.5 – Frequency shift response when the hydrogen concentration changes from (a) 0% to 0.3%; (b) 0.3% to 0.38%

The resolution of the system is not quantified experimentally mainly due to the limited experimental condition: the response of the hydrogen absorption will be linear provided that no phase transition occurs. This must be secured to benefit from a full response of the

Pd and to make the analysis of the results possible. The phase transition pressure depends on temperature that must be kept very low for low hydrogen concentration [161]. However, neither the hydrogen concentration nor the temperature of our gas chamber can be set accurately. Nevertheless, under the assumption that no phase transition occurs, we can make a rough estimation of the noise equivalent hydrogen concentration (which is a parameter more often used to describe the hydrogen detection performance) based on the previous literature and our experiment results: the wavelength shift sensitivity of the fiber is 250 pm per 1% H₂ at 1550 nm, corresponding to 31.2 GHz per 1% H₂ [163]. The calculated uncertainty of our system is 0.034 GHz. Therefore, the noise equivalent hydrogen concentration is about 10⁻⁵, i.e. 10 ppm.

7.4 Conclusions

In summary, a distributed hydrogen sensing system is proposed for the first time based on frequency-scanned ϕ -OTDR and a fiber with adhesively bonded Pd foils. The optimized design of the customized fiber and the high sensitivity of the interrogator allow a fast response to a small change of hydrogen concentration. A concentration 10 times lower than the explosive level of 4% can be detected in less than one minute over potentially up to 20'000 independent sensing points (5 cm spatial resolution over 1 km) along the optical fiber.

It should be noted that, all the sensing systems demonstrated in chapter 4-7, are showing high sensitivities and high spatial resolution (20 cm for pressure sensing and dynamic strain sensing; 5 cm for hydrogen sensing). It must be mentioned that, the sensing range for the dynamic strain sensing and hydrogen sensing is not very long (tens of meters); however, it turns out to be actually limited by the length of the fibers which are available in the lab rather than other fundamental limits such as SNR or coherence length of the laser.

8 Conclusions and Perspectives

With the development of automation and the advent of the artificial intelligence era, sensors of all kinds are required to perceive the environment with unprecedented sensitivities. On top of the numerous merits of optical fibers, such as low cost, abundant raw material, and immunity to electromagnetic interferences, distributed optical fiber sensors enable to probe their environment over long distances by using a single interrogation system. Frequency-scanned ϕ -OTDR provides quantitative measurements with high sensitivity thus has the potential to be used in many different industrial and field applications.

8.1 Main contributions

This thesis focuses on distributed optical fiber sensing based on frequency-scanned ϕ -OTDR, which enables to perform quantitative measurements on different measurands such as temperature and strain by scanning the frequency of the light sent into the sensing fiber. The coherent process involved in the interrogation using frequency-scanned ϕ -OTDR results in a jagged pattern, an unconventional signal waveform that requires proper post-processing. Of outermost importance, measurement errors have been thoroughly investigated in terms of experimental parameters, in order to draw the performances optimization guidelines of the system. Various sensing schemes based on frequency-scanned ϕ -OTDR using different fibers have been proposed, demonstrating the versatility of this technique. The performance of all the sensing demonstrations is summarized in Table 8.1.

Frequency shift estimation errors

- A thorough analysis on the probability of large errors in the frequency shift estimation using cross correlation in frequency-scanned ϕ -OTDR has been performed for the first time to the best of our knowledge. An analytical model has been proposed to describe the probability of large errors and the theoretical results have been compared with experimental results. The study suggests that large errors on the frequency shift

estimation of ϕ -OTDR unavoidably occur when using cross correlation techniques due to purely stochastic reasons related to the limited spectral window of analysis, even in conditions of perfect signal-to-noise ratio, which turns out to be a critical limitation since the large error occurrences are essentially inevitable. It should be noted that large errors do not only occur in correlation-based ϕ -OTDR. A similar model can be developed for any Rayleigh-based distributed sensor employing frequency shift estimation of the backscattered spectra based on cross correlation, such as OFDR, thus the model can be adapted for the estimation of its large errors probability too.

- Moreover, we have proposed a method to circumvent these large errors, employing a least mean squares estimation of the similarity between the reference and measurement spectra. Using this method, the stochastic nature of large errors can be totally suppressed and the measurement becomes only limited by noise. The maximum measurable range can be safely enlarged while keeping a limited spectral scanning range for running acquisitions. As a result, a ϕ -OTDR instrumental system with a spatial resolution of 5 cm and a sensing range of about 860 m is demonstrated. The system exhibits a dynamic range on temperature change of about 36.5 dB (more than 100 °C) and is virtually immune to large statistical errors.

Distributed pressure sensing

Distributed pressure sensing based on frequency-scanned ϕ -OTDR has been proposed for the first time to the best of our knowledge, by measuring the birefringence change of different fibers subject to external pressure. The interrogation procedure has been experimentally demonstrated using two different types of micro-structured fibers.

- Photonic crystal fibers (PCFs) are used for distributed pressure sensing demonstration. The experimental results show the high sensitivity of these fibers, reaching -95.4 MHz/bar and -219 MHz/bar with a high spatial resolution of only 5 cm. The birefringence of the PCFs is barely sensitive to temperature variations, thus they are promising candidates for applications where zero temperature sensitivity is required.
- Distributed pressure sensing has also been demonstrated based on frequency-scanned ϕ -OTDR using side air holes fiber. Thanks to the low splicing and propagation loss of the fiber, a *record* long sensing range (~ 720m) has been achieved with high pressure sensitivity (~ 169 MHz/bar). The temperature/strain and pressure cross sensitivity has been addressed and the discrimination between temperature/strain and pressure has been demonstrated. In addition, the sensing range limitation has been investigated by estimation of the crosstalk between polarizations for the first time to the best of our knowledge, which we believe is a prerequisite to estimate the sensing performances of the system.

Sensing quantity	Fiber	Distance	Spatial resolution	Sensitivity	Accuracy
Temperature	SMF	860 m	5 cm	1.3 GHz/K	0.026 K
Pressure	"Butterfly" PCF 1	20 m	5 cm	-219 MHz/bar	0.22 bar
	"Butterfly" PCF 2	40 m	5 cm	-95.4 MHz/bar	0.59 bar
	Side air hole fiber	720 m	5 cm	159 MHz/bar	0.49 bar
Dynamic Strain	Backscattering-enhanced fiber	55 m	20 cm	150 MHz/ $\mu\epsilon$	0.7 ne/ $\sqrt{\text{Hz}}$
Hydrogen	Palladium foiled fiber	5 m	5 cm	-	-

Table 8.1 – Summary of demonstrated sensing performance

Distributed and dynamic strain sensing

Distributed and dynamic strain sensing has been demonstrated, utilizing a radio frequency (RF) pulsing scheme and backscattering-enhanced fiber. The RF pulsing scheme enables generating short pulses with high extinction ratio exhibiting large linear frequency scan with zero switching latency. At the same time, the Rayleigh enhanced fiber provides 10 dB stronger backscattering intensity with negligible added loss, which eliminates the need for averaging. As a result, a distributed and dynamic strain sensing system with *record* high spatial resolution in direct-detection mode is achieved. What is more, the proposed least mean square scheme has been adapted to the system, thus enabling a fairly large strain ($\leq 80\mu\epsilon$) to be measured. The high spatial resolution, relatively fast response and large measurable strain range, promotes this system to be a good candidate to measure cracks in health monitoring structure.

Distributed hydrogen sensing

A distributed hydrogen alarm system has been proposed and demonstrated, using a novel coating configuration with fibers bonding to palladium (Pd) foils. The fiber is dedicately designed for hydrogen sensing hence displays a larger cross-sectional area than conventional single-mode fibers, thus showing ultra-high hydrogen sensitivity. As a result, by measuring the strain change induced by the absorption of hydrogen by the Pd foils, an ultra-high sensitive distributed hydrogen sensing with 5 cm spatial resolution is demonstrated. Similar to the case of dynamic strain sensing, the least mean square algorithm has been adapted to the system, thus enabling large strain measurements.

8.2 Future work

In this thesis, frequency-scanned ϕ -OTDR has been investigated in great depth and its potential for diverse applications on different measurands using various fibers has been shown. The capability of long-distance sensing with high spatial resolution has been demonstrated. There is always much room for performance improvement in terms of sensing distance, spatial resolution, sensitivity, etc. However, there are more specific aspects that require to be addressed and studied in priority in the future, including:

- The measurement errors (frequency shift uncertainty) of the system as a function of the frequency scanning range, frequency scanning step, signal bandwidth and signal-to-noise ratio should be studied, which would enable defining proper guidelines in order to match the system parameters to well-defined sensing requirements.
- In distributed pressure sensing, the issue of light coupling between the two polarization modes of the fiber due to the bending and twisting is worth being addressed, as to assess its impact on real-world applications. As a step forward towards simplification, an inter-

rogation procedure which would allow to directly obtain the Rayleigh backscattering spectra on both polarization axes using depolarized light or a linearly polarized light with an angle of 45° with respect to both principal polarization axes of the fiber is also to be considered.

- In distributed hydrogen sensing, thorough studies need to be conducted to investigate the response time of different hydrogen concentrations. The palladium foiled fiber shows high sensitivity but the response is relatively slow. Besides, it is difficult to manufacture the Pd foiled fiber with long distance and high uniformity. The reported Palladium-coated fiber [164] can be implemented in the system for faster response with long distance.
- Recently, hollow-core fibers (HCFs) have rapidly drawn increasing attention, in particular due to the fact that their propagation loss (0.28 dB/km) has been reduced to be close to standard single mode fiber [165]. Stimulated Brillouin scattering has been recently demonstrated to be strongly enhanced when pressurizing the gas in HCFs, which also shows interesting and promising features such as zero strain-sensitivity [166]. Similarly, Rayleigh scattering in these fibers with different gas molecules and different pressure levels ought to be investigated and exploited for distributed sensing.

Bibliography

- [1] X. Bao and L. Chen, "Recent Progress in Distributed Fiber Optic Sensors", *"Sensors"*, vol. 12, no. 7, Jul. 2012.
- [2] A. Barrias, J. R. Casas, and S. Villalba, "A review of methods for fibre-optic distributed chemical sensing", *"Sensors"*, vol. 16, no. 5, May 2016.
- [3] A. Masoudi and T. P. Newson, "Contributed review: distributed optical fibre dynamic strain sensing", *"Review of Scientific Instruments"*, vol. 87, no. 1, 2016.
- [4] M. Niklès, B. H. Vogel, F. Briffod, S. Grosswig, F. Sauser, S. Luebbecke, A. Bals, and T. Pfeiffer, "Leakage detection using fiber optics distributed temperature monitoring", *Smart Structures and Materials 2004: Smart Sensor Technology and Measurement Systems*, International Society for Optics and Photonics, vol. 5384, 2004, pp. 18–25.
- [5] C. V. Raman and K. S. Krishnan, "A new type of secondary radiation", *"Nature"*, vol. 121, no. 3048, 1928.
- [6] L. Thevenaz, *Advanced fiber optics: concepts and technology*. EPFL press, 2011.
- [7] M. A. Farahani and T. Gogolla, "Spontaneous raman scattering in optical fibers with modulated probe light for distributed temperature raman remote sensing", *"Journal of Lightwave Technology"*, vol. 17, no. 8, Aug. 1999.
- [8] J. Dakin, D. Pratt, G. Bibby, and J. Ross, "Distributed optical fibre raman temperature sensor using a semiconductor light source and detector", *"Electronics letters"*, vol. 21, no. 13, 1985.
- [9] G. A. Brown, A. Hartog, *et al.*, "Optical fiber sensors in upstream oil & gas", *"Journal of petroleum technology"*, vol. 54, no. 11, 2002.
- [10] S. W. Tyler, J. S. Selker, M. B. Hausner, C. E. Hatch, T. Torgersen, C. E. Thodal, and S. G. Schladow, "Environmental temperature sensing using raman spectra DTS fiber-optic methods", *"Water Resources Research"*, vol. 45, no. 4, 2009.
- [11] A. Ukil, H. Braendle, and P. Krippner, "Distributed temperature sensing: review of technology and applications", *"IEEE Sensors Journal"*, vol. 12, no. 5, 2012.

-
- [12] A. F. Fernandez, P. Rodeghiero, B. Brichard, F. Berghmans, A. H. Hartog, P. Hughes, K. Williams, and A. Leach, "Radiation-tolerant raman distributed temperature monitoring system for large nuclear infrastructures", *"IEEE transactions on nuclear science"*, vol. 52, no. 6, 2005.
- [13] G. W. Bibby, Temperature measurement, US Patent 4,859,065, 1989.
- [14] J. Dakin, D. Pratt, G. Bibby, and J. Ross, "Temperature distribution measurement using raman ratio thermometry", *Fiber Optic and Laser Sensors III*, International Society for Optics and Photonics, vol. 566, 1986, pp. 249–256.
- [15] DTSX200 distributed temperature sensor DTS, 2013.
- [16] LIOS_DE.TECT_linear heat detection_LHD3 series, 2019.
- [17] R. W. Boyd, Nonlinear optics. Academic press, 2007.
- [18] K. Shimizu, T. Horiguchi, Y. Koyamada, and T. Kurashima, "Coherent self-heterodyne detection of spontaneously brillouin-scattered light waves in a single-mode fiber", *"Optics letters"*, vol. 18, no. 3, 1993.
- [19] Z. Wu, F. Wu, L. Niu, and Z. Li, "Distributed fiber optical strain sensor based on BOFDR", *2nd International Symposium on Advanced Optical Manufacturing and Testing Technologies: Optical Test and Measurement Technology and Equipment*, International Society for Optics and Photonics, vol. 6150, 2006, 61501W.
- [20] A. Minardo, R. Bernini, R. Ruiz-Lombera, J. Mirapeix, J. M. Lopez-Higuera, and L. Zeni, "Proposal of brillouin optical frequency-domain reflectometry (BOFDR)", *"Optics express"*, vol. 24, no. 26, 2016.
- [21] H. Ohno, H. Naruse, M. Kihara, and A. Shimada, "Industrial applications of the BOTDR optical fiber strain sensor", *"Optical fiber technology"*, vol. 7, no. 1, 2001.
- [22] C. A. Galindez-Jamioy and J. M. Lopez-Higuera, "Brillouin distributed fiber sensors: an overview and applications", *"Journal of Sensors"*, vol. 2012, 2012.
- [23] D. Cotter, "Observation of stimulated brillouin scattering in low-loss silica fibre at 1.3 μm ", *"Electronics Letters"*, vol. 18, no. 12, 1982.
- [24] A. Motil, A. Bergman, and M. Tur, "State of the art of brillouin fiber-optic distributed sensing", *"Optics & Laser Technology"*, vol. 78, 2016.
- [25] F. Gyger, E. Rochat, S. Chin, M. Niklès, and L. Thévenaz, "Extending the sensing range of brillouin optical time-domain analysis up to 325 km combining four optical repeaters", *23rd International Conference on Optical Fibre Sensors*, International Society for Optics and Photonics, vol. 9157, 2014, 91576Q.
- [26] Y. Fu, Z. Wang, R. Zhu, N. Xue, J. Jiang, C. Lu, B. Zhang, L. Yang, D. Atubga, and Y. Rao, "Ultra-long-distance hybrid BOTDA/ ϕ -OTDR", *"Sensors"*, vol. 18, no. 4, 2018.
- [27] W. Li, X. Bao, Y. Li, and L. Chen, "Differential pulse-width pair botda for high spatial resolution sensing", *"Optics express"*, vol. 16, no. 26, 2008.

BIBLIOGRAPHY

- [28] M. A. Soto, M. Taki, G. Bolognini, and F. Di Pasquale, "Optimization of a dpp-botda sensor with 25 cm spatial resolution over 60 km standard single-mode fiber using simplex codes and optical pre-amplification", *"Optics Express"*, vol. 20, no. 7, 2012.
- [29] S. Wang, Z. Yang, S. Zaslowski, and L. Thévenaz, "Short spatial resolution retrieval from a long pulse brillouin optical time-domain analysis trace", *"Optics Letters"*, vol. 45, no. 15, 2020.
- [30] I. L. Fabelinskii, *Molecular scattering of light*. Springer Science & Business Media, 2012.
- [31] A. Rogers, *Essentials of Optoelectronics with applications*. CRC Press, 1997, vol. 4.
- [32] M. Barnoski and S. Jensen, "Fiber waveguides: a novel technique for investigating attenuation characteristics", *"Applied optics"*, vol. 15, no. 9, 1976.
- [33] L. Palmieri and L. Schenato, "Distributed optical fiber sensing based on Rayleigh scattering", *"The Open Optics Journal"*, vol. 7, no. 1, 2013.
- [34] L. Zhang, L. D. Costa, Z. Yang, M. A. Soto, M. González-Herráez, and L. Thévenaz, "Analysis and Reduction of Large Errors in Rayleigh-Based Distributed Sensor", *"Journal of Lightwave Technology"*, vol. 37, no. 18, Sep. 2019.
- [35] R. Posey, G. Johnson, and S. Vohra, "Strain sensing based on coherent Rayleigh scattering in an optical fibre", *"Electronics Letters"*, vol. 36, no. 20, 2000.
- [36] T. Chen, Q. Wang, R. Chen, B. Zhang, C. Jewart, K. P. Chen, M. Maklad, and P. R. Swinehart, "Distributed high-temperature pressure sensing using air-hole microstructural fibers", *"Optics Letters"*, vol. 37, no. 6, Mar. 2012.
- [37] X. Liu, B. Jin, Q. Bai, Y. Wang, D. Wang, and Y. Wang, "Distributed fiber-optic sensors for vibration detection", *"Sensors"*, vol. 16, no. 8, 2016.
- [38] A. J. Rogers, "Polarization-optical time domain reflectometry: a technique for the measurement of field distributions", *"Applied optics"*, vol. 20, no. 6, 1981.
- [39] Z. Zhang and X. Bao, "Distributed optical fiber vibration sensor based on spectrum analysis of polarization-OTDR system", *"Optics express"*, vol. 16, no. 14, 2008.
- [40] H. F. Taylor and C. E. Lee, *Apparatus and method for fiber optic intrusion sensing*, US Patent 5,194,847, 1993.
- [41] W. Eickhoff and R. Ulrich, "Optical frequency domain reflectometry in single-mode fiber", *"Applied Physics Letters"*, vol. 39, no. 9, 1981.
- [42] Z. Ding, X. S. Yao, T. Liu, Y. Du, K. Liu, Q. Han, Z. Meng, and H. Chen, "Long-range vibration sensor based on correlation analysis of optical frequency-domain reflectometry signals", *"Optics express"*, vol. 20, no. 27, 2012.
- [43] J. Von Der Weid, R. Passy, G. Mussi, and N. Gisin, "On the characterization of optical fiber network components with optical frequency domain reflectometry", *"Journal of Lightwave Technology"*, vol. 15, no. 7, 1997.

-
- [44] D. Zhao, D. Pustakhod, K. Williams, and X. Leijtens, "High resolution optical frequency domain reflectometry for analyzing intra-chip reflections", *"IEEE Photonics Technology Letters"*, vol. 29, no. 16, 2017.
- [45] Q. Liu, X. Fan, and Z. He, "Time-gated digital optical frequency domain reflectometry with 1.6-m spatial resolution over entire 110-km range", *"Optics Express"*, vol. 23, no. 20, 2015.
- [46] M. Froggatt and J. Moore, "High-spatial-resolution distributed strain measurement in optical fiber with Rayleigh scatter", *"Applied Optics"*, vol. 37, no. 10, 1998.
- [47] D. K. Gifford, B. J. Soller, M. S. Wolfe, and M. E. Froggatt, "Distributed fiber-optic temperature sensing using Rayleigh backscatter", *2005 31st European Conference on Optical Communication, ECOC 2005*, IET, vol. 3, 2005, pp. 511–512.
- [48] D. Arbel and A. Eyal, "Dynamic optical frequency domain reflectometry", *"Optics express"*, vol. 22, no. 8, 2014.
- [49] L. Shiloh and A. Eyal, "Sinusoidal frequency scan OFDR with fast processing algorithm for distributed acoustic sensing", *"Optics express"*, vol. 25, no. 16, 2017.
- [50] R. C. Youngquist, S. Carr, and D. E. Davies, "Optical coherence-domain reflectometry: a new optical evaluation technique", *"Optics letters"*, vol. 12, no. 3, 1987.
- [51] D. Huang, E. A. Swanson, C. P. Lin, J. S. Schuman, W. G. Stinson, W. Chang, M. R. Hee, T. Flotte, K. Gregory, C. A. Puliafito, *et al.*, "Optical coherence tomography", *"Science"*, vol. 254, no. 5035, 1991.
- [52] K. Hotate and O. Kamatani, "Reflectometry by means of optical-coherence modulation", *"Electronics Letters"*, vol. 25, no. 22, 1989.
- [53] T. Okugawa and K. Hotate, "Synthesis of arbitrary shapes of optical coherence function using phase modulation", *"IEEE Photonics Technology Letters"*, vol. 8, no. 12, 1996.
- [54] T. Saida and K. Hotate, "Distributed fiber-optic stress sensor by synthesis of the optical coherence function", *"IEEE Photonics Technology Letters"*, vol. 9, no. 4, 1997.
- [55] K. Hotate and Z. He, "Synthesis of optical-coherence function and its applications in distributed and multiplexed optical sensing", *"Journal of Lightwave Technology"*, vol. 24, no. 7, 2006.
- [56] K. Hotate and M. Tanaka, "Distributed fiber Brillouin strain sensing with 1-cm spatial resolution by correlation-based continuous-wave technique", *"IEEE Photonics Technology Letters"*, vol. 14, no. 2, 2002.
- [57] Y. Mizuno, W. Zou, Z. He, and K. Hotate, "Proposal of Brillouin optical correlation-domain reflectometry (BOCDR)", *"Optics express"*, vol. 16, no. 16, 2008.
- [58] Y. Rao, J. Luo, Z. Ran, J. Yue, X. Luo, and Z. Zhou, "Long-distance fiber-optic ϕ -OTDR intrusion sensing system", *20th international conference on optical fibre sensors*, International Society for Optics and Photonics, vol. 7503, 2009, 75031O.

BIBLIOGRAPHY

- [59] F. Peng, H. Wu, X.-H. Jia, Y.-J. Rao, Z.-N. Wang, and Z.-P. Peng, "Ultra-long high-sensitivity ϕ -OTDR for high spatial resolution intrusion detection of pipelines", *"Optics express"*, vol. 22, no. 11, 2014.
- [60] Z. Wang, J. Zeng, J. Li, M. Fan, H. Wu, F. Peng, L. Zhang, Y. Zhou, and Y. Rao, "Ultra-long phase-sensitive OTDR with hybrid distributed amplification", *"Optics letters"*, vol. 39, no. 20, 2014.
- [61] H. F. Martins, S. Martin-Lopez, P. Corredera, J. D. Ania-Castañon, O. Frazão, and M. Gonzalez-Herraez, "Distributed vibration sensing over 125 km with enhanced SNR using phi-OTDR over a URFL cavity", *"Journal of Lightwave Technology"*, vol. 33, no. 12, 2015.
- [62] T. Zhu, X. Xiao, Q. He, and D. Diao, "Enhancement of SNR and spatial resolution in φ -OTDR system by using two-dimensional edge detection method", *"Journal of Lightwave Technology"*, vol. 31, no. 17, 2013.
- [63] Y. Lu, T. Zhu, L. Chen, and X. Bao, "Distributed vibration sensor based on coherent detection of phase-otdr", *"Journal of lightwave Technology"*, vol. 28, no. 22, 2010.
- [64] F. Zhu, X. Zhang, L. Xia, Z. Guo, and Y. Zhang, "Active compensation method for light source frequency drifting in ϕ -OTDR sensing system", *"IEEE Photonics Technology Letters"*, vol. 27, no. 24, 2015.
- [65] J. Zhang, H. Wu, H. Zheng, J. Huang, G. Yin, T. Zhu, F. Qiu, X. Huang, D. Qu, and Y. Bai, "80 km fading free phase-sensitive reflectometry based on multi-carrier nlfm pulse without distributed amplification", *"Journal of Lightwave Technology"*, vol. 37, no. 18, 2019.
- [66] T. Zhu, Q. He, X. Xiao, and X. Bao, "Modulated pulses based distributed vibration sensing with high frequency response and spatial resolution", *"Optics express"*, vol. 21, no. 3, 2013.
- [67] Z. Wang, B. Zhang, J. Xiong, Y. Fu, S. Lin, J. Jiang, Y. Chen, Y. Wu, Q. Meng, and Y. Rao, "Distributed acoustic sensing based on pulse-coding phase-sensitive OTDR", *"IEEE Internet of Things Journal"*, vol. 6, no. 4, 2018.
- [68] Z. Wang, J. Zeng, J. Li, F. Peng, L. Zhang, Y. Zhou, H. Wu, and Y. Rao, "175km phase-sensitive OTDR with hybrid distributed amplification", *23rd international conference on optical fibre sensors*, International Society for Optics and Photonics, vol. 9157, 2014, p. 9157D5.
- [69] J. Pastor-Graells, L. R. Cortés, H. F. Martins, M. R. Fernández-Ruiz, J. Azaña, S. Martin-Lopez, and M. Gonzalez-Herraez, "20 dB SNR enhancement in phase-sensitive OTDR using pulse stretching and recompression", *2017 25th Optical Fiber Sensors Conference (OFS)*, IEEE, 2017, pp. 1–4.
- [70] G. Yang, X. Fan, Q. Liu, and Z. He, "Frequency response enhancement of direct-detection phase-sensitive otdr by using frequency division multiplexing", *"Journal of Lightwave Technology"*, vol. 36, no. 4, 2018.

-
- [71] Y. Koyamada, M. Imahama, K. Kubota, and K. Hogari, "Fiber-Optic Distributed Strain and Temperature Sensing With Very High Measurand Resolution Over Long Range Using Coherent OTDR", *"Journal of Lightwave Technology"*, vol. 27, no. 9, May 2009.
- [72] X. Lu, "Coherent Rayleigh time domain reflectometry", EPFL, Tech. Rep., 2016.
- [73] J. W. Goodman, *Speckle phenomena in optics: theory and applications*. Roberts and Company Publishers, 2007.
- [74] P. Healey, "Fading in heterodyne OTDR", *"Electronics letters"*, vol. 20, no. 1, 1984.
- [75] H. P, "Statistics of Rayleigh backscatter from a single-mode optical fibre", *"Electronics Letters"*, vol. 21, no. 6, 1985.
- [76] H. Izumita, S.-I. Furukawa, Y. Koyamada, and I. Sankawa, "Fading noise reduction in coherent OTDR", *"IEEE Photonics Technology Letters"*, vol. 4, no. 2, 1992.
- [77] L. Costa, H. F. Martins, S. Martín-López, M. R. Fernández-Ruiz, and M. González-Herráez, "Fully distributed optical fiber strain sensor with 10-12 $\epsilon/\sqrt{\text{Hz}}$ sensitivity", *"Journal of Lightwave Technology"*, vol. 37, no. 18, Sep. 2019.
- [78] Y. Wang, Q. Liu, D. Chen, H. Li, and Z. He, "Distributed fiber-optic dynamic-strain sensor with sub-meter spatial resolution and single-shot measurement", *"IEEE Photonics Journal"*, vol. 11, no. 6, Dec. 2019.
- [79] A. Masoudi, M. Belal, and T. P. Newson, "A distributed optical fibre dynamic strain sensor based on phase-OTDR", *"Meas. Sci. Technol."*, vol. 24, no. 8, Jul. 2013.
- [80] G. Fang, T. Xu, S. Feng, and F. Li, "Phase-sensitive optical time domain reflectometer based on phase-generated carrier algorithm", *"Journal of Lightwave Technology"*, vol. 33, no. 13, Jul. 2015.
- [81] J. Xiong, Z. Wang, Y. Wu, and Y. Rao, "Single-shot COTDR using sub-chirped-pulse extraction algorithm for distributed strain sensing", *"Journal of Lightwave Technology"*, 2020.
- [82] Z. Wang, L. Zhang, S. Wang, N. Xue, F. Peng, M. Fan, W. Sun, X. Qian, J. Rao, and Y. Rao, "Coherent ϕ -OTDR based on I/Q demodulation and homodyne detection", *"Optics Express"*, vol. 24, no. 2, Jan. 2016.
- [83] J. J. Mompó, L. Shiloh, N. Arbel, N. Levanon, A. Loayssa, and A. Eyal, "Distributed dynamic strain sensing via perfect periodic coherent codes and a polarization diversity receiver", *"Journal of Lightwave Technology"*, vol. 37, no. 18, Sep. 2019.
- [84] A. Alekseev, V. Vdovenko, B. Gorshkov, V. Potapov, and D. Simikin, "A phase-sensitive optical time-domain reflectometer with dual-pulse phase modulated probe signal", *"Laser Physics"*, vol. 24, no. 11, 2014.
- [85] C. Wang, C. Wang, Y. Shang, X. Liu, and G. Peng, "Distributed acoustic mapping based on interferometry of phase optical time-domain reflectometry", *"Optics Communications"*, vol. 346, 2015.

BIBLIOGRAPHY

- [86] R. G. Priest, "Analysis of fiber interferometer utilizing 3 x 3 fiber coupler", *"IEEE Transactions on Microwave Theory and Techniques"*, vol. 30, no. 10, 1982.
- [87] D. S. Ly Gagnon, S. Tsukamoto, K. Katoh, and K. Kikuchi, "Coherent detection of optical quadrature phase-shift keying signals with carrier phase estimation", *"Journal of lightwave technology"*, vol. 24, no. 1, 2006.
- [88] J. Jiang, Z. Wang, Z. Wang, Y. Wu, S. Lin, J. Xiong, Y. Chen, and Y. Rao, "Coherent kramers-kronig receiver for ϕ -OTDR", *"Journal of Lightwave Technology"*, vol. 37, no. 18, 2019.
- [89] G. Yang, X. Fan, S. Wang, B. Wang, Q. Liu, and Z. He, "Long-range distributed vibration sensing based on phase extraction from phase-sensitive OTDR", *"IEEE Photonics Journal"*, vol. 8, no. 3, 2016.
- [90] H. Gabai and A. Eyal, "SNR characterization in distributed acoustic sensing", *Sixth European Workshop on Optical Fibre Sensors*, International Society for Optics and Photonics, vol. 9916, 2016, 99162W.
- [91] Z. Sha, H. Feng, and Z. Zeng, "Phase demodulation method in phase-sensitive OTDR without coherent detection", *"Optics Express"*, vol. 25, no. 5, 2017.
- [92] X. He, S. Xie, F. Liu, S. Cao, L. Gu, X. Zheng, and M. Zhang, "Multi-event waveform-retrieved distributed optical fiber acoustic sensor using dual-pulse heterodyne phase-sensitive otdr", *"Optics letters"*, vol. 42, no. 3, 2017.
- [93] J. Pastor-Graells, H. F. Martins, A. Garcia-Ruiz, S. Martin-Lopez, and M. Gonzalez-Herraez, "Single-shot distributed temperature and strain tracking using direct detection phase-sensitive OTDR with chirped pulses", *"Optics Express"*, vol. 24, no. 12, Jun. 2016.
- [94] G. B. Hocker, "Fiber-optic sensing of pressure and temperature", *"Apply Optics"*, vol. 18, no. 9, May 1979.
- [95] M. Okaji, N. Yamada, K. Nara, and H. Kato, "Laser interferometric dilatometer at low temperatures: application to fused silica srm 739", *"Cryogenics"*, vol. 35, no. 12, 1995.
- [96] D. B. Leviton and B. J. Frey, "Temperature-dependent absolute refractive index measurements of synthetic fused silica", *Optomechanical Technologies for Astronomy*, International Society for Optics and Photonics, vol. 6273, 2006, 62732K.
- [97] C. D. Butter and G. Hocker, "Fiber optics strain gauge", *"Applied optics"*, vol. 17, no. 18, 1978.
- [98] Y. Zhang, D. Feng, Z. Liu, Z. Guo, X. Dong, K. Chiang, and B. C. Chu, "High-sensitivity pressure sensor using a shielded polymer-coated fiber bragg grating", *"IEEE Photonics Technology Letters"*, vol. 13, no. 6, 2001.
- [99] Y. Liu, Z. Guo, Y. Zhang, K. S. Chiang, and X. Dong, "Simultaneous pressure and temperature measurement with polymer-coated fibre bragg grating", *"Electronics letters"*, vol. 36, no. 6, 2000.

- [100] F. C. Fávero, S. M. Quintero, C. Martelli, A. Braga, V. V. Silva, I. Carvalho, R. W. Llerena, and L. C. Valente, "Hydrostatic pressure sensing with high birefringence photonic crystal fibers", *"Sensors"*, vol. 10, no. 11, 2010.
- [101] H. M. Xie, K. Okamoto, P. Dabkiewicz, and R. Ulrich, "Side-hole fiber for fiber-optic pressure sensing", *"Optics Letters"*, vol. 11, no. 5, May 1986.
- [102] M. Ren, D.-P. Zhou, L. Chen, and X. Bao, "Influence of finite extinction ratio on performance of phase-sensitive optical time-domain reflectometry", *"Optics express"*, vol. 24, no. 12, 2016.
- [103] H. F. Martins, S. Martin-Lopez, P. Corredera, P. Salgado, O. Frazão, and M. González-Herráez, "Modulation instability-induced fading in phase-sensitive optical time-domain reflectometry", *"Optics letters"*, vol. 38, no. 6, 2013.
- [104] P. S. Westbrook, K. S. Feder, R. M. Ortiz, T. Kremp, E. M. Monberg, H. Wu, D. A. Simoff, and S. Shenk, "Kilometer length, low loss enhanced back scattering fiber for distributed sensing", *2017 25th Optical Fiber Sensors Conference (OFS)*, 2017, pp. 1–5.
- [105] J. Urricelqui, A. Zornoza, M. Sagues, and A. Loayssa, "Dynamic BOTDA measurements based on Brillouin phase-shift and RF demodulation", *"Optics Express"*, vol. 20, no. 24, Nov. 2012.
- [106] A. K. Sang, M. E. Froggatt, D. K. Gifford, S. T. Kreger, and B. D. Dickerson, "One centimeter spatial resolution temperature measurements in a nuclear reactor using Rayleigh scatter in optical fiber", *"IEEE Sensors Journal"*, vol. 8, no. 7, 2008.
- [107] K. Feng, J. Cui, D. Jiang, H. Dang, Y. Jin, X. Sun, Y. Niu, and J. Tan, "Improvement of the strain measurable range of an OFDR based on local similar characteristics of a Rayleigh scattering spectrum", *"Optics Letters"*, vol. 43, no. 14, 2018.
- [108] L. Zhang, Z. Yang, F. Gyger, M. A. Soto, and L. Thévenaz, "Rayleigh-based distributed optical fiber sensing using least mean square similarity", *Optical Fiber Sensors*, Optical Society of America, 2018, ThE29.
- [109] S. Liehr, S. Münzenberger, and K. Krebber, "Wavelength-scanning coherent OTDR for dynamic high strain resolution sensing", *"Optics express"*, vol. 26, no. 8, 2018.
- [110] G. Jacovitti and G. Scarano, "Discrete time techniques for time delay estimation", *"IEEE Transactions on signal processing"*, vol. 41, no. 2, 1993.
- [111] J. Ianniello, "Time delay estimation via cross-correlation in the presence of large estimation errors", *"IEEE Transactions on Acoustics, Speech, and Signal Processing"*, vol. 30, no. 6, 1982.
- [112] I. J., "Large and small error performance limits for multipath time delay estimation", *"IEEE Transactions on Acoustics, Speech, and Signal Processing"*, vol. 34, no. 2, 1986.
- [113] X. Lu, P. J. Thomas, and J. O. Hellevang, "A Review of Methods for Fibre-Optic Distributed Chemical Sensing", *"Sensors"*, vol. 19, no. 13, Jan. 2019.

BIBLIOGRAPHY

- [114] R. Magalhães, A. Garcia-Ruiz, H. F. Martins, J. Pereira, W. Margulis, S. Martin-Lopez, and M. Gonzalez-Herraez, “Fiber-based distributed bolometry”, *“Optics express”*, vol. 27, no. 4, 2019.
- [115] S. Liehr, M. Breithaupt, and K. Krebber, “Distributed Humidity Sensing in PMMA Optical Fibers at 500 nm and 650 nm Wavelengths”, *“Sensors”*, vol. 17, no. 4, Apr. 2017.
- [116] Y. H. Kim, H. Kwon, J. Kim, and K. Y. Song, “Distributed measurement of hydrostatic pressure based on Brillouin dynamic grating in polarization maintaining fibers”, *“Optics Express”*, vol. 24, no. 19, Sep. 2016.
- [117] L. Teng, H. Zhang, Y. Dong, D. Zhou, T. Jiang, W. Gao, Z. Lu, L. Chen, and X. Bao, “Temperature-compensated distributed hydrostatic pressure sensor with a thin-diameter polarization-maintaining photonic crystal fiber based on Brillouin dynamic gratings”, *“Optics Letters”*, vol. 41, no. 18, Sep. 2016.
- [118] L. Schenato, A. Pasuto, A. Galtarossa, and L. Palmieri, “An optical fiber distributed pressure sensing cable with pa-sensitivity and enhanced spatial resolution”, *“IEEE Sensors Journal”*, vol. 20, no. 11, 2020.
- [119] L. Schenato, A. Galtarossa, A. Pasuto, and L. Palmieri, “Distributed optical fiber pressure sensors”, *“Optical Fiber Technology”*, vol. 58, 2020.
- [120] M. A. Soto, X. Lu, H. F. Martins, M. Gonzalez-Herraez, and L. Thévenaz, “Distributed phase birefringence measurements based on polarization correlation in phase-sensitive optical time-domain reflectometers”, *“Optics Express”*, vol. 23, no. 19, 2015.
- [121] J. Knight, T. Birks, P. S. J. Russell, and D. Atkin, “All-silica single-mode optical fiber with photonic crystal cladding”, *“Optics letters”*, vol. 21, no. 19, 1996.
- [122] P. Russell, “Photonic crystal fibers”, *“Science”*, vol. 299, no. 5605, 2003.
- [123] J. M. Dudley, G. Genty, and S. Coen, “Supercontinuum generation in photonic crystal fiber”, *“Reviews of modern physics”*, vol. 78, no. 4, 2006.
- [124] L. Rindorf, J. B. Jensen, M. Dufva, L. H. Pedersen, P. E. Høiby, and O. Bang, “Photonic crystal fiber long-period gratings for biochemical sensing”, *“Optics Express”*, vol. 14, no. 18, 2006.
- [125] A. M. Pinto and M. Lopez-Amo, “Photonic crystal fibers for sensing applications”, *“Journal of Sensors”*, vol. 2012, 2012.
- [126] A. Ortigosa-Blanch, J. Knight, W. Wadsworth, J. Arriaga, B. Mangan, T. Birks, and P. S. J. Russell, “Highly birefringent photonic crystal fibers”, *“Optics letters”*, vol. 25, no. 18, 2000.
- [127] T. P. Hansen, J. Broeng, S. E. Libori, E. Knudsen, A. Bjarklev, J. R. Jensen, and H. Simonsen, “Highly birefringent index-guiding photonic crystal fibers”, *“IEEE Photonics Technology Letters”*, vol. 13, no. 6, 2001.
- [128] M. Szpulak, W. Urbanczyk, T. Martynkien, J. Wojcik, and W. J. Bock, “Temperature sensitivity of photonic crystal holey fibers”, *Optical Fibers and Their Applications VIII*, International Society for Optics and Photonics, vol. 5028, 2003, pp. 108–114.

- [129] M. Szpulak, T. Martynkien, and W. Urbanczyk, "Effects of hydrostatic pressure on phase and group modal birefringence in microstructured holey fibers", *"Applied optics"*, vol. 43, no. 24, 2004.
- [130] Y. Liu, B. Rahman, and K. T. Grattan, "Thermal-stress-induced birefringence in bow-tie optical fibers", *"Applied optics"*, vol. 33, no. 24, 1994.
- [131] T. Hosaka, K. Okamoto, T. Miya, Y. Sasaki, and T. Edauro, "Low-loss single polarisation fibres with asymmetrical strain birefringence", *"Electronics Letters"*, vol. 17, no. 15, 1981.
- [132] T. Martynkien, G. Statkiewicz-Barabach, J. Olszewski, J. Wojcik, P. Mergo, T. Geernaert, C. Sonnenfeld, A. Anuszkiewicz, M. K. Szczurowski, K. Tarnowski, *et al.*, "Highly birefringent microstructured fibers with enhanced sensitivity to hydrostatic pressure", *"Optics Express"*, vol. 18, no. 14, 2010.
- [133] S. Sulejmani, C. Sonnenfeld, T. Geernaert, P. Mergo, M. Makara, K. Poturaj, K. Skorupski, T. Martynkien, G. Statkiewicz-Barabach, J. Olszewski, *et al.*, "Control over the pressure sensitivity of bragg grating-based sensors in highly birefringent microstructured optical fibers", *"IEEE Photonics Technology Letters"*, vol. 24, no. 6, 2012.
- [134] J. Clowes, S. Syngellakis, and M. Zervas, "Pressure sensitivity of side-hole optical fiber sensors", *"IEEE Photonics Technology Letters"*, vol. 10, no. 6, 1998.
- [135] S. Mikhailov, L. Zhang, T. Geernaert, F. Berghmans, and L. Thévenaz, "Distributed Hydrostatic Pressure Measurement Using Phase-OTDR in a Highly Birefringent Photonic Crystal Fiber", *"Journal of Lightwave Technology"*, vol. 37, no. 18, Sep. 2019.
- [136] E. Chmielewska, W. Urbańczyk, and W. J. Bock, "Measurement of pressure and temperature sensitivities of a Bragg grating imprinted in a highly birefringent side-hole fiber", *"Applied Optics"*, vol. 42, no. 31, Nov. 2003.
- [137] X. Lu, M. A. Soto, and L. Thévenaz, "Temperature-strain discrimination in distributed optical fiber sensing using phase-sensitive optical time-domain reflectometry", *"Optics express"*, vol. 25, no. 14, 2017.
- [138] J. R. Clowes, S. Syngellakis, and M. N. Zervas, "Pressure sensitivity of side-hole optical fiber sensors", *"IEEE Photonics Technology Letters"*, vol. 10, no. 6, 1998.
- [139] T. Martynkien, A. Anuszkiewicz, G. Statkiewicz-Barabach, J. Olszewski, G. Golojuch, M. Szczurowski, W. Urbanczyk, J. Wojcik, P. Mergo, M. Makara, T. Nasilowski, F. Berghmans, and H. Thienpont, "Birefringent photonic crystal fibers with zero polarimetric sensitivity to temperature", *"Applied Physics B"*, vol. 94, no. 4, Feb. 2009.
- [140] K. Takada, K. Okamoto, Y. Sasaki, and J. Noda, "Ultimate limit of polarization cross talk in birefringent polarization-maintaining fibers", *"JOSA A"*, vol. 3, no. 10, 1986.
- [141] K. Okamoto, Y. Sasaki, and N. Shibata, "Mode coupling effects in stress-applied single polarization fibers", *"IEEE Journal of Quantum Electronics"*, vol. 18, no. 11, 1982.

BIBLIOGRAPHY

- [142] L. Zhang, M. Fisser, F. Yang, and L. Thévenaz, "Distributed hydrogen monitoring with phase-sensitive optical time-domain reflectometry", *Optical Fiber Sensors*, Optical Society of America, 2018, ThE17.
- [143] A. H. Hartog, *An introduction to distributed optical fibre sensors*. CRC press, 2017.
- [144] Y. Muanenda, "Recent advances in distributed acoustic sensing based on phase-sensitive optical time domain reflectometry", *Journal of Sensors*, vol. 2018, 2018.
- [145] D. Chen, Q. Liu, and Z. He, "108-km distributed acoustic sensor with $220 \text{ p}\epsilon\sqrt{\text{Hz}}$ strain resolution and 5-m spatial resolution", *Journal of Lightwave Technology*, vol. 37, no. 18, Sep. 2019.
- [146] J. J. Mompó, S. Martín-López, M. González-Herráez, and A. Loayssa, "Sidelobe apodization in optical pulse compression reflectometry for fiber optic distributed acoustic sensing", *Optics letters*, vol. 43, no. 7, 2018.
- [147] D. Chen, Q. Liu, X. Fan, and Z. He, "Distributed Fiber-Optic Acoustic Sensor With Enhanced Response Bandwidth and High Signal-to-Noise Ratio", *Journal of Lightwave Technology*, vol. 35, no. 10, May 2017.
- [148] S. Liehr, S. Münzenberger, and K. Krebber, "Wavelength-scanning coherent OTDR for dynamic high strain resolution sensing", *Optics Express*, vol. 26, no. 8, Apr. 2018.
- [149] P. Westbrook, K. Feder, T. Kremp, T. Taunay, E. Monberg, J. Kelliher, R. Ortiz, K. Bradley, K. Abedin, D. Au, *et al.*, "Integrated optical fiber shape sensor modules based on twisted multicore fiber grating arrays", *Optical Fibers and Sensors for Medical Diagnostics and Treatment Applications XIV*, International Society for Optics and Photonics, vol. 8938, 2014, 89380H.
- [150] D. Johlen, P. Knappe, H. Renner, and E. Brinkmeyer, "Uv-induced absorption, scattering and transition losses in uv side-written fibers", *Optical Fiber Communication Conference*, Optical Society of America, 1999, ThD1.
- [151] A. Asseh, H. Storoy, B. E. Sahlgren, S. Sandgren, and R. A. Stubbe, "A writing technique for long fiber bragg gratings with complex reflectivity profiles", *Journal of Lightwave Technology*, vol. 15, no. 8, 1997.
- [152] P. Lu, S. J. Mihailov, D. Coulas, H. Ding, and X. Bao, "Low-loss random fiber gratings made with an fs-ir laser for distributed fiber sensing", *Journal of Lightwave Technology*, vol. 37, no. 18, 2019.
- [153] P. Lefebvre, A. Vincelette, C. Beaulieu, and P. Ficocelli, "Automated manufacturing of fiber bragg grating arrays", *Optical Fiber Sensors*, Optical Society of America, 2006, ThE27.
- [154] C. Askins, M. Putnam, G. Williams, and E. Friebele, "Stepped-wavelength optical-fiber bragg grating arrays fabricated in line on a draw tower", *Optics Letters*, vol. 19, no. 2, 1994.

- [155] H. D. Bhatta, L. Costa, A. Garcia-Ruiz, M. R. Fernandez-Ruiz, H. F. Martins, M. Tur, and M. Gonzalez-Herraez, "Dynamic measurements of 1000 microstrains using chirped-pulse phase-sensitive optical time-domain reflectometry", *Journal of Lightwave Technology*, vol. 37, no. 18, 2019.
- [156] G. Cedilnik, G. Lees, P. E. Schmidt, S. Herstrøm, and T. Geisler, "Pushing the reach of fiber distributed acoustic sensing to 125 km without the use of amplification", *IEEE Sensors Letters*, vol. 3, no. 3, 2019.
- [157] T. Hübert, L. Boon-Brett, G. Black, and U. Banach, "Hydrogen sensors—a review", *Sensors and Actuators B: Chemical*, vol. 157, no. 2, 2011.
- [158] S. Sumida, S. Okazaki, S. Asakura, H. Nakagawa, H. Murayama, and T. Hasegawa, "Distributed hydrogen determination with fiber-optic sensor", *Sensors and Actuators B: Chemical*, vol. 108, no. 1-2, 2005.
- [159] D. Y. Wang, Y. Wang, J. Gong, and A. Wang, "Fully distributed fiber-optic hydrogen sensing using acoustically induced long-period grating", *IEEE Photonics Technology Letters*, vol. 23, no. 11, 2011.
- [160] T. Chen, Q. Wang, R. Chen, B. Zhang, K. P. Chen, M. Maklad, and P. R. Swinehart, "Distributed hydrogen sensing using in-fiber Rayleigh scattering", *Applied Physics Letters*, vol. 100, no. 19, 2012.
- [161] M. Fisser, R. A. Badcock, P. D. Teal, and A. Hunze, "Optimizing the sensitivity of palladium based hydrogen sensors", *Sensors and Actuators B: Chemical*, vol. 259, 2018.
- [162] F. Lewis, "The palladium-hydrogen system: structures near phase transition and critical points", *International journal of hydrogen energy*, vol. 20, no. 7, 1995.
- [163] M. Fisser, R. A. Badcock, P. D. Teal, and A. Hunze, "Improving the sensitivity of palladium-based fiber optic hydrogen sensors", *Journal of Lightwave Technology*, vol. 36, no. 11, 2018.
- [164] M. Butler and D. Ginley, "Hydrogen sensing with palladium-coated optical fibers", *Journal of applied physics*, vol. 64, no. 7, 1988.
- [165] G. T. Jasion, T. D. Bradley, K. Harrington, H. Sakr, Y. Chen, E. N. Fokoua, I. A. Davidson, A. Taranta, J. R. Hayes, D. J. Richardson, *et al.*, "Hollow core nanf with 0.28 db/km attenuation in the c and l bands", *Optical Fiber Communication Conference*, Optical Society of America, 2020, Th4B-4.
- [166] F. Yang, F. Gyger, and L. Thévenaz, "Intense brillouin amplification in gas using hollow-core waveguides", *Nature Photonics*, 2020.

List of acronyms

ϕ -OTDR	Phase-sensitive optical time-domain reflectometry
DOFS	Distributed optical fiber sensor
PCF	Photonic crystal fiber
SpRS	Spontaneous Raman scattering
DTS	Distributed temperature sensor
SpBS	Spontaneous Brillouin scattering
SMF	standard single mode fiber
BOTDR	Brillouin optical time-domain reflectometry
BOFDR	Brillouin optical frequency-domain reflectometry
SBS	Stimulated Brillouin scattering
BOTDA	Brillouin optical time-domain analyzer
BOFDA	Brillouin optical frequency-domain analyzer
EDFA	Erbium doped fiber amplifier
OTDR	Optical time-domain reflectometry
OFDR	Optical frequency-domain reflectometry
OCDR	Optical coherence-domain reflectometry
FUT	Fiber under test
SOP	State of polarization
POTDR	Polarization optical time-domain reflectometry
FRM	Faraday rotator mirror
PZT	Piezoelectric transducer
DUE	Device under evaluation
BOCDA	Brillouin optical correlation-domain analyzer
BOCDR	Brillouin optical correlation-domain reflectometry
MZ	Mach-Zehnder
PGC	Phase-generated carrier
OLO	Optical local oscillator
EOM	Electro-optic modulator
Cir	Circulator
TF	Tunable filter
PD	Photodetector

List of acronyms

OSC	Oscilloscope
PC	Personal computer
FBG	Fiber Bragg grating
PDF	Probability density function
FS	Frequency shift
CC	Cross correlation
LMS	Least mean square
SNR	Signal-to-noise ratio
PLE	Probability of large errors
PG	Pulse generator
Sync	Synchronization
DFB	Distributed feedback
ASE	Amplified spontaneous emission
DPS	Distributed pressure sensing
SAHF	Side air holes fiber
RS	Rayleigh spectra
OS	Optical source
PSw	Polarization switch
PolC	Polarization controller
OR	Optical receiver
DDFS	Distributed and dynamic strain sensing
SHM	Structure health monitoring
PPA	Perfect periodic auto-correlation
AWG	Arbitrary wave generator
RF	Radio frequency
PSD	Power spectral density
Pd	Palladium
HCF	Hollow-core fiber

List of symbols

Symbol	Unit	Definition
ϕ		Phase of electric field
E_0	J	Energy of ground state of a molecular
E_1	J	Energy of an excited state of a molecular
ω	Hz	Optical angular frequency
h	$\text{m}^2 \cdot \text{kg}/\text{s}$	The Planck constant
Ω_A	Hz	Angular frequency of the thermal vibration of the molecule related to Raman scattering
ν_R	Hz	Raman frequency shift
N_{ave}		The average number of thermally activated phonons in a material
K_B	$\text{m}^2 \text{kg} \cdot \text{s}^{-2} \text{K}^{-1}$	The Boltzmann constant
T	K	Temperature
\mathbf{k}	m^{-1}	Optical wave vector
ν	Hz	Optical wave frequency
\mathbf{q}	m^{-1}	Acoustic wave vector
ν_a	Hz	Acoustic wave frequency
c	m/s	Speed of light in vacuum
V_a	m/s	Acoustic velocity in a material
n		Refractive index in a material
ν_B	Hz	The Brillouin shift
λ	m	The wavelength of an optical wave in vacuum
Γ	s^{-1}	The damping factor
g_B	$\text{m} \cdot \text{W}^{-1}$	The Brillouin gain factor
p_{12}		The longitudinal elasto-optic coefficient
A_{eff}	m^2	The effective area of an optical fiber
ρ	$\text{kg}^3 \text{m}^{-3}$	Density of a material
K_p		A factor describing the alignment between the polarization state of pump and signal in Brillouin scattering
\mathbf{D}	$\text{C} \cdot \text{m}^{-2}$	The electric displacement vector
\mathbf{E}	V/m	The electric field

Symbol	Unit	Definition
\mathbf{P}	$\text{C}\cdot\text{m}^{-2}$	The polarization vector
ϵ	F/m	The permittivity in a material
ϵ_0	F/m	The permittivity in vacuum
χ	F/m	The susceptibility tensor
\mathbf{I}		The identity matrix
β		The propagation constant of an optical wave
I	$\text{W}\cdot\text{m}^2$	The optical intensity
V	m^3	Volume
γ_e	m^4/C^2	The electrostrictive constant
C_T	m^2/N	The isothermal compressibility
p	N/m^2	Pressure
s	J/K	Entropy
c_p	$\text{J}\cdot\text{kg}^{-1}\text{K}^{-1}$	The specific heat at constant pressure
κ	$\text{W}/(\text{m}\cdot\text{K})$	The thermal conductivity
F		Capture coefficient
α_r		Rayleigh scattering coefficient
$v - g$	m/s	Group velocity of optical pulse in material
P	W	The optical power
W	s	The pulse width
α	m^{-1}	The fiber attenuation coefficient
n_g		The group refractive index of an optical pulse in the material
γ	Hz/s	The frequency scan rate of the light modulation
f	Hz	The frequency of an electric wave
L	m	The fiber length
ϵ		Strain
\mathbb{S}_j		The strain vector
μ		Poisson's ratio of the material
E	Pa	The Young's modulus
t	s	Time
M		The number of scatters covered by an optical pulse
F	Hz	The frequency scan range
B_s	s	the statistical bandwidth of a frequency-domain trace
N		The number of scanned frequency

List of publications

- 1 **L. Zhang**, Z. Yang, N. Gorbatov, R. Davidi, M. Galal, L. Thévenaz, and M. Tur, "Distributed and dynamic strain sensing with high spatial resolution and large measurable strain range," *Opt. Lett.*, 2020.
- 2 **L. Zhang**, L. D. Costa, Z. Yang, M. A. Soto, M. González-Herráez and L. Thévenaz, "Analysis and Reduction of Large Errors in Rayleigh-based Distributed Sensor," in *Journal of Lightwave Technology*, 2019.
- 3 X. Lu, M. A. Soto, **L. Zhang** and L. Thévenaz, "Spectral Properties of the Signal in Phase-Sensitive Optical Time-Domain Reflectometry With Direct Detection," in *Journal of Lightwave Technology*, 2020.
- 4 S. Mikhailov, **L. Zhang**, T. Geernaert, F. Berghmans and L. Thévenaz, "Distributed hydrostatic pressure measurement using phase OTDR in a highly birefringent photonic crystal fiber," in *Journal of Lightwave Technology*, 2019.
- 5 **L. Zhang**, Z. Yang, F. Gyger, M. A. Soto, and L. Thévenaz, "Rayleigh-Based Distributed Optical Fiber Sensing Using Least Mean Square Similarity," in *Optical Fiber Sensors Conference (OFS 26)*, Lausanne, Switzerland, September 2018.
- 6 **L. Zhang**, Z. Yang, Ł. Szostkiewicz, K. Markiewicz, T. Nasilowski, and L. Thévenaz, "Fully Distributed Pressure Sensing with Ultra-high-sensitivity using Side-hole Fibers," in *Optical Fiber Sensors Conference (OFS 26)*, Lausanne, Switzerland, September 2018.
- 7 **L. Zhang**, M. Fisser, F. Yang, and L. Thévenaz, "Distributed Hydrogen Monitoring with Phase-sensitive Optical Time-Domain Reflectometry," in *Optical Fiber Sensors Conference (OFS 26)*, Lausanne, Switzerland, September 2018.
- 8 T. F. P. Neves, **L. Zhang**, F. Yang, K. H. Tow, P. Petagna and L. Thévenaz, "A kilometre-range distributed relative humidity sensor," in *Seventh European Workshop on Optical Fibre Sensors*, August 2019.
- 9 S. Mikhailov, **L. Zhang**, T. Geernaert, F. Berghmans, K. Hey Tow, and L. Thévenaz, "Distributed hydrostatic pressure measurement using phase-OTDR in a highly birefringent photonic crystal fibre," in *International Conference on Optical Fibre Sensors (OFS-26)*, Lausanne, Switzerland, September 2018.

Li Zhang**Gender:** Female**Date of Birth:** 28/04/1991**Tel:** (+41) 21 69 37387**Email:** li.zhang@epfl.ch**Address:** EPFL SCI STI LT ELE 117, CH-1015 Lausanne, Switzerland**EDUCATION****11. 2016 -12. 2020: EPFL Swiss Federal Institute of Technology**

PhD of photonics

Fellowship of Marie Skłodowska-Curie Innovative Training Network "FINESSE"

09. 2013 -06. 2016: University of Electronic Science and Technology of China

Outstanding graduate student award of the province

M.E. of Optical Engineering; GPA: 3,72/4; Ranking: 3/50.

09. 2009 -06. 2013: Ocean University of China

Outstanding graduate student award of the province

BSc of Optical Information Science and Technology; GPA: 84,2/100; Ranking: 6/48.

RESEARCH FOCUS

Fiber optics; Distributed fiber sensing; Rayleigh scattering

PROFESSIONAL SKILLS

- Hands-on experience on optical sensing systems and signal processing;
- Programming : C, C#, MATLAB, LabVIEW;
- Other software: COMSOL, Inkscape, Office, Latex;
- Language: Chinese (mother language); English (working language); French (A2)

RESEARCH EXPERIENCE**● Group of Fiber Optics, EPFL****11. 2016-12. 2020: distributed fiber sensing based on Rayleigh scattering.**

- Distributed temperature alarm using hollow-core fiber.
- Distributed pressure/temperature/strain/hydrogen sensing with high spatial resolution.
- Large error analysis of phase-sensitive OTDR.

● School of Electrical Engineering, Tel Aviv University, Israel**03. 2019-06. 2019: distributed and dynamic strain measurement with high spatial resolution.****● Photonics research and innovation center, Vrije Universiteit Brussel, Belgium****10. 2018-11. 2018: theoretical analysis on the temperature and pressure sensitivity of side air holes fiber.****● Photonics Engineering Group, University of Alcalá, Spain****09. 2017-11. 2017: analysis of large errors in phase-sensitive OTDR.**